THE STRUCTURE OF SMALL SILVER PARTICLES

by

Laurence Daniel Marks
Kings College
Cambridge

A dissertation submitted for the degree of
Doctor of Philosophy
at the University of Cambridge

June, 1980.

"....· ει γαρ και τα μαλιστα τυχοι τετελεσμευω ειπω, αυτοζ αμωζ ωκ οιδε·....."

"....: for even if one chanced to say the complete truth, yet oneself knows it not;....."

Xenophanes of Colophon, Fragment 34 in Kirk G C and Ravey J E, The Presocratic Philosophers (1975) (Cambridge University Press, Cambridge).

PREFACE

This dissertation is the result of research carried out at the Cavendish Laboratory during the years 1976-1980. The first three years were financed jointly by the Science Research Council and I.C.I. Ltd. through a CASE Studentship, for which I am grateful. I would like to thank my supervisors Dr R. Clayton and Dr A. Howie for their interest and guidance. I am indebted to Dr Howie for his tolerance and expert advice throughout all stages of my work. Among the many others who have been helpful, I am especially grateful to Dr D.J. Smith for his advice in the use of the Cambridge High Resolution Electron Microscope; Dr E.H. Yoffe for many useful discussions on the energies of small particles; Dr A.B. Mistry for teaching me how to obtain high resolution images; D. Nicol for maintaining the Siemens 102 electron microscope, and B. Ambrose for advice in the preparation of specimens.

I hereby declare that all parts of this dissertation which are not explicitly attributed to others are, to the best of my knowledge, original and that no part has been submitted previously to this or any other University.

The major part of Chapter 7 has appeared under the title "Multiply-twinned particles in silver catalysts" with A. Howie in Nature 282, 196, 1979. It is intended to submit the contents of Chapters 3-6 for publication in the near future.

TABLE OF CONTENTS

CHAPTER ONE

GENERAL INTRODUCTION

1.1 Scope and Motivation

Small metal particles frequently occur in many systems of technological importance such as heterogeneous catalysts. Hence the mechanisms whereby these particles grow, and their chemical and physical behaviour are important subjects. To understand these requires a rather detailed knowledge of the precise particle structures and their thermodynamics. This is the general direction of this thesis. Fortunately particle structures and thermodynamics are in practice interlocked problems - the most powerful experimental method, direct imaging in an electron microscope, normally provides so much information that the only way of unravelling it is structural modelling!

The major metal which has been studied is silver, which is important for its unique catalytic behaviour in the epoxidation of ethylene (1.2). To a lesser extent small gold particles have also been analysed as these often have very similar structures. Additionally, the theoretical analysis in Chapter 4 has been extended to include a number of other, face-centered cubic (fcc) metals. Because of their very frequent occurrence in silver, much of the work has centered around particles with rather unusual, non-crystallographic packings called "multiply-twinned particles" (or MTPs). The detailed structure of these particles and previous work on them is described in Chapter 2.

The equilibrium surface structure of MTPs is examined, both theoretically and experimentally, in Chapter 3. The decahedral type of these particles is shown to have a rather unusual surface structure which includes re-entrant surfaces at the twin boundaries. This is successfully modelled by a modified form of the Wulff construction (Wulff 1901). Theoretical structures and total surface energies for

two extreme models of faceting are evaluated and discussed.

Following on from the total surface energy results in Chapter 3, the remaining strain-dependent energy terms are evaluated in Chapter 4. These are then employed to analyse the energy balance between MTPs and single crystals. These results show that the stability of MTPs is very sensitive to the presence of any surface impurities.

The high resolution structures of small particles are considered in Chapters 5 and 6. In Chapter 5 the structures of MTPs are considered and the possible presence of partial dislocations in these particles reported. In Chapter 6 the structures of some more complicated particles are investigated, and a new species of particles termed "polyparticles" are identified. These are similar to polycrystals, with the basic structural unit being a discrete particle, rather than a single crystal.

Finally, in Chapter 7 the presence of significant numbers of MTPs in a heterogeneous catalyst is reported. The possibility that these particles have unusual catalytic sites, and hence umusual catalytic behaviour is discussed.

1.2 Silver as a Catalyst

A particularly important application of metallic silver, second only to the adornment of the female sex, is as a catalyst for the epoxidation of ethylene. The reaction

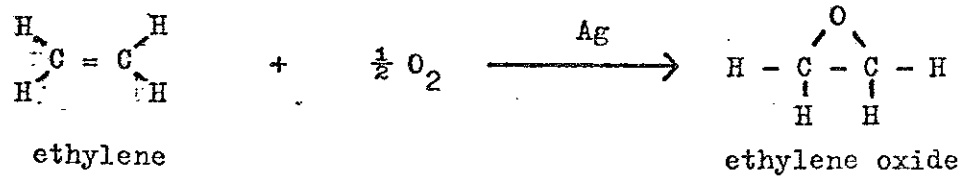

is the means whereby the commodity, ethylene, is converted into a form suitable for industrial synthesis. The most familiar use of ethylene oxide is probably in ethylene glycol, car "anti-freeze", which is the hydrated form of the chemical.

Silver is the only metal which catalyses this partial oxidation. Why this should be so is not understood, despite the fact that this catalytic reaction is probably the one which has been most extensively studied. The reaction is probably between chemisorbed molecular oxygen and gas phase ethylene (see Clayton & Norval 1980 for a recent review). Chemisorbed atomic oxygen is a negative factor, leading to a complete oxidation to carbon dioxide. The ratio between the amount of ethylene usefully converted and that burned (to CO_2 and H_2O) is termed the "selectivity", and is strongly affected by trace impurities. The most important of these is chlorine, added to the gas feed as ethylene dichloride, which appears to poison the further oxidation. It is not clear whether the precise details of particle size or morphology are important. The absence of any particle size effect reported by Wu and Harriot (1975) occurred in the absence of any chloride promoter, and hence is unrepresentative of the industrial conditions.

1.3 Experimental Techniques

The experimental technique employed throughout this thesis is electron microscopy. This is the most powerful and direct method of examining small particles, as information concerning their surface and internal structure can be obtained in far more detail than is possible with any other technique. For example, resolutions near to the atomic level are attainable in the most advanced instruments.

The basic methods of operation, and the theory of image formation are amply documented elsewhere and are not described here (see, for example, Hirsh et al 1965). In this section the principle techniques employed by the author are briefly described and cross-referenced, excepting high resolution lattice imaging which is considered in 5.2.

Three major techniques have been used: diffraction contrast bright field; axial dark field, and hollow cone dark field. A comparison between the three techniques is given in Figure 1.1 and Table 1.1. Diffraction contrast bright field is the simplest and easiest method of examining small particles, with exclusion of the diffracted beams by an aperture producing dark contrast at the particles. Typical resolutions are between 0.5 and 1 nm, depending upon the size of aperture employed. However, the contrast levels are frequently rather low, particularly with small polycrystals, so a structural identification based upon this method alone is rather problematic (see Figure 1.1a).

Improved contrast levels can be obtained by employing dark field techniques, wherein an image is produced by selecting only one or more diffracted beams with a suitable aperture. For axial dark field (Figure 1.1b), the illuminating beam is tilted so that the diffracted beams pass down the optic axis of the microscope. (Typically .8 nm resolutions were obtained, judging by the aperture size.) Examples of this technique with small particles have been provided by Ino (1966), Ino and Ogawa (1967), Avery and Sanders (1970), Yacuman and Ocana (1977), showing how structural and thickness information can be obtained. An alternative method is hollow cone dark field, where the specimen is illuminated with a hollow cone of electrons "tuned" so that the diffracted beams of interest pass down the optic axis (Treacy et al 1978). Contrast is here obtained with

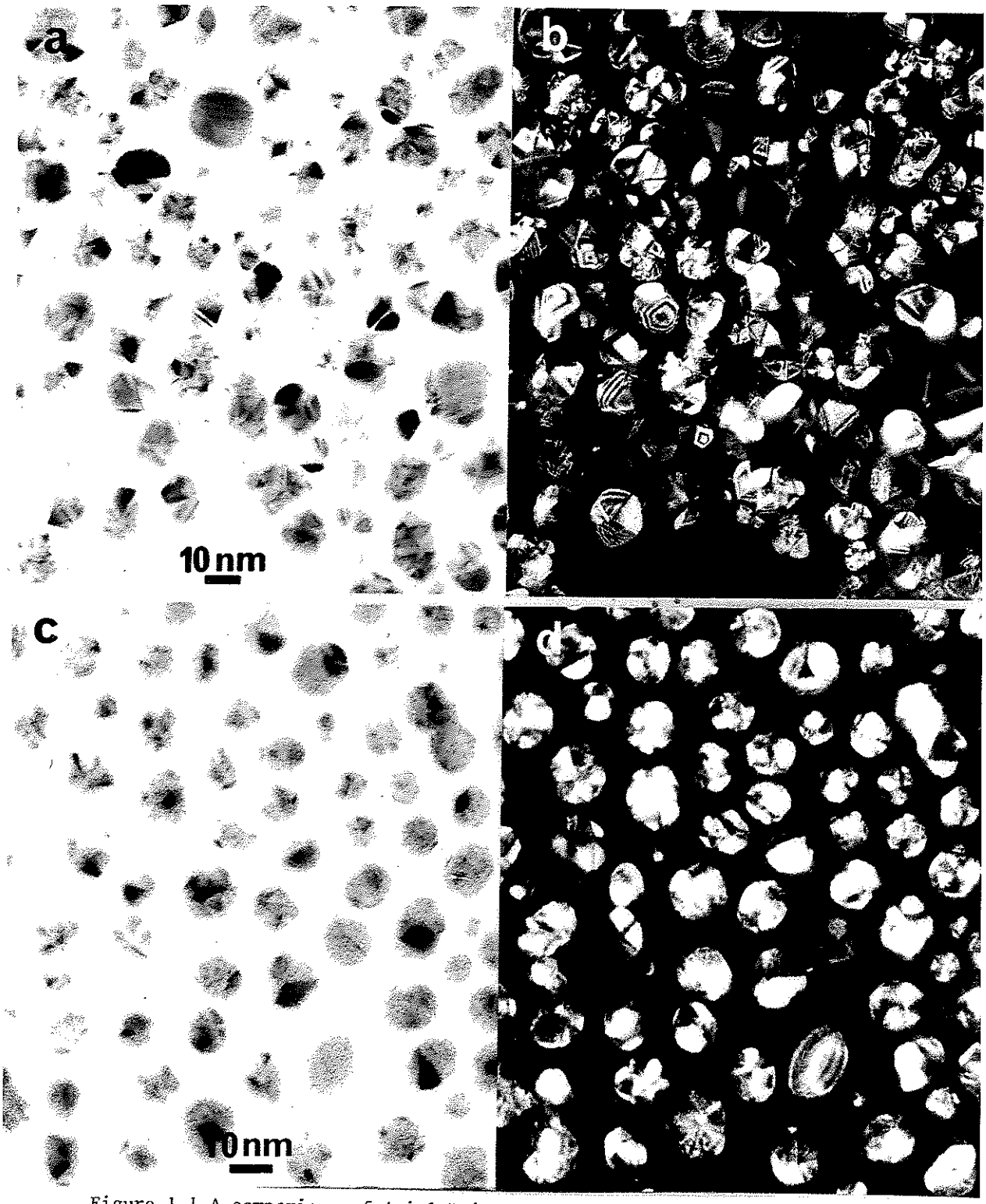

Figure 1.1 A comparison of Axial Bright Field (BF), Axial Dark Field (DF) and Hollow Cone Dark Field (HCDF). The micrographs are: a),and b), a matching BF-DF pair (the DF was obtained over the (111) and (200) rings); c), and d), a matching BF-HCDF pair (also over the (111) and (200) rings). The specimen is the silver sample prepared by evaporation onto NaCl, as described in 3.2., the background being an amorphous carbon film. Far more structural imformation is available with either of the Dark Field techniques. Particularly fine thickness fringes are obtained when using DF, whilst the general contrast levels between the particles and the substrate are better when using HCDF. Hence DF is the better mode for obtaining structural imformation, whilst HCDF is better for identifying the particles.

TABLE 1.1

A comparison of Axial Bright Field (BF), Axial Dark Field (DF) and Hollow Cone Dark Field techniques with small metal particles. All the dark field values given are suitable for imaging the (111) and (200) rings.

	BF	DF	HCDF
Operating magnification (10^5)	1.25-2.00	1.25-2.00	1.25-2.00
Exposure times (secs) (x meter)[1]	1/2 5/4-1	30-60 1/3-1	10-20 1/3-1
Aperture size (nm^{-1})	2-1	2-1	2-1
Structural identification of particles (size in nm)	$\gtrsim$10 bad method	$\gtrsim$2 only with BF	$\gtrsim$2 good method
Use for thickness fringes	very little	very good	problems with overlap
Advantages	Easy to use. Best employed togethor with dark field techniques.	High resolution of structural details. Most powerful method is to use several different tilts simultaneously (which can be pre-set).	Easy to set up; high contrast, and relatively short exposures for a dark field technique (high incident intensity).
Disadvantages	Low structural resolution. On its own can give misleading results.	Susceptible to drift and contamination.[2]	Susceptible to contamination[2] problems. Specimen may move when changing the condensor aperture.

1 These are the relative exposures to be employed when the exposure for the sample (as read from, for example, an exposure meter) is 1. The samples examined normally consisted of a dense distribution of particles on a thin (10-20 nm) amorphous carbon film, so with a different substrate, or a different distribution these values will change. The first figure is for strongly diffracting large (20 nm diameter) particles, the second for weak beam intensities or small particles.

2 Contamination with small metal particles is often sever, probably as a result of them acting as catalysts. The rate can be considerably reduced by drying the samples prior to examination in a dessicator with phosphorus pentoxide.

a suitable axial aperture. This technique provides all the possible axial dark field images for a particular diffraction angle simultaneously, and has considerable advantages in the detection of small particles (Treacy et al 1978). However, it was found in practice to provide slightly lower contrast levels and resolutions than axial dark field.

There are two other methods available for examining small particles which have not been exploited by the author. It is possible to obtain images similar to hollow cone dark field micrographs using a hollow cone objective aperture, the so called selected zone dark field technique of Heinemann and Poppa (1975). This method is particularly useful for obtaining crystallographic information, but a better approach is direct lattice imaging (see Chapter 6 in particular). Scanning transmission electron microscopes can also, at least in principle, provide considerable information (see Treacy et al 1978). A potentially very useful technique is direct microdiffraction (see, e.g., Lynch, PhD Thesis 1980), but in practice contamination rates were found by the author to be too fast.

CHAPTER 2

INTRODUCTION TO MULTIPLY TWINNED PARTICLES

2.1 Introduction

The first indication that small fcc particles can have unusual structures came with the work of Ino (1966), Ino and Ogawa (1967), and, almost simultaneously, Allpress and Sanders (1967). Both groups employed, for the first time, a combination of UHV ($\sim 10^{-8}$ pascals) evaporation and *in-situ* substrate cleavage to produce clean metal particles. In the early stages of growth (particles sized $\sim$ 200 Å in diameter) two new types of particles were observed with non-crystallographic packings. These were identified as decahedra and icosahedra composed of five and twenty twin-related fcc tetrahedra respectively (see Figures 2.5 - 2.17). The typical appearance of these particles is shown in Figure 2.1.

This chapter provides an introduction to these particles, which are generally described as multiply twinned particles, or MTPs, although various other names have appeared in the literature (e.g. cyclic twins, mono and poly-pentagonal crystallites, pentagonal and hexagonal particles). The structure and crystallography of these particles is described in 2.2 and 2.3, the literature concerning the mechanism of their formation in 2.4, their energies relative to single crystals in 2.5 and a brief review of the experimental evidence in 2.6. In the section dealing with the formation of MTPs (2.4) a brief, preliminary account of some original work by the author is included. This revives a somewhat neglected approach. To conclude this chapter, the similarity of MTPs (principally the Ics) to some other structures found in very different fields (ranging from medicine to a football pitch) is mentioned in 2.7.

For the purposes of nomenclature, the two nouns "decahedron" and "icosahedron" are reserved in this thesis exclusively for these

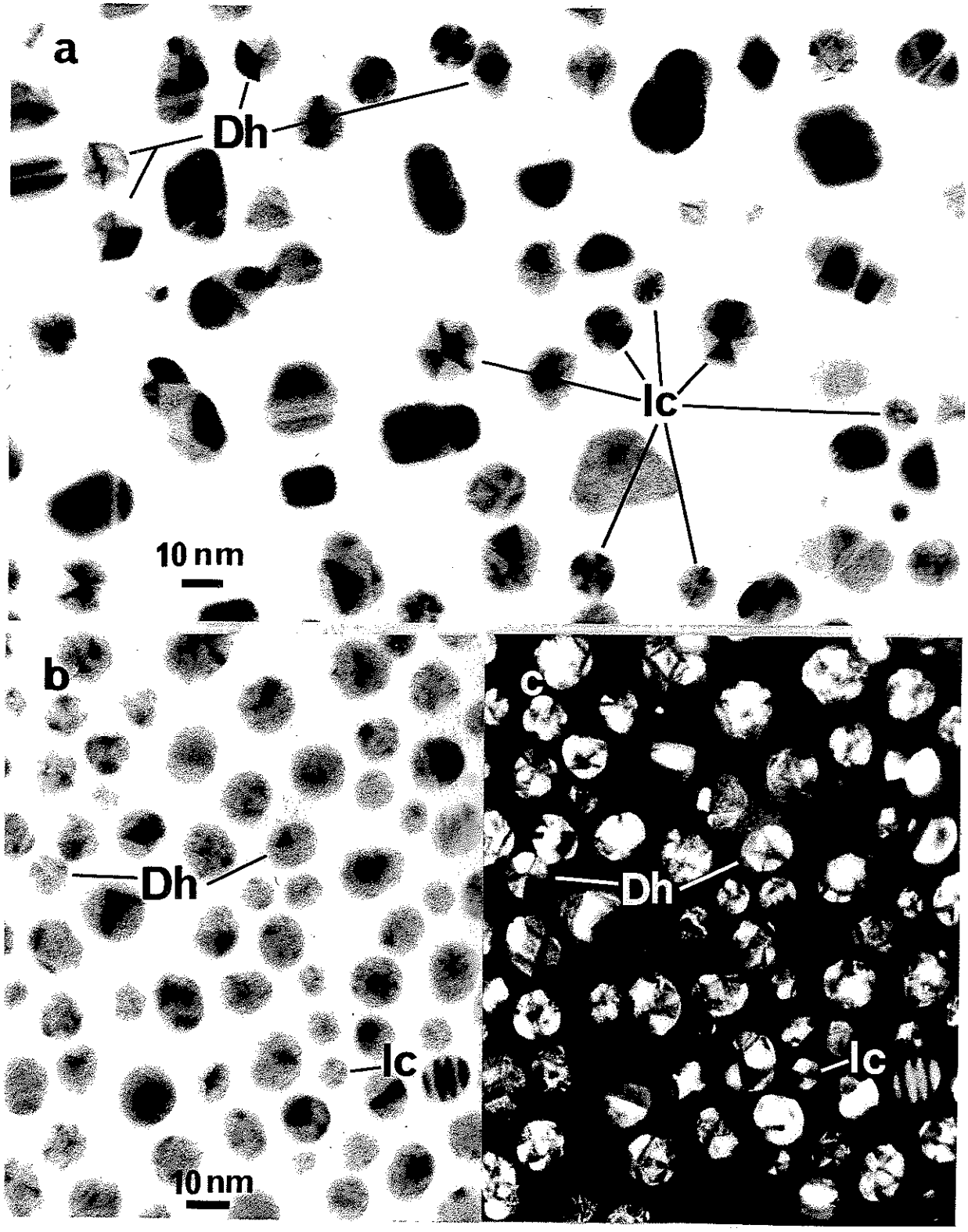

Figure 2.1 The typical appearance of MTPs in a), a "nice" sample (epitaxial silver on NaCl prepared as described in 5.3); b), and c), a matching Bright Field-Hollow Cone Dark Field pair from a "nasty" sample (the annealed silver sample on NaCl prepared as described in 3.2). The background is an amorphous carbon film. With the nice sample, Bright Field alone is adequate for indentifying these particles, but for the nasty sample Dark Field techniques are required: a number of featureless particles in b) clearly show up as MTPs in c) (taken using the (111) and (200) silver rings). It is also of interest to compare the micrograph in a), which was taken at 100 kV,to Figure 5.3, which was obtained at 500 kV.

polyhedra. The adjectives "icosahedral" and "decahedral" are loosely employed to denote particles with, respectively. I_h and D_{5h} point group symmetries (with no assumptions made concerning their surface structure). The two abbreviations Ic for icosahedral MTP and Dh for decahedral MTP are frequently employed.

2.2 Microcrystallite Model for MTPs

The most useful method for visualising the structure of MTPs is as a collection of distorted fcc microcrystallites. This "microcrystallite model" was first employed by Ino (1969), who used fcc tetrahedra with (111) faces as the starting units. Normal tensile forces are applied to two of the faces in the case of Dh, and three of the faces in an Ic to produce the shapes shown in Figure 2.2. In both cases these forces must keep the faces to which they are applied flat. (No restrictions apply to the other surfaces, except the standard elasticity boundary conditions of zero applied stresses.) Joining five of these distorted tetrahedra (face-sharing on the tensile forces) for a Dh and twenty for an Ic, the completed MTPs are produced.

It is important to realise that other, more complicated shapes than tetrahedra can be employed as the initial building blocks. The faces on which the twins occur (those upon which the tensile forces act) are fixed, but the facets which produce the particles' external surface can be varied. For example, Ino (1969) incorporated a (100) facet on each of his tetrahedral segments for a Dh. (This produces a structure with a slightly lower total surface energy.) A more detailed analysis of the optimum shapes of these initial fcc microcrystallites is described in Chapter 3.

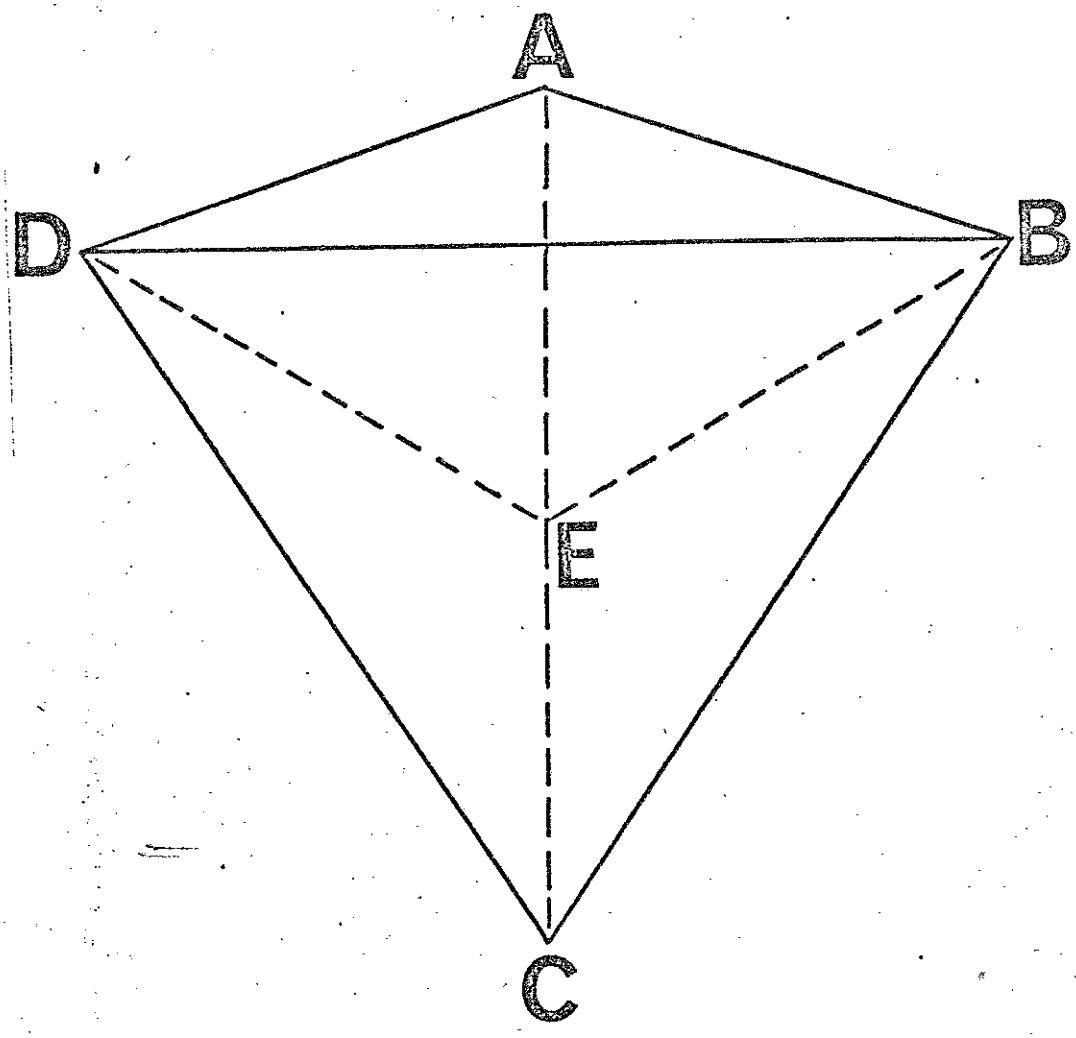

Figure 2.2 The shapes of the distorted tetrahedra present in MTPs. Starting with a tetrahedron (ABCD in the figure, with E the mid-point of AC), normal tensile forces are applied to the faces ABC and ACD for the Dh, ABC, BCD and ACD for the Ic. In both cases these faces must remain flat. For the Dh the angle BED is expanded from 70.53^{o} to 72.00^{o}; in the Ic the angles between the three stressed plains (i.e. the angle BED and the two similar angles) are expanded by the same amount. The surfaces ABD and BCD in the Dh, ABD in the Ic are not constrained (and need not be flat). It should be noted that the "sense" of these distortions is towards an orthorhombic structure in the Dh, a rhombic structure in the Ic.

An alternative approach to the individual straining described above is to consider a distortion to the collection of microcrystallites. The various cracks present can be described as missing angular gaps, and their elimination hence considered as equivalent to incorporating screw disclinations into the MTPs. (Disclinations are defects characterised by an angular deficit, comparable to the translational deficit in dislocations. A screw disclination has its rotation vector parallel to the defect line. For further details see Nabarro 1967 and Fundamental Aspects of Dislocation Theory 1970.) A single screw disclination is present in Dh (de Wit 1972) as shown in Figure 2.3, whilst six pass through an Ic as shown in Figure 2.4. (Twelve "surface disclinations" are present in an icosahedral skin, as shown by Harris 1970.) The magnitude of these disclinations depends upon the precise definition of their rotational deficits - whether by reference to the atom positions in a translationally symmetric solid (after Nabarro 1967), or by the rotation required to produce a simply-connected body (de Wit 1972). The latter is more appropriate to MTPs, and leads to a magnitude 7.356^{o}.

The precise nature of the internal strains produced by the distortions in MTPs is as yet unclear. Ino (1969) assumed homogeneous anisotropic elasticity theory to derive values of approximately 1% and4% for Dhs and Ics respectively. Bagley (1965) for the Dhs, and more recently Heinemann et al (1979)[1] considered that MTPs possess different lattice structures - orthorhombic and rhombic for Dhs and Ics respectively. It should be noted that these different structures are equivalent to completely homogeneous strains. De Wit (1972) noted the similarity between the decahedral particles

[1]The set of five papers by the group of Heinemann, Poppa, Yacamán and Yang (1979) are referred to here, and elsewhere as Heinemann et al (1979). They are separately described in the references section.

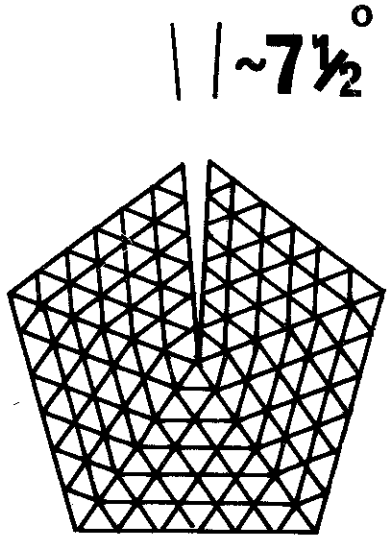

Figure 2.3 Illustration of the screw disclination in a Dh. As shown in the figure, when the five segments are assembled (here tetrahedra) there is a gap of $\sim 7.5^{\circ}$. This can be eliminated by incorporating a 7.5° screw disclination.

Figure 2.4 Illustration of the screw disclinations in an Ic. When the 20 segments (tetrahedra in the figure) are assembled there is a $\sim 7.5^{\circ}$ gap around each of the twelve 5-fold symmetry axes. These lead to the presence of six $\sim 7.5^{\circ}$ screw disclinations in the final particle.

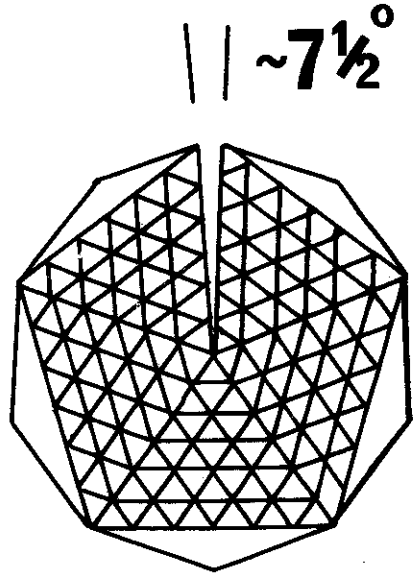

and a screw disclination and derived a plane strain solution (see 4.2.2). A more detailed analysis, with an inhomogeneous isotropic elasticity solution for the Ics, is described in 4.2.

2.3 Crystallography of MTPs

2.3.1 Introduction

The typical contrast from MTPs (in an electron microscope) and their electron diffraction patterns are generally very complicated. Consequently, qualitative theoretical models for their positionally-resolved microdiffraction patterns are invaluable when attempting to interpret the experimental results.(Quantitative models are far harder problems, requiring as they do assumptions about the form of the internal distortions. Furthermore, quantitative analysis of any experimental results is a very difficult and dangerous procedure as the particle shapes enter into the results, by the wedge splittings as described in 5.2). To obtain these, which is the subject of this section, a simple homogeneous model is adopted here. Specifically, the electron diffraction poles of an fcc tetrahedron are considered as homogeneously mapped (by the distortions) into fcc poles of the MTP microcrystallites. For example, with this procedure all the edges of the distorted tetrahedra in MTPs are considered as <110> electron diffraction poles. Alternative analyses have been presented by Ino (1966) and Ino and Ogawa (1967) (by incorporating "cracks" rather than strains in the particles) who include all the double (or triple) diffraction effects, and Heinemann et al (1979) with a homogeneous strain, but few of the double diffraction spots.

In all the following diagrams, perfect icosahedra or decahedra

noted that these are not, in general, the shapes of the particles as is shown in 3.4 (although this is not important with respect to the crystallography).

2.3.2 Icosahedral MTPs

There are three major symmetry orientations of these particles. The most common of these is when one of the microcrystallites has its external (111) surface flat against the substrate, which occurs where there is <111> epitaxy (e.g. for Au on alkali halides as observed by Ino 1966). An illustration of an icosahedron with this orientation as viewed normal to the substrate is shown in Figure 2.5a, with the crystallography of the particle described in Figure 2.6 and 2.7. The formation of pseudo-(111) double diffraction spots (as shown in Figure 2.7) is an umusual and distinctive feature of this orientation.

The second major orientation is with the icosahedron sitting edge on to the substrate, as is found, for example, for Au on alkali halides (Heinemann et al 1979). Some further faceting is of course required for this orientation, a <112> epitaxy, to occur. The detailed crystallography is described in Figure 2.8 and Figure 2.9, with a sketch of the shape shown in Figure 2.5b.

Finally, the third symmetry orientation is down one of the five-fold axes, corresponding to a <110> orientation, and is described in Figures 2.10 and 2.11, with the shape shown in Figure 2.5c. This orientation has not to date been experimentally observed, probably because it does not occur epitaxially.

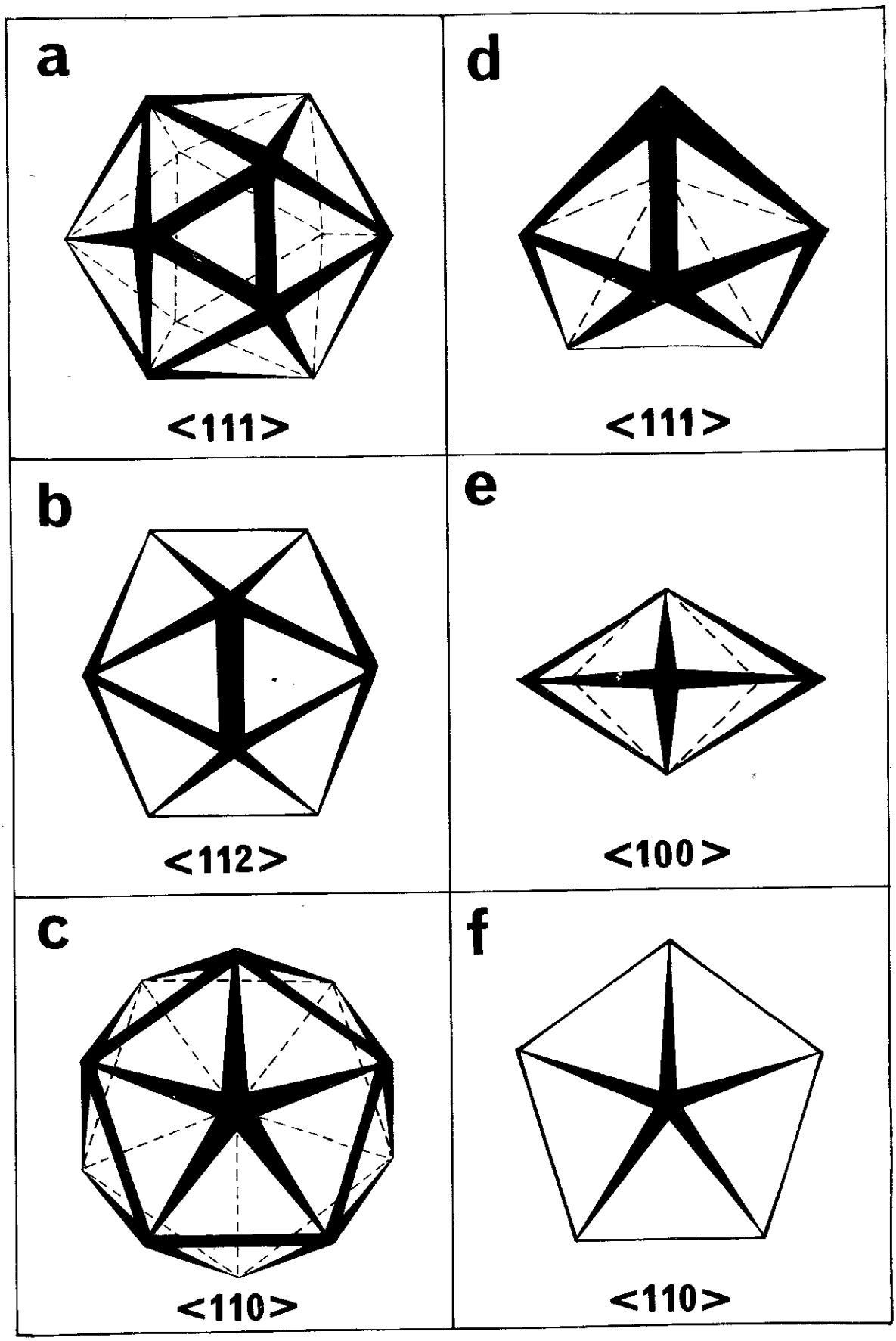

Figure 2.5 The external surface of an icosahedron (a,b and c) and a decahedron (d,e and f) as viewed down the three major symmetry axes of these structures. In b) and f) the lower surfaces are related by a mirror plane symmetry to the upper surfaces, in a) and c) by a center of symmetry. The distorted

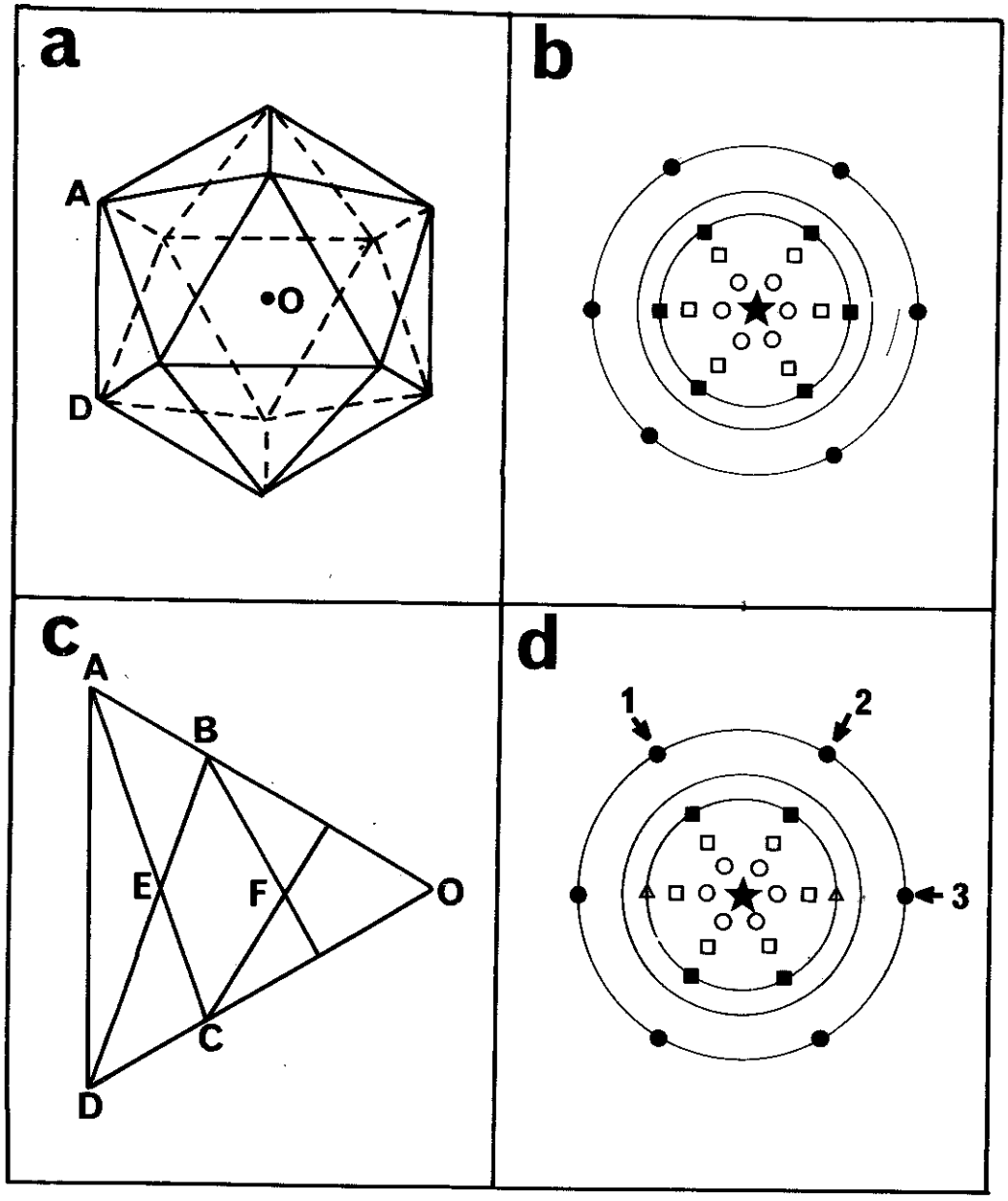

Figure 2.6 The diffraction from a <111> oriented Ic, out to the (220) ring. The particle here, shown in a), yields the total diffraction pattern shown in b). This is best analysed by reducing the section being considered to any of the six rotationally related segments, e.g. the segment AOD as marked in a) and expanded in c). Also marked on c) are the positions of the edges of the distorted tetrahedra. The breakdown is:
Primary spots: (111)= ■, and (220)= ● .
Moire spots: ○ =∿.695 nm; □ =∿.355 nm, and △ =.235 nm (pseudo-(111) fringes).
All magnitudes quoted in this figure, and the following breakdowns for MTPs are appropriate for Ag (or Au).
Positions of the spots in c) and d): ■ everywhere; all the spots along the line marked 1 in d) in BOD; all the spots along line 2 in AOC, and those marked along the line 3 in BOCE. (The (220) spots are Moirés, rather than primary spots in the section BFCE.)

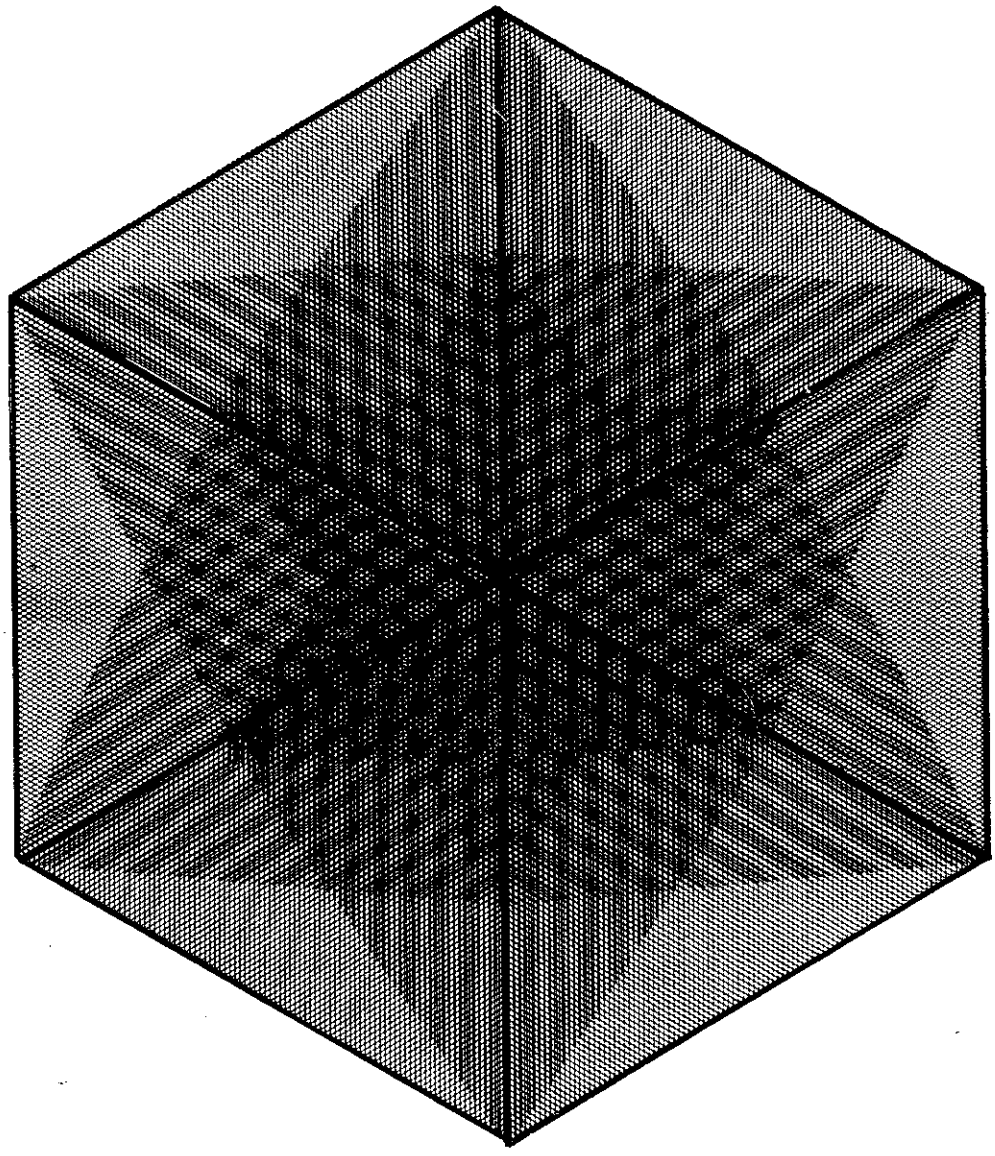

Figure 2.7 Simulation of the lattice fringes in a ⟨111⟩ oriented Ic. In this and the following figures, (110) planes rather than (220) planes have been employed (due to lack of a suitable lettraline). Hence the common (222)/(220) Moiré fringes, which in this case produce a very characteristic rosette pattern, are shown with twice their true spacings.

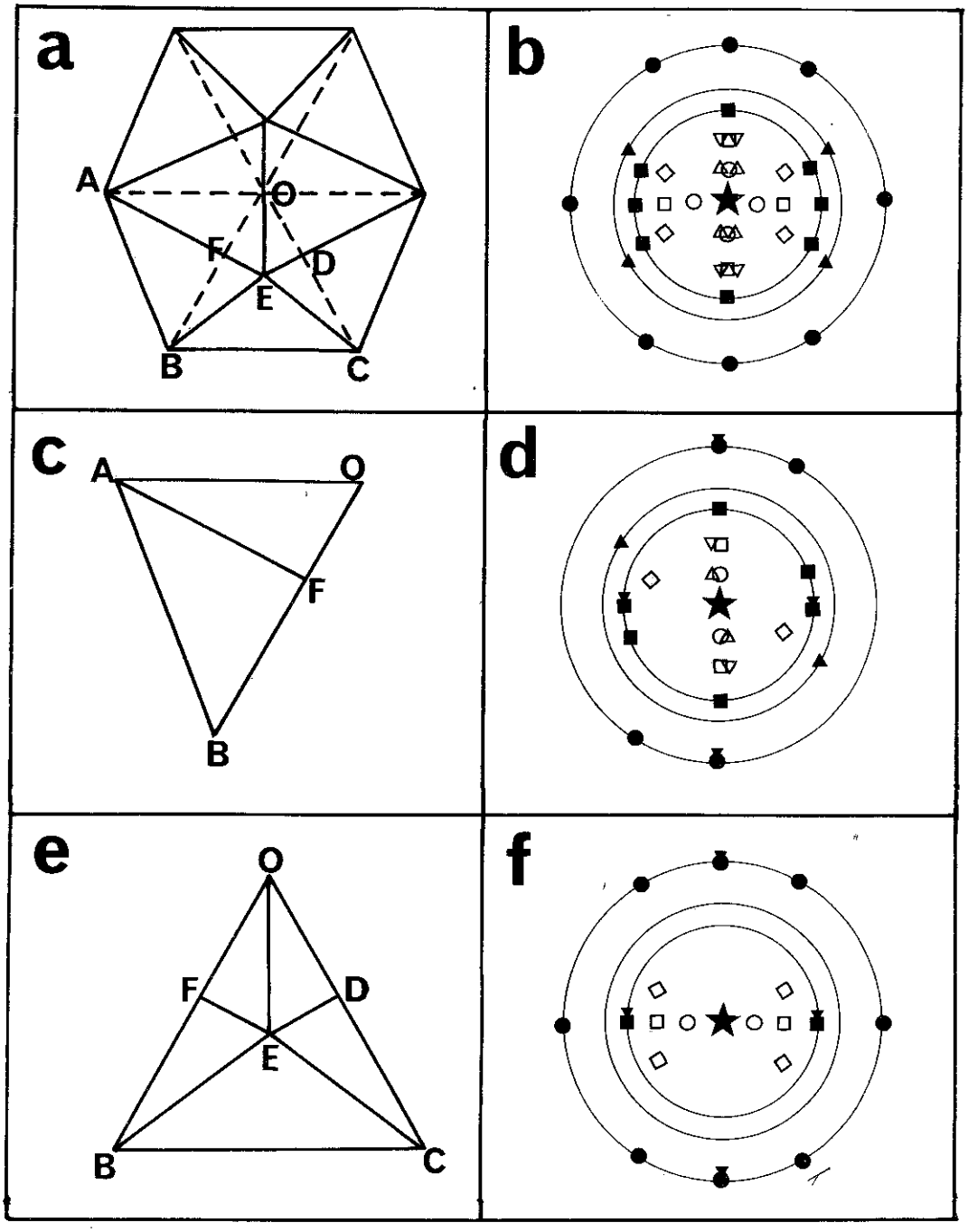

Figure 2.8 Diffraction from a <112> Ic to (220) for the primary spots and (111) for the Moires. The particle, shown in a) with its total diffraction in b), is decomposable into the segments AOB and BOC as shown in c) and e) respectively, with their diffractions shown in d) and f). The overlap between the spots ▽ , △ (produced by double diffraction between the (111) spots ■ and ▼) and ○ , □ should be noted. (This will complicate interpretation of these Moires.) The breakdown is: Spacings: (i) primary spots- (111)= ■ and ▼ ; (200)= ▲ , and (220)= ● and ▼ . (ii) Moires- ○ and △ =∿.695 nm; □ and ▽ =∿.355 nm, and ◇ =∿.270 nm. Positions: (i) in c) and d)- in AOB only, ■ , ▲ and ● ; in AOF all the spots. (ii) In e) and f)-only the (220) spots ● in FBCDE whilst all are present in ODEF.

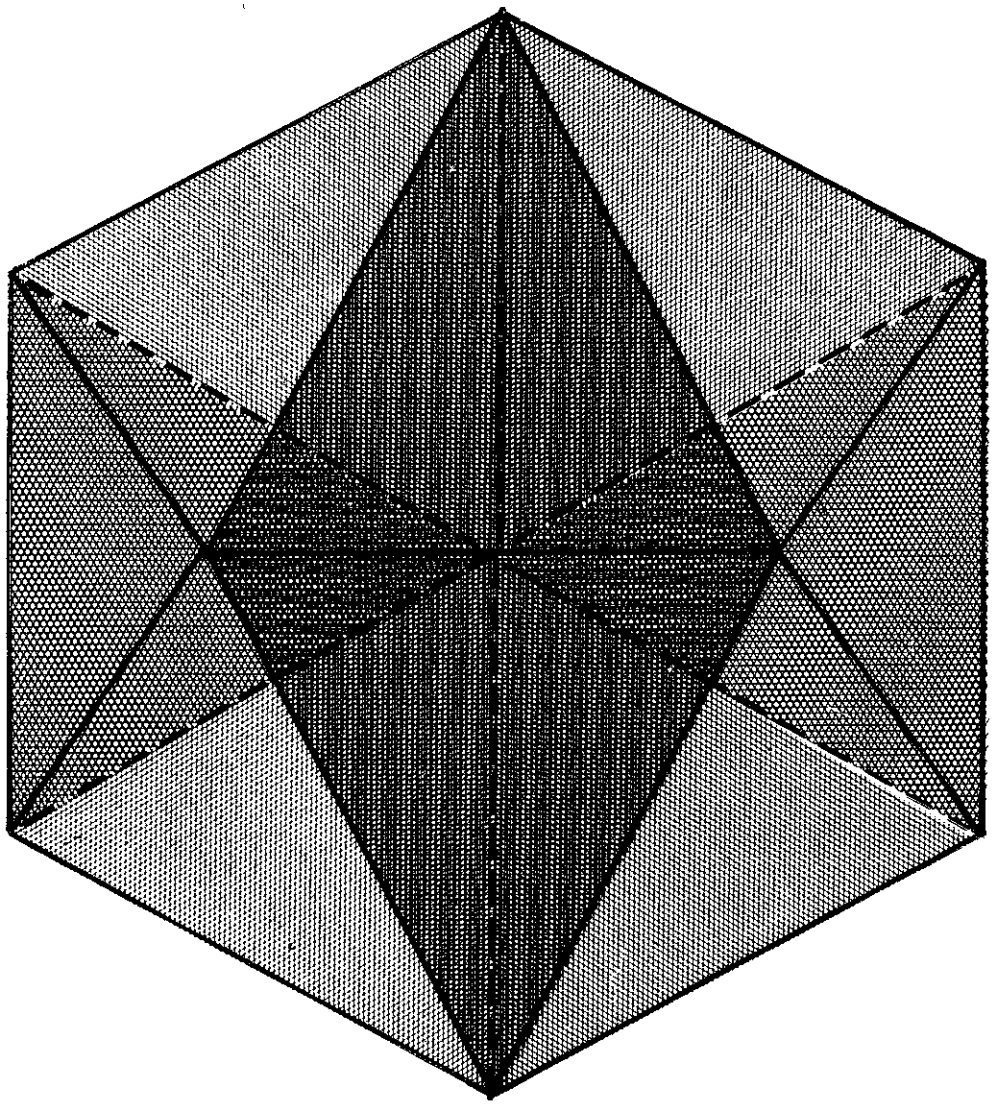

Figure 2.9 Simulation of the lattice fringes in a <112> oriented Ic. The Moire fringes are a particularly distinctive feature.

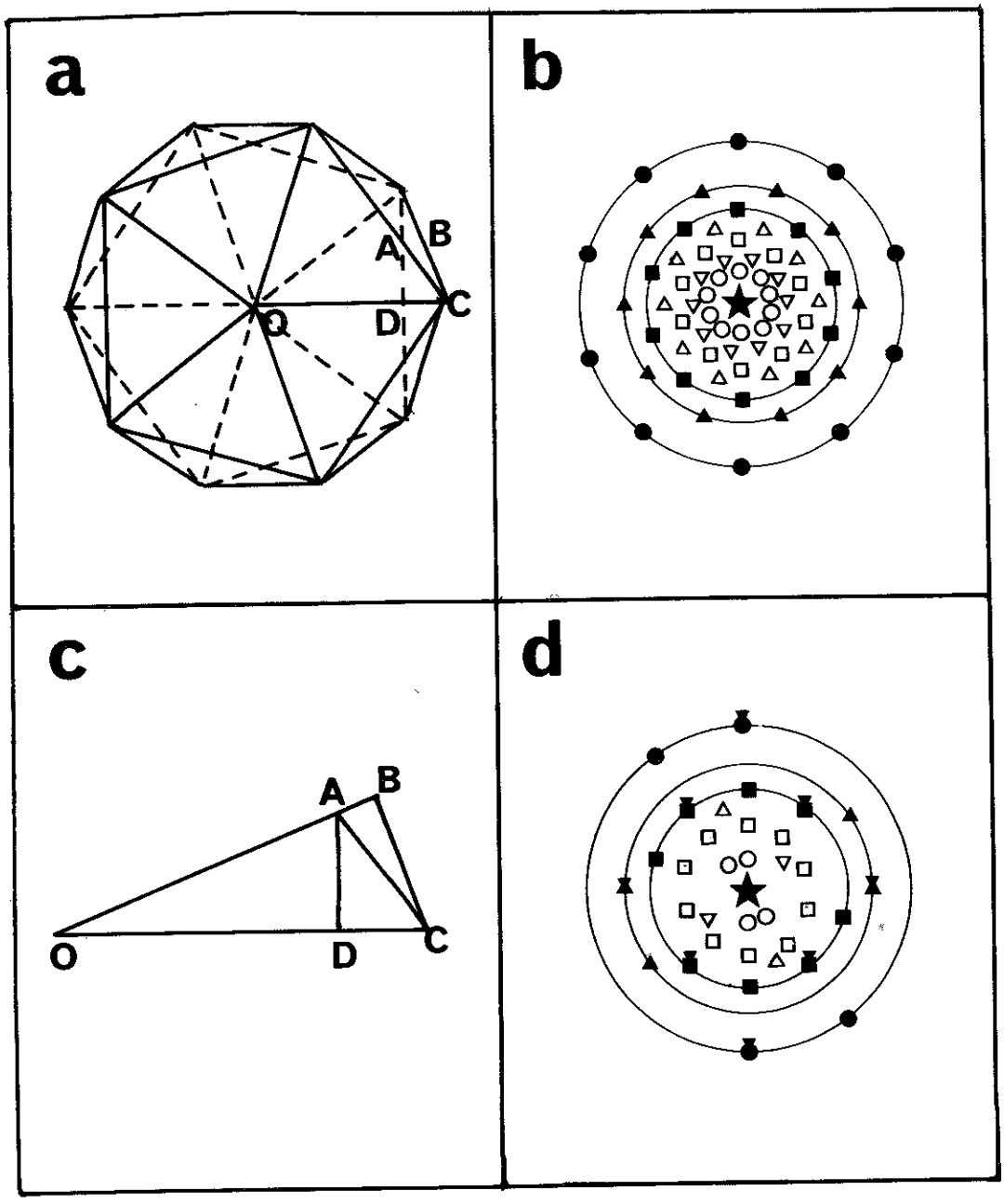

Figure 2.10 Analysis of the diffraction from a <110> oriented Ic. The primary spots are shown out to (220), the Moires out to (111). In an electron microscope, this orientation has the highest symmetry (10-fold rotational), and is in consequence very complicated. The total particle, shown in a), produces the total diffraction pattern shown in b). This contains a large number of Moire spots. These are best analysed by considering a smaller segment, e.g. the section OBC as marked in a) and shown in c), with the resulting diffraction in d). One interesting aspect of d)is the presence of a "top-bottom" effect: the pattern is less symmetric than might be expected (see the spots marked as ▽). Diagram d) has been drafted for the electron beam coming out of the plane of the paper, the spots ■ , ▲ and ● coming from the first diffracting segment. The positional breakdown is:
Primary spots: in OAC (111)= ■ and ■ ; (200)= ▲ and ▲ ; in OBC (220)= ● and ●.
Moire spots, all of which are present in OAC: ○ =∿.695 nm; ▽ =∿.411 nm; □ = ∿.355 nm, and △ =∿.278 nm.

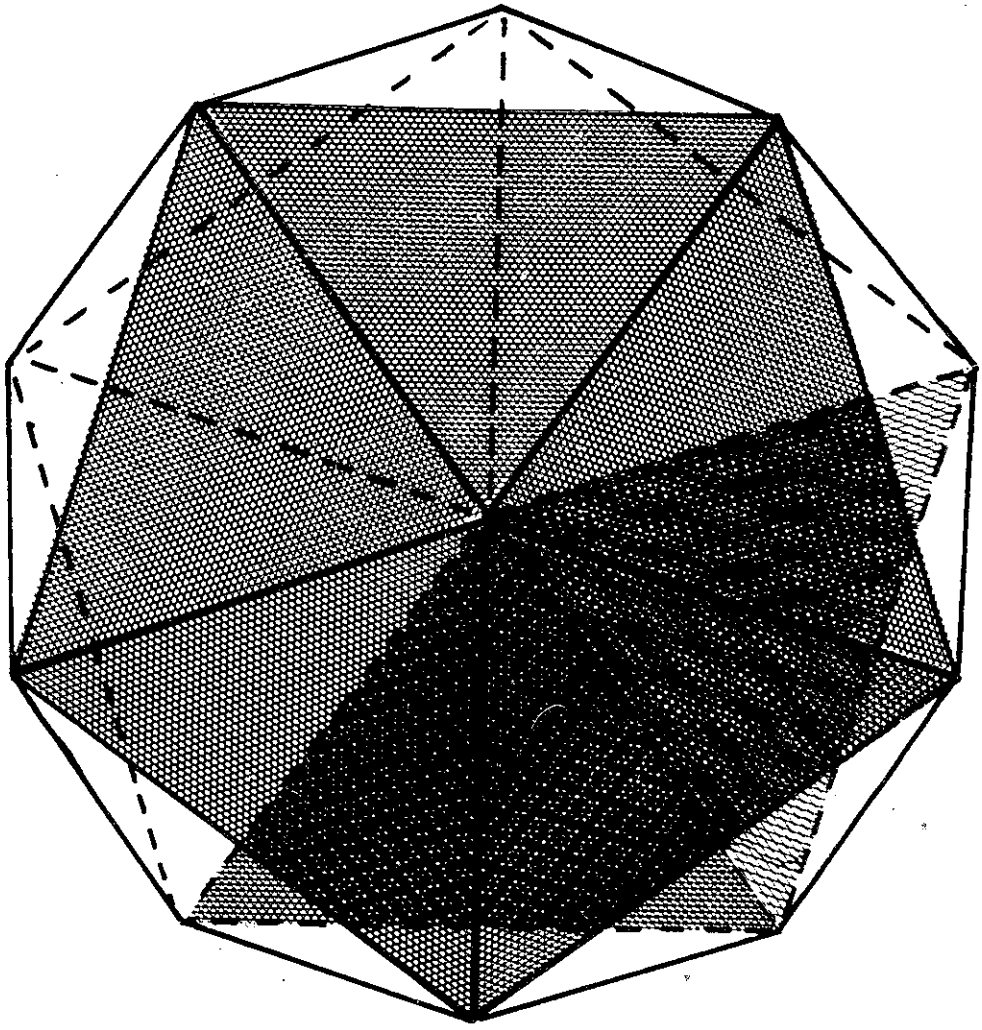

Figure 2.11 Simulation of the lattice fringes in a ·110· oriented Ic. The very complicated appearance of the Moire fringes should be noted.

2.3.3 Decahedral MTPs

In common with the Ics, there are three major symmetry orientations for the Dhs. The one most frequently encountered is when one of the microcrystallites has an external (111) facet adhering to the substrate, as illustrated in Figure 2.5d, together with its diffraction in Figure 2.12 and 2.13.

The second important orientation is where one of the unshared edges of a distorted tetrahedral segment is resting on the substrate - a ⟨100⟩ epitaxy, as found for either Ag or Au on alkali halides. All five of the microcrystallites are actively diffracting from low index planes, thereby producing a rather complicated set of double diffraction or Moire spots. The breakdown of this diffraction is shown in Figure 2.14 and Figure 2.15, with a sketch shown in Figure 2.5e. Similar to the ⟨112⟩ Ics, some further faceting must be present on this particle for it to have this epitaxy.

The final orientation of importance is down the five-fold symmetry axis as shown in Figure 2.5f. It should be noted that this ⟨011⟩ orientation is perpendicular to the ⟨100⟩ orientation described above. It is occasionally found for small Dh, probably as a result of particle disturbances during sample preparation, rather than being a natural epitaxial arrangement. The diffraction, which consists of five rotationally related (011) poles, is described in Figure 2.16 and Figure 2.17.

2.4 Growth of MTPs

The precise mechanism whereby MTPs are produced (as against their thermodynamic stabilities) is a problem which has to date only

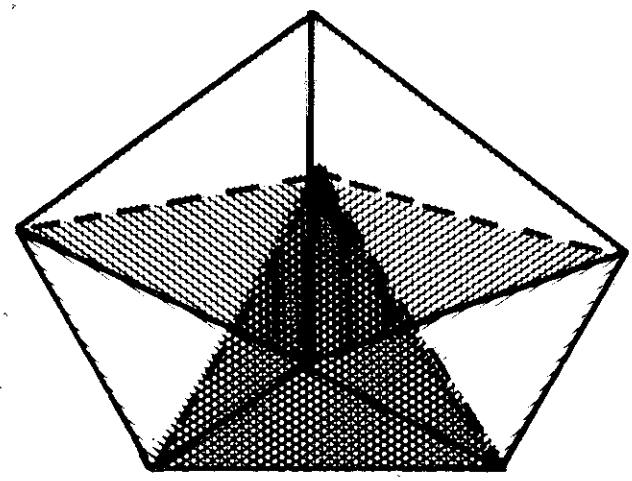

Figure 2.13 Lattice fringes in a <111> oriented Dh.

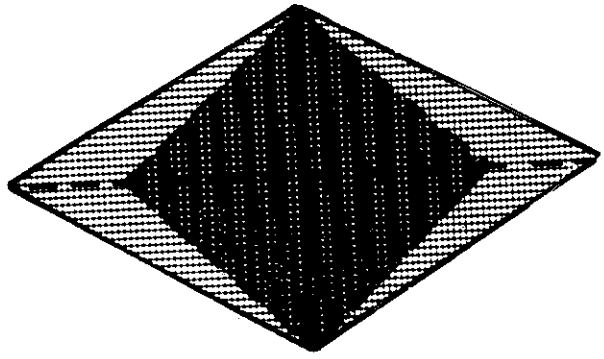

Figure 2.15 Lattice fringes in a <100> oriented Dh.

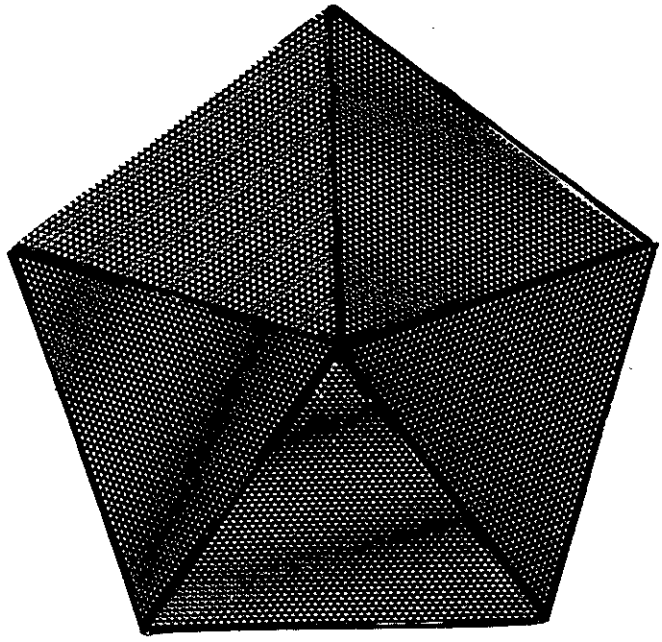

Figure 2.17 Lattice fringes in a <110> oriented Dh.

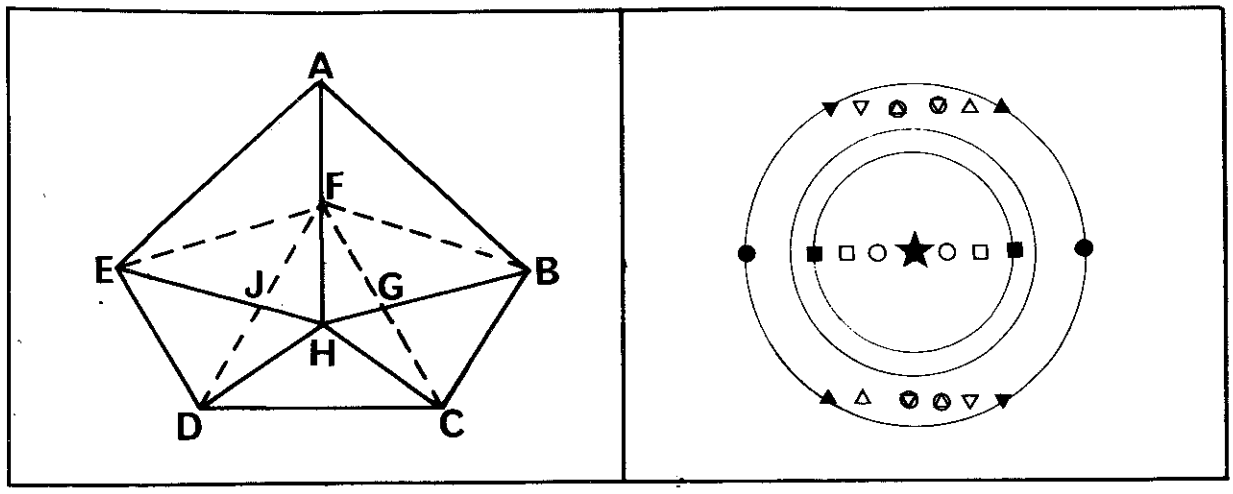

Figure 2.12 Diffraction from a <111> oriented Dh out to the (220) ring. A rather complicated set of Moire fringes is produced, the two main ones, marked on the figure as the spots ○ and □ being redily visible with spacings of ∿.695 and ∿.355 nm respectively. The positional breakdown is:
Primary spots: (111)= ■ in ABHE; (220)= ▲, ▼ and ● with ▲ in FBCD, ▼ in EFCD, and ● in DFC.
Moire spots: upright triangles (including those circled) in FBH; inverted triangles in EFH, and all the spots are present in FGHJ.

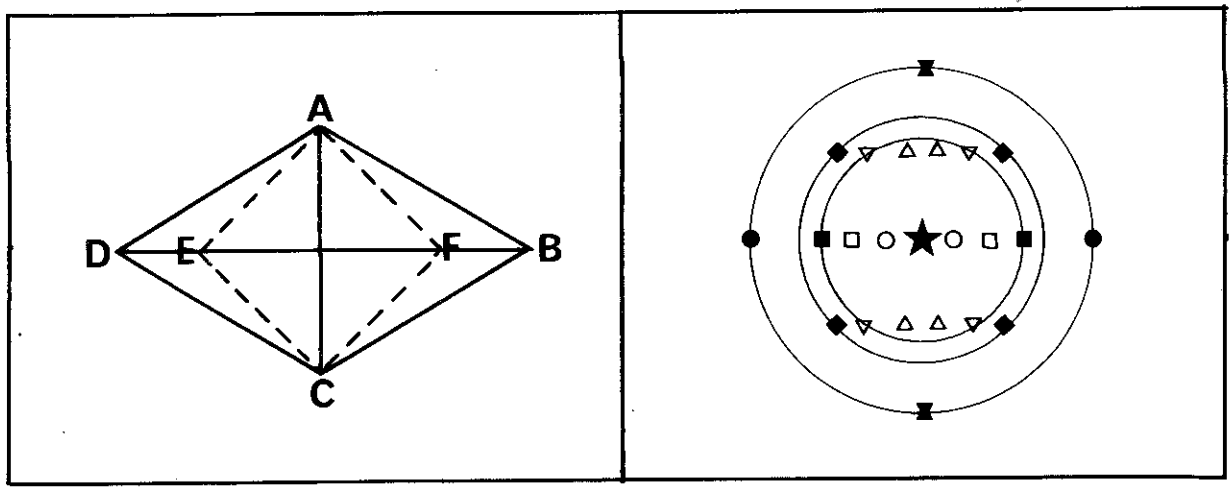

Figure 2.14 Diffraction from a <100> oriented Dh out to (220). The diffraction here is similar to that in Figure 2.12. However, all the Moire fringes are now likely to occur in the images of these particles (see Figure 5.5).Two main areas are present: The central region AFCE where all the spots are present, and the remainder of the particle where only the (111) spots ■ and the (220) spots ⧗ are active. The spacings breakdown as:
Primary spots: (111)= ■ ; (220)= ⧗ and ● , and (200)= ◆ .
Moire spots: =∿.695 nm; =∿.355 nm; △ =∿.286 nm, and ▽ =∿.239 nm.

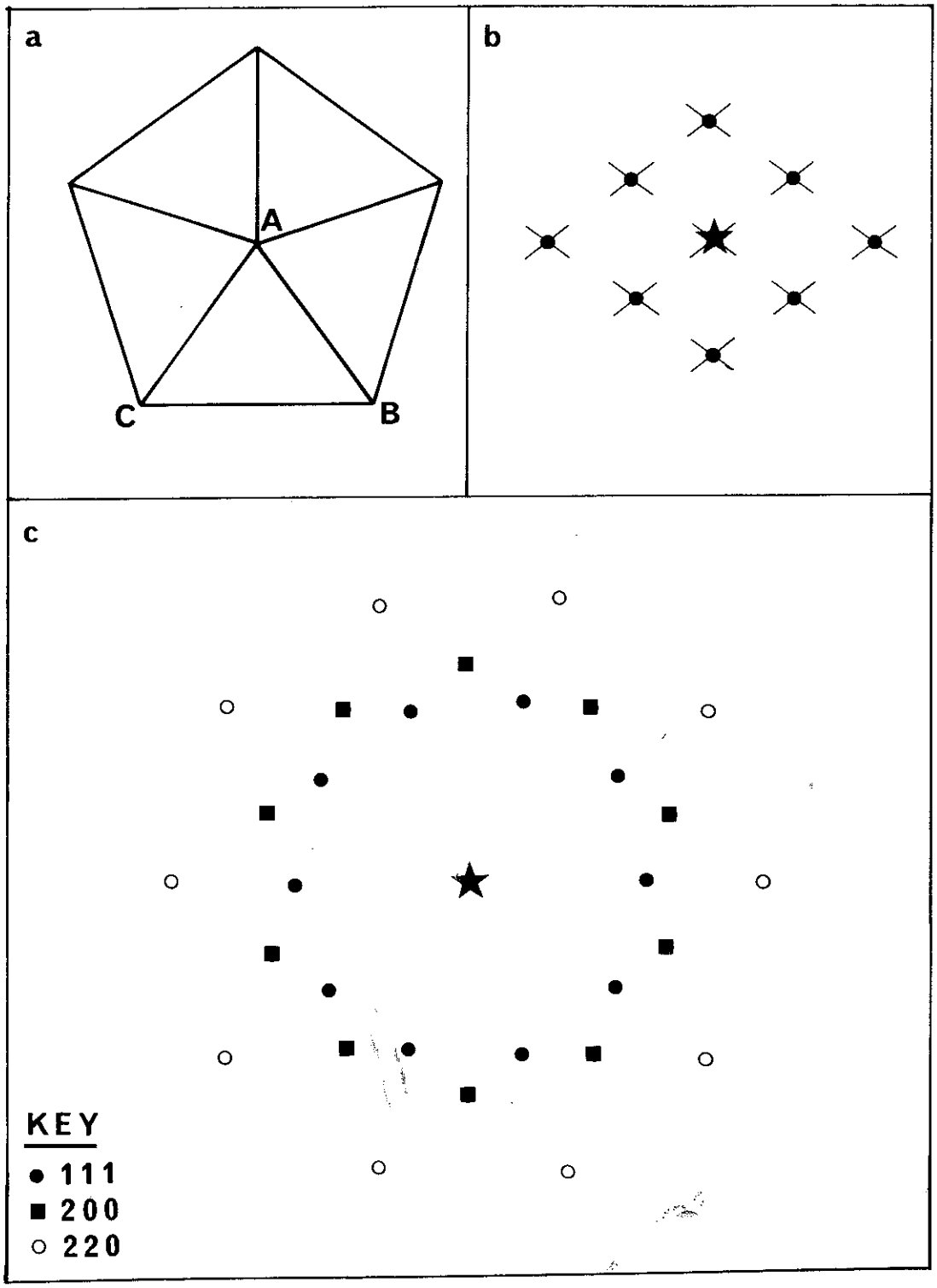

Figure 2.16 Breakdown of the diffraction from a <110> oriented Dh: a), the particle structure; b) diffraction from the segment ABC shown in a). The beam direction is indicated with a star, and the streaking due to the twin boundaries is indicated. c) The diffracrion from the total particle.

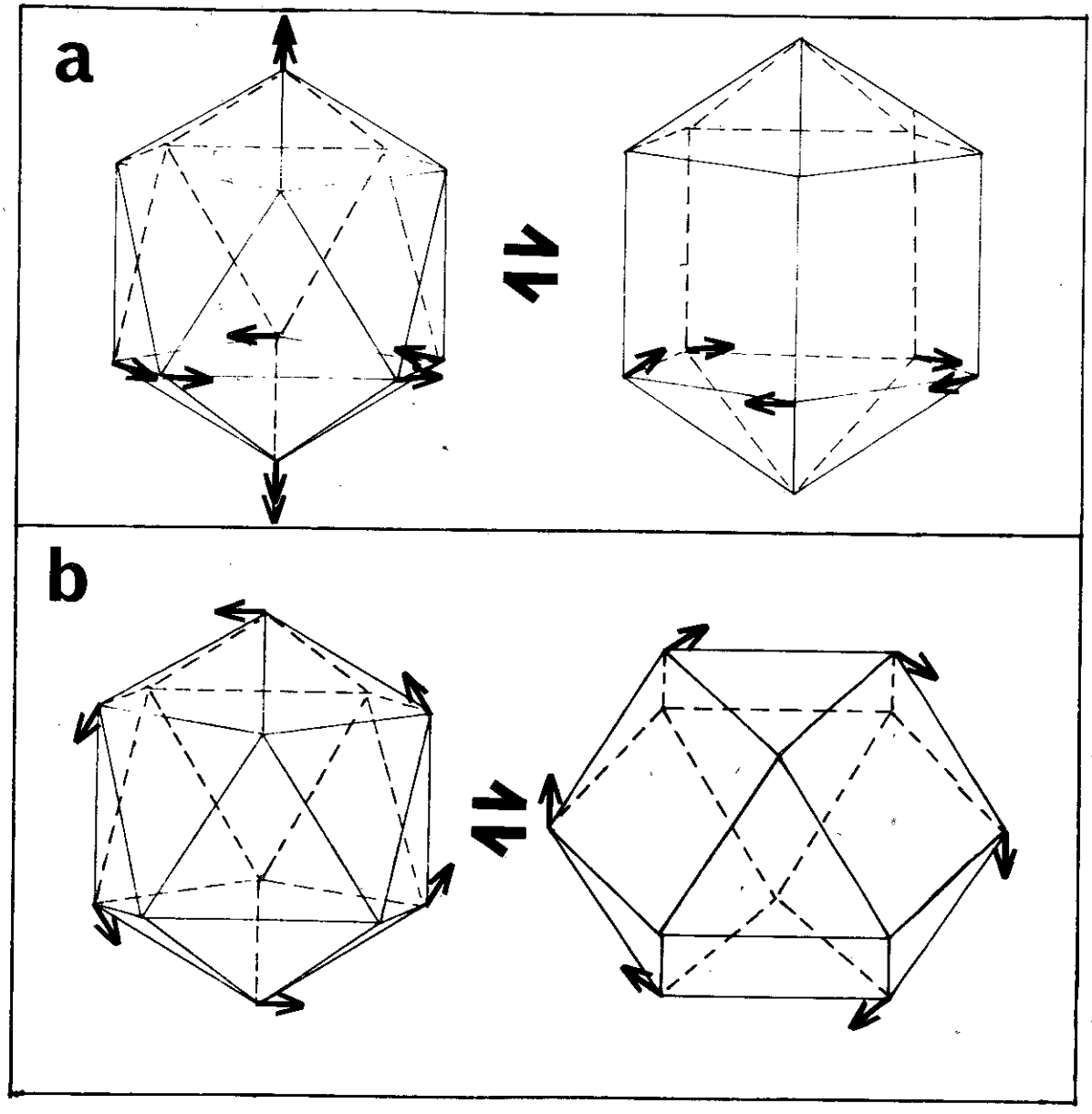

Figure 2.18 Illustration of the vibrational relationships between MTPs and single crystals: a) interconversion of an Ic (left) and a Dh (right). The two structures shown are related by $\pi/5$ rotations about one of the 5-fold symmetry axes, as indicated by the single headed arrows. Alternatively, the Ic can be converted into the Dh by pulling apart two opposing vertices, as indicated by the double headed arrows. b) Interconversion of an Ic (left) and a single crystal (right). The rotations shown by the arrows interchange the two structures. All the sides shown in the figures are of the same length.

been treated rather qualitatively in the literature. Two models have been proposed: layer growth upon very small multiply twinned nuclei (Komoda 1968), and accidental twinning (Allpress and Sanders 1967).

Layer growth is the mechanism which has received the most support (in the interpretation of results) in the literature (see, for example, Gillet 1977). The model assumes the existence of very small rigid nuclei upon which layer growth (i.e. growth where the atoms adopt the crystallography of the surface to which they are added) procedes. This is almost certainly how very large ($> 1\mu$) MTPs are produced by, for example, electrodeposition (Disgard et al 1976).

However, there is a major problem with this model - what are the initial nuclei? The seven atom pentagonal bipyramid (a Dh) and the 13 atom icosahedron are those normally considered (see Komoda 1968, Gillet 1977), but, as Hoare and Pal (1972) have critically commented, there is very little reason to believe that either of these are conformationally rigid. Clusters this small are almost certainly mobile, and are closer to liquids than to solids. Hence atom addition probably produces a new, completely different structure rather than an extension of the old one. Hoare and Pal (1970) suggested that the smallest nucleus rigid enough for layer growth is the 55 atom McKay Icosahedron (McKay 1962). Hence Ics can be produced by layer growth, but where do the Dhs come from?

The accidental twinning mechanism of Allpress and Sanders (1967) is one way in which Dhs can be produced. This model assumes the existence of very small tetrahedra upon which growth accidentally produces one twin boundary, then successively more twin boundaries, finally to end up with MTPs. However, this mechanism requires the presence of very samll single crystals as the initial nucleation products, whilst Komoda (1968) showed that MTPs were present even at the very early

stages (particles 1-2 nm across).

To reconcile these problems concerning MTP growth, retaining the attractive layer growth model for the formation of very large MTPs, requires a mechanism whereby small (e.g. 5 nm across) MTPs or single crystals can be produced. A model developed by the present author appears capable of this. The basic feature of this model is that MTPs and single crystals are not completely unrelated species (as the microcrystallite model in 2.2 implies), but can be interconverted by relatively small rotational distortions. This can be simply demonstrated with a framework model of an icosahedron. If two opposing vertices are pulled apart and the appropriate "bonds" are broken or allowed to stretch, a version of Dh is produced as shown in Figure 2.18a. Similarly, holding two of the flat faces rigid and rotating the intermediary vertices produces a single crystal (cubo-octahedron), as shown in Figure 2.18b. These distortions correspond to vibrational modes effecting the whole structure. For example, interconversion of a Dh to (or from) an Ic corresponds to a vibration of class A (in, respectively, the D_{5h} and I_h point groups). For the application of point group symmetry to vibrational modes see, for example, Murrell, Kettle and Tedder (1965).

Hence, MTPs and single crystals can be interconverted, even at relatively large sizes (e.g. 5 nm across), by thermally excited vibrations. The precise mechanism of MTP (or single crystal) formation can be sketched as follows. At the very earliest stages (a few tens of atoms) very mobile structures are formed which freely interconvert by the type of vibrations mentioned above. As the particles grow these transformations become progressively harder (requiring more energy) until the structure "crystallises" into conformationally rigid entities. Further layer growth upon these nuclei can produce

the very large particles frequently found. An interconversion of a particle with one twin boundary into a Dh, which then rearranges to an Ic has in fact been observed by Yagi et al (1975) during in-situ studies of particulate growth. (The final particle has contrast typical of a ⟨112⟩ oriented Ic, but was interpreted by these authors as a rather different type of particle.)

2.5 Thermodynamics of MTPs

Complete agreement has not been reached on the thermodynamic stability of MTPs relative to single crystals. All the analyses (to date) have found the Ics to have lower total free energies than single crystals at very small sizes, but no particularly satisfactory explanation for the Dhs has been proposed.

Fukano and Wayman (1969) were the first to analyse this problem, employing a simple hard sphere model with nearest neighbour interactions. They concluded that Ics (icosahedra in fact) were stable relative to single crystals for up to 1156 atoms, with no stability for the Dh. Allpress and Sanders (1970) improved upon this type of atomistic approach, employing Morse and Mie potentials with a homogeneous relaxation of the atom co-ordinates, and obtained very similar results. Hoare and Pal (1972) approached the problem in a similar fashion (Mie potentials), analysing the relative stabilities of a wide variety of different structures and evaluating the partition functions. Their results are rather more relevant to the growth of MTPs, where they have already been described. Most recently, an atomistic calculation has been carried out by Gordon et al (1979), with a tight binding approximation and a homogeneous strain. This produced the (exceptionally low) result of Ics being the

preferred form (in Ni) for less than 150 atoms.

A rather different approach was adopted by Ino (1969), namely a continuum model with homogeneous anisotropic elasticity and surface free energies. He found very small Ics to be stable relative to all other types, and suggested that Dhs were metastable compared to tetrahedra. More detailed calculations based upon this approach, with the extra refinements of a more complete surface minimisation (Chapter 3) and inhomogeneous elasticity (Chapter 4) are included in this thesis. These indicate that the energetics of MTPs are considerably more complicated than any of the previous analyses have suggested.

2.6 Experimental Evidence

There is a considerable amount of literature where the presence of MTPs is reported, but a relative sparsity of detailed experimental analyses concerning their structures or the mechanisms of their growth. In this section these latter works are briefly reviewed.

The basic sources for MTPs are the two original papers by Ino (1966) and Ino and Ogawa (1967). These authors observed very complicated electron diffraction patterns during the early stages of growth of Au on alkali halides in UHV. By taking high resolution dark field electron micrographs around the various diffraction spots, a positionally-resolved microdiffraction pattern was obtained. These showed that in addition to <111> epitaxed tetrahedra, two new particles were present. These were Ics and Dhs with <111> epitaxy, the second paper also reporting the presence of <100> epitaxed Dh. Shapes of icosahedra and decahedra, repsectively, were reported for these particles. The detailed structure of the particles was explained

with a qualitative form of the microcrystallite model.

Similar particles were observed almost simultaneously by Allpress and Sanders (1967) during the growth of Au, Ni and Pd on mica in UHV. The experimental diffraction patterns and images are analysed here in less detail than Ino and Ogawa, but the results are more extensively discussed. An important measurement was the relative edge lengths of the tetrahedra, Dhs and Ics observed. This showed that the different particle types all contained approximately the same number of atoms, thereby precluding a preferential growth mechanism for MTPs (as was later suggested by Gillet (1976)). The successive twinning mechanism for MTPs, as described in 2.4, was proposed.

Evidence of a rather different nature was provided by Komoda (1969) using axial lattice imaging of the (111) and (200) fringes in MTPs. The lattice fringes were observed to be slightly bent, this being taken as evidence in favour of inhomogeneous strains in MTPs. Following from the observation of very small (1-2 nm across) MTPs, the layer growth mechanism based upon the seven and 13 atom nuclei was proposed (as previously described in 2.4). Unfortunately, despite the extreme clarity of the images obtained, these interpretations are not particularly convincing. Bent lattice fringes are to be expected when there are variations in the crystallite thickness (see Hashimoto et al 1961 and 5.2) and need not be due to any internal strains. The problems connected with the choice of seven and 13 atom nuclei for the layer growth model have been discussed in 2.4 .

Important evidence concerning the behaviour of MTPs during evaporative growth has been obtained by Yagi et al (1975). These authors observed, <u>in-situ</u>, the early stages of growth of Au and Ag on various substrates at moderate ($\sim$ 1 nm) resolution. MTPs

were found to be produced by three different mechanisms: layer growth on small nuclei; rearrangement following the coalescence of two particles (which produced Ics, not Dhs), and an internal rearrangement where a particle with one twin boundary changed into a Dh, which later changed into an Ic. (The final particle is interpreted as a ⟨112⟩ oriented Ic by the present author, which is different to Yagi et al's analysis.) The post-coalescence formation of Ics provides the only available evidence for an absolute thermodynamic stability of these particles. The internal rearrangement provides evidence in support of the vibrational rearrangements described in 2.4.

An analysis of high resolution images (obtained using tilted illumination) has been carried out by Gillet et al (1976). A splitting of one of the Moire fringes in the Ics into two pairs at an angle of approximately $6^{\circ}20'$ was observed. This was attributed to the presence of some form of "fcc structure", that is, dislocations. This feature was observed to occur in particles larger than approximately 8 nm. However, interpretation of these details, as with the work of Komoda, is very complicated. (In fact, more problems are likely when tilted, rather than axial illumination is employed.) Further, corroborative evidence is required for the full confirmation of these results.

More recently, Heinemann et al (1979) have critically re-examined the experimental evidence concerning MTPs. They drew attention to a number of features (the loss of (220) "ghost images" in the Dhs; a splitting of the diffraction spots in the Ics, and the presence of straight Moire fringes and continuous thickness fringes in both types of particles) which were considered to be inconsistent with the presence of inhomogeneous strains. Hence they considered that the microcrystallites in the MTPs are not distorted fcc crystals, but are, instead, orthorhombic (for the Dhs) and rhombic (for the Ics) crystals. However,

these features do not unambiguously disprove the existence of inhomogeneous strains. The strains present in these particles are relatively homogeneous, except near the five-fold axis of the Dhs or the centre of the Ics (see 4.2 for the inhomogeneous strain solutions). Therefore the effects that they produce will be very small. For example, on drafting the strain field in a Dh to simulate the formation of the relevant Moire fringes (as in 5.4.1, Figure 5.7), straight fringes are produced. Furthermore, thickness fringes must always be continuous, whilst intensity changes are symptoms of inhomogeneous strains. Finally, the loss of the (220) ghost images and the splitting of the diffraction spots are features also to be expected with an inhomogeneous strain.

2.7 Related Fields

An interesting, and in some cases relevant relationship exists between the study of MTPs and some other, rather distant fields. In this section those known to the present author are briefly discussed.

A rather directly related field is the study of the very large ($>1\mu$) MTPs grown by electrodeposition techniques (see Digard et al 1976, who also provide a useful review). One of the more interesting results of this work is how the type of particle produced depends upon the overvoltage employed.

Another directly relevant area is the study of small transition metal or boron clusters (the so called "electron-deficient compounds"). The properties of these compounds should provide some insight into the very earliest stages (i.e. >20 atoms) of particulate growth. One interesting result is the exceptional stability of the 13 atom boron icosahedron - it behaves in many respects like a very large atom

(see Cotton and Wilkinson 1972 for a useful review).

Further afield is the common occurrence of icosahedral structures in viruses (see any recent Cell Biology textbook). One particularly relevant paper is that due to Caspar and Klug (1962), who showed that the lowest energy skin that can be built using identical units (implicitly proteins) with nearest neighbour interactions is the surface of an icosahedron.

Icosahedral structures are also of importance in architecture. Buckminster Fuller (1963) showed in his design of the geodesic dome that efficient building principles involve an icosahedral symmetry. Probably for similar reasons, the European football design has icosahedral symmetry.

Finally, the icosahedron is a very special structure, being the largest regular polyhedron. (This was known to the ancient Greeks, who based some of their astrological theories upon it.) Except for the "infinite" point groups $C_{\infty v}$, $D_{\infty h}$, SV_2 and R_3, the icosahedral point group is therefore the most symmetric point group (there are 120 symmetry operations in I_h, as against, for example, 48 in O_h).

CHAPTER 3

SURFACE ENERGIES AND STRUCTURES OF MTPS

3.1 Introduction

An important characteristic of a MTP is its equilibrium surface structure, a topic which is investigated both experimentally and theoretically in this chapter. The experimental results obtained for thermally-annealed particles (3.3) show one rather surprising feature: the presence of re-entrant surfaces in Dhs. To understand this, a theoretical model based upon the Wulff construction is developed in 3.4.2. In addition to giving structures reproducing the experimental features (3.5.2 in particular), this permits a rather useful perturbation approach explaining why there are any total surface energy differences between MTPs and single crystals (3.4.3). The predicted structures and energies for two extreme models of faceting are considered in 3.5. This is followed in 3.6 by a model explaining why the results obtained here differ from any previous work, with a general discussion in 3.7.

3.2 Experimental Procedure

Specimens of silver were prepared by evaporation in a vacuum of $< 2 \times 10^{-3}$ pascals onto amorphous carbon at 500, 600 and 700° C, and cleaved NaCl at 500° C. These were then annealed at the deposition temperature for 30 minutes. A specimen of gold was prepared by evaporation in the same vacuum conditions onto amorphous carbon at 600° C and annealed for 10 minutes. For both metals, a range of particle sizes was obtained by varying the deposition time across the substrates with a movable shutter.

The specimens deposited on NaCl were prepared for microscopy by evaporation of a thin amorphous carbon film over the particles,

followed by transfer of the particles on the carbon support film onto microscope grids (by dissolving the NaCl in water). The amorphous carbon substrates employed were premounted on microscope grids.

The particles obtained in this fashion were examined in a Siemens 102 electron microscope at 100kV using axial bright field imaging combined with either axial or hollow cone dark field imaging over the (111) and (200) rings.

3.3 Results

A wide variety of particle types were observed, in agreement with previous work for similarly annealed particles (Solliard et al 1976, Takahoshi et al 1978). A typical field of view is shown in Figure 3.1. The external profiles of the particles were rounded, crudely approximating to spheres, although facets could be observed at higher magnifications.

A particularly interesting result was the surface structure of the Dhs. Regardless of size, substrate or temperature, these particles possessed well-formed notches at the twin boundaries, as shown in Figure 3.2. It can be seen from the figure that the planes producing these re-entrant surfaces are nearly parallel to an adjacent twin boundary, from which they were indexed as (111) facets, or possibly facets very close to (111).

3.4 Theory

3.4.1 Introduction

The problem that is analysed in this section is the thermo-

most useful approach to this problem is via the microcrystallite model for MTPs (described in 2.2) in which a collection of single crystals is elastically distorted. It is convenient to divide this model into two parts: a "plastic problem", which involves determining the most stable shape of the unstrained single crystal building blocks, and an "elastic problem", which considers the effects of the elastic distortions. The plastic problem, which produces shapes closely approximating those of the complete MTPs (the strains required are only a few per cent), is considered in this section. The elastic problem is considered in 4.2, along with a first order correction for the coupling between the elastic and plastic problems (in 4.3).

When considering the pre-strained particle, two new names are adopted: each single crystal element is described as a "precursor segment", and the total particle is called a "precursor MTP".

3.4.2 Modified Wulff Construction

In this section, the equilibrium shape of the precursor segments employed in constructing MTPs is considered. This is an energy minimisation problem, where the free variables are the normal distances from some arbitrary origin to a number of surface planes and twin boundaries. To obtain a solution, two approximations are adopted: a continuum (rather than atomistic) treatment, and the assumption that all the precursor segments are identical. Both of these approximations are discussed in 3.7.

Given that the precursor segments are identical, only the energy and shape of any one arbitrary segment has to be considered. The solution to this type of problem was first given by Wulff (1901), with general proofs of the theorem by Laue (1943) and Dinghas (1943).

If $\gamma_s(\theta,\phi)$ is the excess surface free energy per unit area of the strain-free surface defined by the polar co-ordinates θ, ϕ (referred to as the "specific surface work" of the face as suggested by Linford 1973), then the solution takes the form of the construction:

(i) draw $\gamma_s(\theta,\phi)$ in 3-D as a polar plot;

(ii) construct the planes normal to the radii at all points on $\gamma_s(\theta,\phi)$, and

(iii) the minimum energy shape is the inner envelope of these planes.

The form of the construction for a single crystal is shown in Figure 3.3.

The use of the strain-free term, specific surface work, is important. The excess surface free energy is in general strain-dependent, but the Wulff construction is valid only when the energy per unit area of surface is dependent solely upon the surface normal, not upon the position. This condition does not hold when strains are included. An analysis including the effects of strains is given in 4.3.

To employ this construction for the MTP precursor segments, a modification must be made to include the twin boundaries. By virtue of the symmetry of the segments, each of the facets which combine (after straining) to produce the twin boundaries have an energy per unit area which is half that of a twin boundary (written as $\gamma_t/2$). Incorporating extra point values of $\gamma_t/2$ in the Wulff construction produces "twin facets", which include all the effects of the twin boundaries. An example of this "modified Wulff construction", suitable for a Dh precursor segment, is shown in Figure 3.4.

Finally, when discussing the total energies of these shapes, a dimensionless parameter ξ_ω will be employed. This is defined by

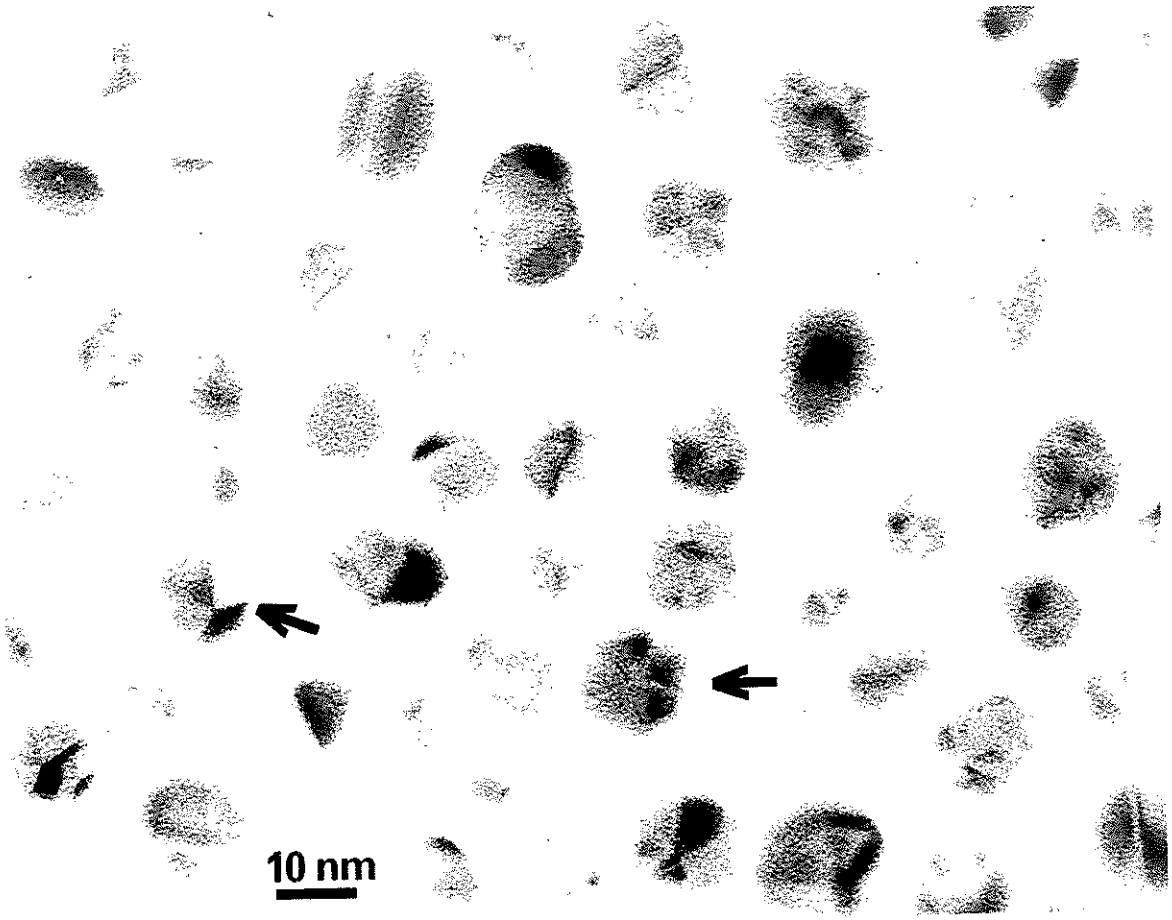

Figure 3.1 A typical field of view from the sample of silver prepared on NaCl at 500 °C. Two Dhs with the notches just visible are indicated.

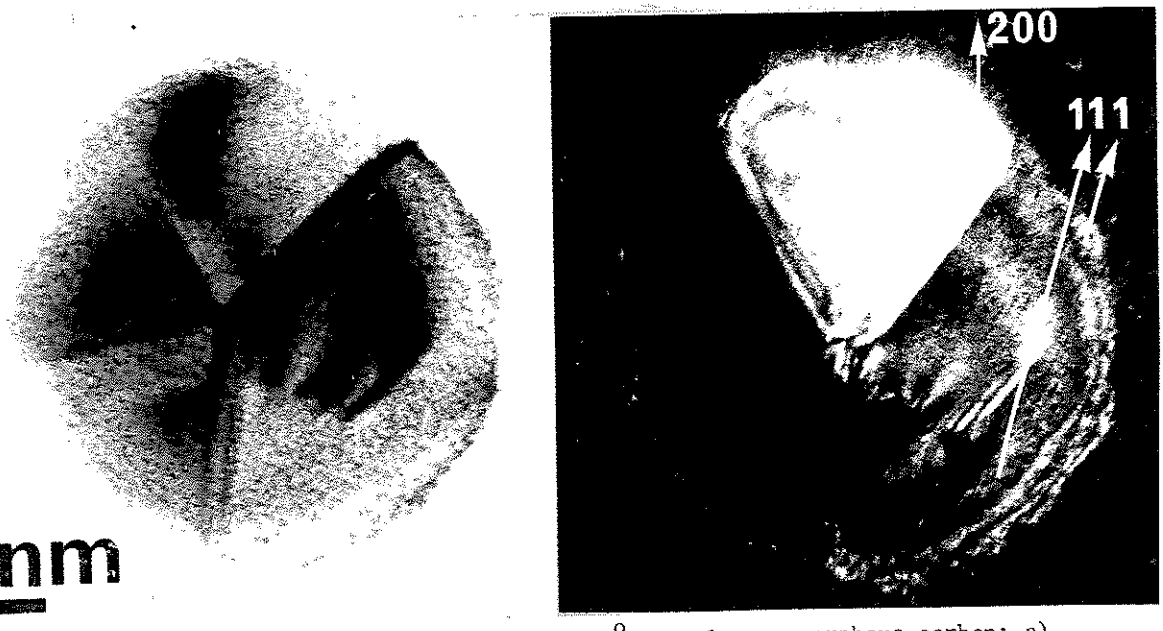

Figure 3.2 A Dh of silver from the 700 °C sample on amorphous carbon; a), bright field and b), dark field. The diffraction spots contributing to the image in b) are indicated on the figure.

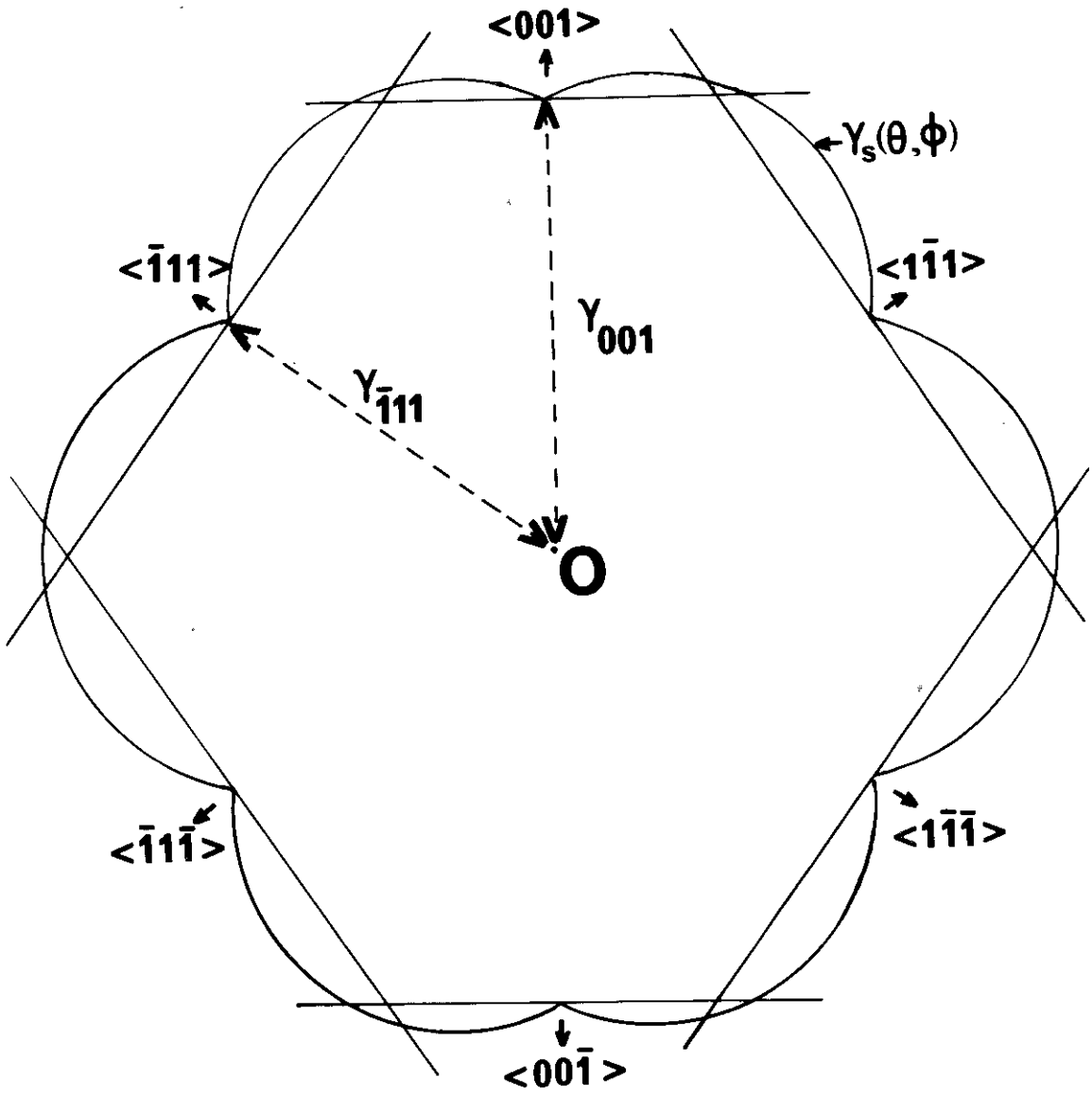

Figure 3.3 <110>section of a Wulff construction for a single crystal. The form of $\gamma_s(\theta,\phi)$ employed in the figure produces the Strong Faceting Model with $\gamma_{100}=2.\gamma_{111}/\sqrt{3}$ (the broken bond model).

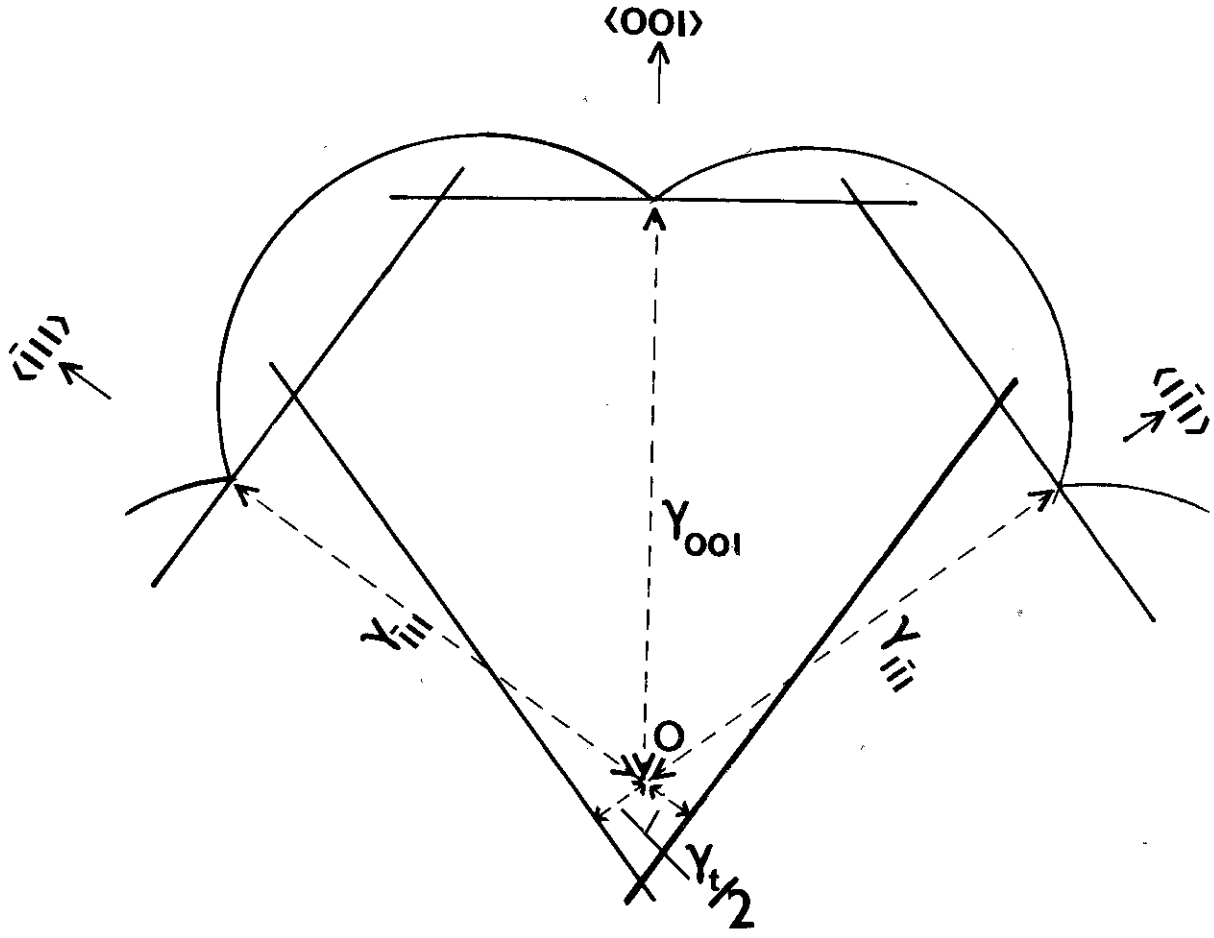

Figure 3.4 <110> section of a modified Wulff construction suitable for a Dh. The form shown results in the Strong Faceting Model with $\gamma_{t/\gamma_{111}}$ =0.1 (about x20 to large) and $\gamma_{100/\gamma_{111}}$ =1.13.

$$\varepsilon_\omega = \frac{\int \gamma_s(\theta,\phi)\, dS}{\gamma_{111}\left[\int dV\right]^{2/3}} ,$$

where γ_{111} is the specific surface work of an (111) face. The advantage of this parameter is that it depends only upon the particle shape (in a continuum model - but see 3.7), and not upon the volume.

3.4.3 Perturbation Approach

The modified Wulff construction developed in the previous section completely includes the effects of the twin boundaries, but lacks any direct physical interpretation. An alternative approach, which provides more insight, is to consider the twin boundaries as small perturbations and apply perturbation theory. The surface energy parameter ε_ω can be expanded in the form

$$\varepsilon_\omega = \varepsilon_s + \varepsilon_t \gamma_t/\gamma_{111} + \varepsilon_c$$

where ε_s is the zero order term, obtained by putting $\gamma_t = 0$ in a modified Wulff construction, ε_t is the first order correction obtained from the twin boundary area of the $\gamma_t = 0$ construction, and ε_c is the residual term containing all the higher order corrections. For fcc metals (except possibly aluminium) $\gamma_{111} \gg \gamma_t \approx 0.01\gamma_{111}$, so that ε_s is the major term in ε_ω. A combination of ε_s and ε_t is similar to the treatment of the twin boundaries employed by Ino (1969). The term ε_c is a measure of how strongly the twin and surface terms interact.

The total surface energies of different particle types can be qualitatively compared by their ε_s values. These vary because the possible external surfaces in MTPs are restricted by the twin boundaries. The total annular domain of a single crystal can be represented by a

stereographic plot (Figure 3.5a), whilst MTP precursor segments have more limited domains, as also shown in Figure 3.5a. The different domains can be conveniently reduced onto a stereographic triangle divided into the two angular domains A and B shown in Figure 3.5b. The domain of a single crystal is 48(A + B), a precursor Dh segment 8A + 12B, and a precursor Ic segment 6B. Utilising the relationship given in Appendix 3.1, for a single crystal

$$\varepsilon_s = \left(\frac{q}{\gamma_{111}}\right)^{1/3} \left[48 \left\{ \int^{A} \gamma_s(\theta,\phi)\, dS + \int^{B} \gamma_s(\theta,\phi)\, dS \right\} \right]^{1/3}$$

where the suffixes A, B denote the values taken over these domains.

Substituting

$$\int \gamma_s(\theta,\phi)\, dS = \bar{\gamma}_s \Omega$$

where $\bar{\gamma}_s$ is a mean specific surface work, and Ω the solid angle of integration, then

$$\varepsilon_s = \left(\frac{q}{\gamma_{111}}\right)^{1/3} \left[48 \left\{ \bar{\gamma}_s^{A} \Omega^{A} + \bar{\gamma}_s^{B} \Omega^{B} \right\} \right]^{1/3}.$$

Similarly, for a precursor Dh

$$\varepsilon_s = \left(\frac{q}{\gamma_{111}}\right)^{1/3} \left[40 \bar{\gamma}_s^{A} \Omega^{A} + 60 \bar{\gamma}_s^{B} \Omega^{B} \right]^{1/3},$$

and for a precursor Ic

$$\varepsilon_s = \left(\frac{q}{\gamma_{111}}\right)^{1/3} \left[120 \bar{\gamma}_s^{B} \Omega^{B} \right]^{1/3}.$$

Hence ignoring the twin boundary energy, both types of MTPs have lower total surface energies than a single crystal if

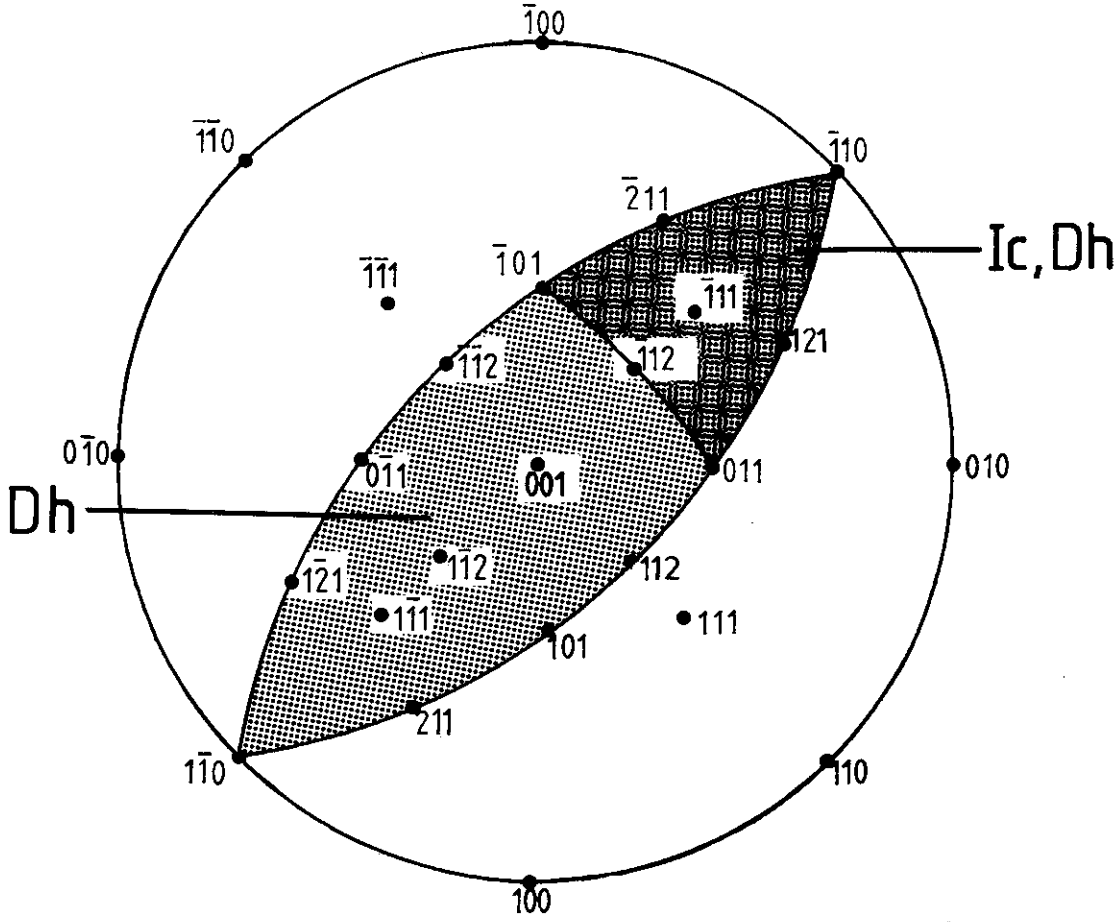

Figure 3.5a) Stereographic plot for the zero order surface energy term in MTPs. The total shaded area shows the angular region of a precursor Dh segment, that on the top right the angular region of a precursor Ic segment.

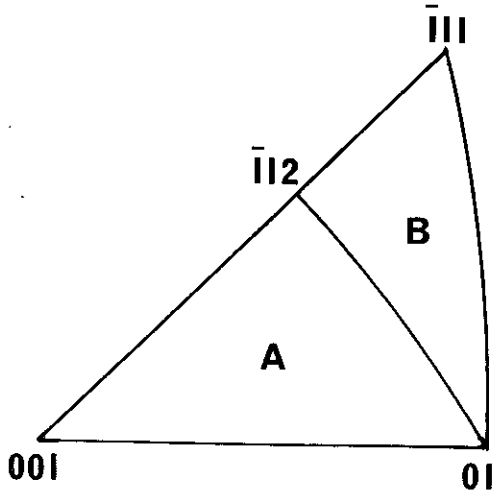

Figure 3.5b) Stereographic triangle for use with MTPs. The angular regions shown in Figure 3.5a) can be represented by suitable combinations of the regions A and B shown above.

$$\frac{\bar{\gamma}^A_A \Omega^A}{\bar{\gamma}^B \Omega^B} > 1.5 .$$

As $\Omega^A/\Omega^B = 1.6137$, the above reduces to $\bar{\gamma}^A/\bar{\gamma}^B > 0.9296$.

MTPs therefore have lower surface energies than single crystals if the mean specific surface work of domain A is more than 0.9296 times that in domain B. Furthermore, the size of the surface energy preferences will be directly related to the magnitude of this ratio. This is very different to any simple consideration that MTPs have more (111) facets; low energy (111) and high energy (100) facets favour MTPs, but so do many other possibilities.

The fact that the right hand side of the inequality is less than 1 relates to the presence of the angular gaps. The total solid angle subtended by a single crystal is $48(\Omega^A + \Omega^B)$. For a precursor Dh the solid angle subtended by ξ_s is $40\Omega^A + 60\Omega^B$ which is also the solid angle subtended with a full (i.e. including $\gamma_t/2$ facets) modified Wulff construction. (This can be shown by considering an origin at the centroid of the precursor MTP.) Similarly, for a precursor Ic the total solid angle is $120\Omega^B$.

Subtracting these values, it is apparent that the angular gap in a precursor Dh is $8(\Omega^A - 1.5\Omega^B)$, and in a precursor Ic $48(\Omega^A - 1.5\Omega^B)$. With no angular gaps (i.e. $\Omega^A = 1.5\Omega^B$) the ratio is 1.

This analysis is a useful method for obtaining the magnitude of the angular gaps. For example, the angular deficit in a precursor Ic is shown to be exactly 6-times that in a precursor Dh.

3.5 Theoretical Results

3.5.1 Introduction

The concern of this section is to evaluate the shapes of total surface energies employing the modified Wulff construction of 3.4. For this purpose a form of $\gamma_s(\theta,\phi)$ is required. However, there appears to be very little experimental evidence as yet available for the temperature regime of interest. Therefore, two models will be employed which represent the extremes of faceting: a strong faceting model with (111) and (100) facets only (used already in Figures 3.3 and 3.4), and an isotropic faceting model where $\gamma_s(\theta,\phi)$ is orientation independent.

3.5.2 Strong Faceting Model

The shapes for this model of a single crystal (for reference), a Dh precursor segment and an Ic precursor segment are shown in Figures 3.6, 3.7 and 3.8 respectively. These terms were obtained by extracting the appropriate region between the twin facets from the single crystal construction, as illustrated for a Dh in Figure 3.9. All these values are valid if

$$\sqrt{3} \geq \gamma_{100}/\gamma_{111} \geq \frac{\sqrt{3}}{2}\left(\gamma_t/\gamma_{111}+1\right).$$

The precursor segment for a Dh differs considerably from a tetrahedron, possessing five more facets. Two of these are very small and must be treated with caution. For example, in a silver particle of diameter 40 nm, the side length of these facets is 0.1 nm, i.e.

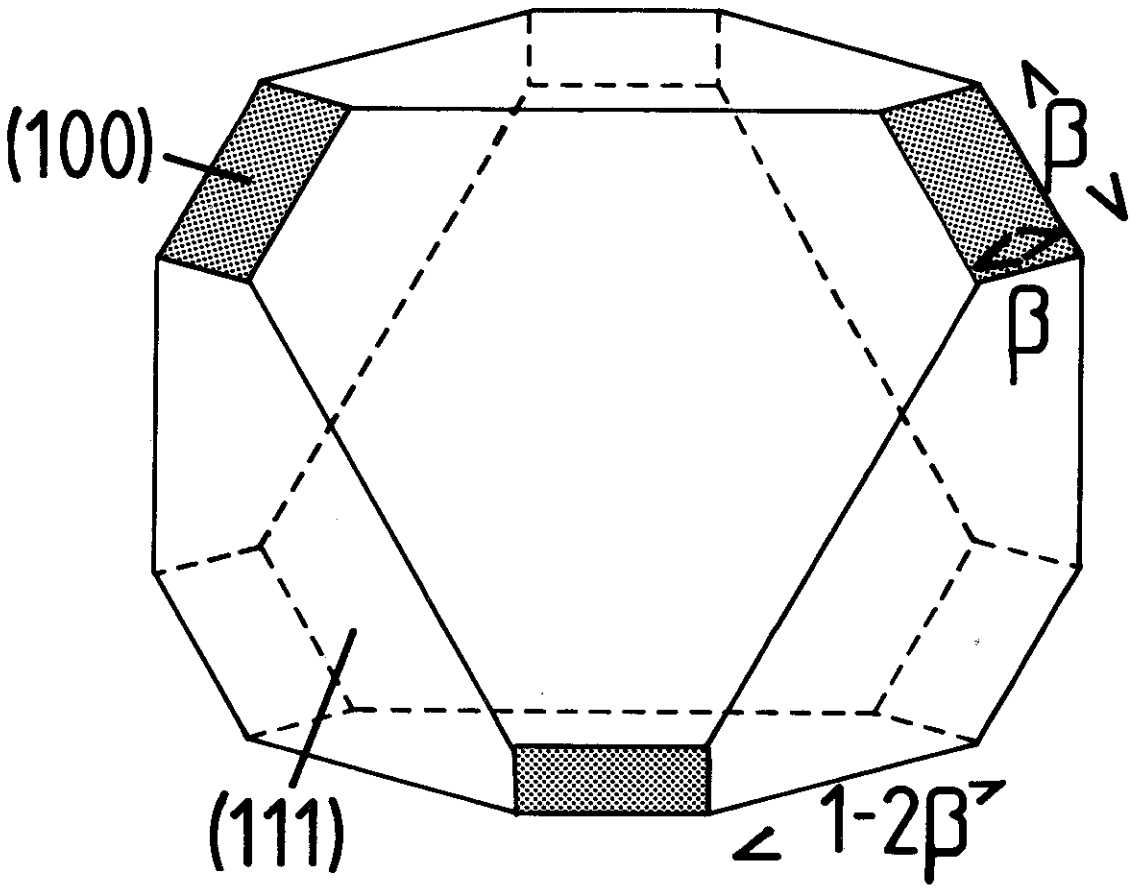

Figure 3.6 The shape of a single crystal with the Strong Faceting Model. Dimensions are shown for a scale (see Appendix) of $\gamma_{111}=1/\sqrt{6}$.

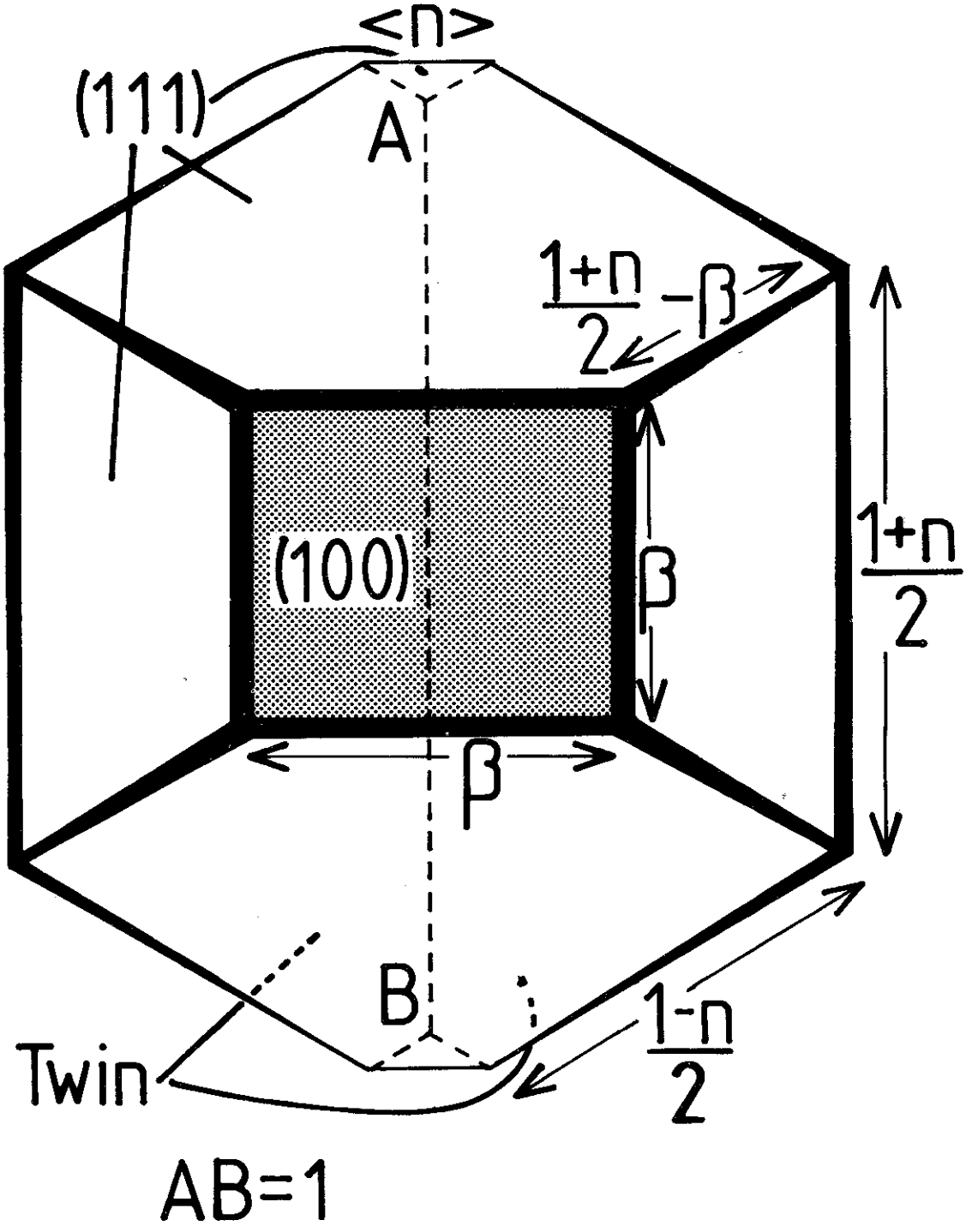

Figure 3.7a) Plan down the <100> direction of a Dh precursor segment in the Strong Faceting Model. The scale for the diagram is $\gamma_{111}=1/\sqrt{6}$. γ_t has been grossly exaggerated.

"one atom". The other three facets are very large and produce a far more rounded shape than a decahedron. As is shown in the scale drawings in Figure 3.10, the <011> projection of the precursor Dh displays the large re-entrant surfaces experimentally observed, and the <100> (side) projection is rather squat. For example, the length along the shared <110> axis is slightly more than the width across it. A qualitative fitting to the experimental shape could, in principle, be obtained employing a "softer" form of $\gamma_s(\theta,\phi)$ with more facets.

A particularly important consequence of this new shape is that the total surface energy of the Dhs (i.e. the ε_ω value) is considerably lower than Ino's (1969) value. The various parameters are:

$$\varepsilon_\omega = \left[101\tfrac{1}{4}\sqrt{3}\left\{(1+\eta)^3 - \tfrac{8}{3}(\beta^3+\eta^3)\right\}\right]^{1/3};$$

$$\varepsilon_s = \left[101\tfrac{1}{4}\sqrt{3}\,(1-8\beta^3/3)\right]^{1/3}, \text{ and}$$

$$\varepsilon_t = \varepsilon_s / (1-8\beta^3/3)$$

so that

$$\varepsilon_\omega = \varepsilon_s + \varepsilon_t \gamma_t/2\gamma_{111} - O(\eta^2),$$

$$\text{and} \quad \varepsilon_c = -\varepsilon_t \eta - O(\eta^2)$$

where $\beta = 1-\gamma_{100}/\sqrt{3}\gamma_{111}$ and $\eta = \gamma_t / 2\gamma_{111}$.

These are to be compared with

$$\varepsilon_\omega = \varepsilon_s = \left[108\sqrt{3}\,(1-3\beta^3)\right]^{1/3}$$

for a single crystal, and the D-Wulff polyhedron of Ino (1969)(which has the (100) facets, but not the notch (111) planes)

$$\varepsilon_s = [45\alpha^2\sqrt{3}\,(1+2\beta)]^{1/3} \text{ and}$$

$$\varepsilon_t = [50^{5/8}\,\alpha\,(1+\beta)^3/(1+2\beta)^2]^{1/3}$$

with $\varepsilon_\omega = \varepsilon_s + \varepsilon_t \gamma_t/\gamma_{111}$ (Ino used a perturbation approach)

where $\alpha = \gamma_{100}/\gamma_{111}$.

All these values can be obtained from the dimensions shown, with the relationship given in Appendix 3.1 as a useful shortcut.

The various parameters are all evaluated in Table 3.1 for $n = 0.5\%$ (a mean value for fcc metals, explicit values are given in Table 4.2) and $\alpha = 2/\sqrt{3}$ (broken band model).

The precursor segment for an Ic differs only very slightly from a tetrahedron, containing three extra, very small (side $\gamma_t/2\gamma_{111}$) facets. As with the Dh, these must be treated cautiously: drawn to scale they are also undetectable. The energy values obtained differ from Ino's only by the coupling term ε_c, which is again quite large. Explicitly, these are given by:

$$\varepsilon_\omega = [67\tfrac{1}{2}\sqrt{3}\,\{(1+n)^3 - 5n^3\}]^{1/3};$$

$$\varepsilon_s = [67\tfrac{1}{2}\sqrt{3}]^{1/3}, \text{ and}$$

$$\varepsilon_t = 3\varepsilon_s/2 .$$

Hence

$$\varepsilon_\omega = \varepsilon_s + \varepsilon_t\,\gamma_t/3\gamma_{111} - O(n^2),$$

and

$$\varepsilon_c = -\varepsilon_t\,4n/3 - O(n^2).$$

3.5.3 Isotropic Faceting Model

With this model, the form of a single crystal is [illegible]

occur along the twin boundaries in both types of precursor MTPs, as illustrated in Figure 3.11. However, these grooves are so small that their presence must be treated with caution; in the figure $\gamma_t/2\gamma_{111}$ has been grossly exaggerated, for with a realistic value (0.5-2%) the grooves disappear in the drafting.

The various energy parameters for a precursor Ic are:

$$\varepsilon_\omega = \left[\varepsilon_s^3 + 1080 \left\{ \int_0^n A(p)\,dp + \frac{n}{2}(1-n^2)^{1/2} A(n) + \frac{\sqrt{3}\,n^2}{4\sqrt{2}} \left(\frac{3n}{\sqrt{2}} + \cdots \right.\right.\right.$$

$$\left.\left.\left. \cdots \left(1 - \frac{11n^2}{8}\right)^{1/2} \right) \right\} \right]^{1/3}$$

$$= \varepsilon_s + \varepsilon_t \gamma_t/\gamma_{111} - O(n^2) \; ;$$

$$\varepsilon_s = \left[9 \left(4\pi - \Delta\Omega^{Ic} \right) \right]^{1/3} \; ;$$

$$\varepsilon_t = 1\tfrac{1}{4}\, \varepsilon_s / \left(1 - \Delta\Omega^{Ic}/4\pi\right) \text{, and}$$

$$\varepsilon_c = -\,O(n^2)$$

where $$A(p) = \left[\frac{\pi}{6} - \sin^{-1} \left\{ \frac{\sqrt{3}}{2\sqrt{2}} \frac{p}{(1-p^2)^{1/2}} \right\} \right] (1-p^2)^{1/2}$$

and $\Delta\Omega^{Ic}$ is the solid angle deficit in these particles given by

$$\Delta\Omega^{Ic} = 48(\Omega^A - 1.5\Omega^B) = 1.5405.$$

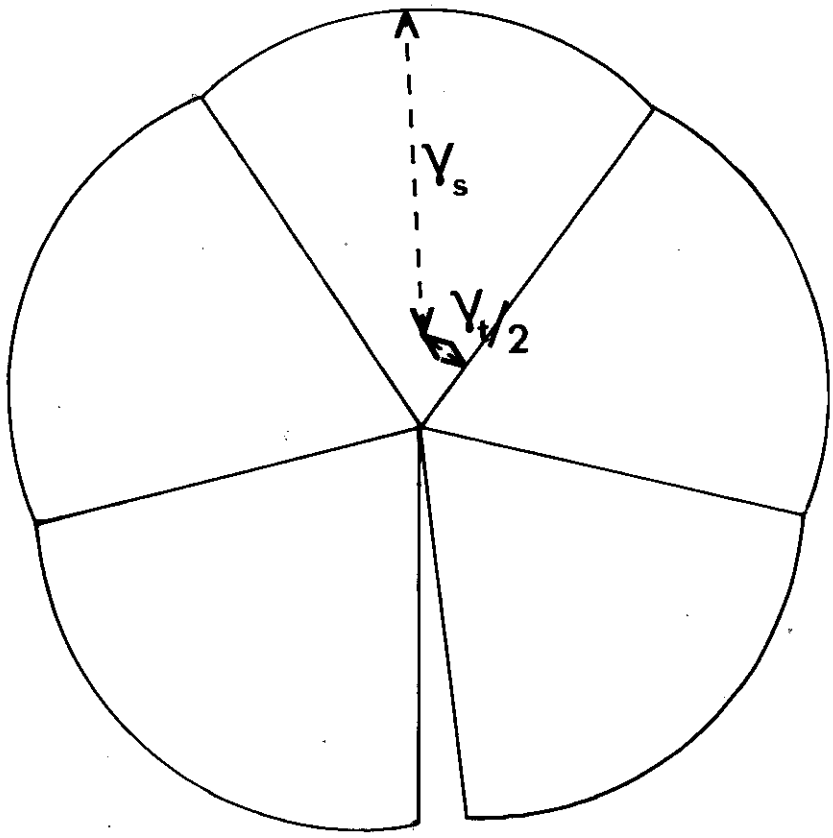

Figure 3.11 The ⟨110⟩ section of a precursor Dh obtained with the Zero Faceting Model. As before, γ_t has been grossly exaggerated.

TABLE 3.1

PARTICLE TYPE	ε_w	ε_s	ε_t
a) (111) and (100) Faceting			
Precursor Dh	5.436	5.407	5.999
Precursor Ic	4.914	4.890	7.335
Single Crystal	5.499	5.499	-
b) Ino's Shapes			
Octahedron	5.719	5.719	-
Tetrahedron	7.206	7.206	-
Decahedron	6.192	6.161	3.081
Icosahedron	4.963	4.890	7.335
D-Wulff polyhedron	5.611	5.574	3.681
c) Isotropic Model			
Precursor Dh	4.834	4.803	3.064
Precursor Ic	4.696	4.630	6.596
Single Crystal	4.836	4.836	-

Numerical values for the surface energy parameters, evaluated for $\beta = 1/3$ and $\gamma_t/2\sigma_{111} = 0.5\%$.

For a precursor Dh:

$$\varepsilon_\omega = \left[\varepsilon_S^3 + 90 \left\{ 2\int_0^n A(p)dp + n(1-n^2)^{1/2} A(n) + \sqrt{2}\, n^2 (1-3n^2)^{1/2} \right\} \right]^{1/3}$$

$$= \varepsilon_S + \varepsilon_t \gamma_t/\gamma_{III} - O(n^2) \; ;$$

$$\varepsilon_S = \left[9(4\pi - \Delta\Omega^{Dh}) \right]^{1/3} \; ;$$

$$\varepsilon_t = 5/8 \; \varepsilon_S/(1 - \Delta\Omega^{Dh}/4\pi) \; , \text{ and}$$

$$\varepsilon_c = - O(n^2)$$

with $A(p) = \left[\frac{\pi}{2} + \sin^{-1} \left\{ \frac{\sqrt{2}\, p}{(1-p^2)^{1/2}} \right\} \right] (1-p^2)^{1/2}$

and $\Delta\Omega^{Dh}$, the solid angle gap, given by

$$\Delta\Omega^{Dh} = 8(\; A - 1.5 \; B)$$

$$= 0.2568.$$

Finally, for a single crystal

$$\varepsilon_\omega = \varepsilon_S = (36\pi)^{1/3}.$$

Numerical values are given in Table 3.2, evaluated for n = 0.5%.

As might be expected from the analysis in 3.4.3, the ε_ω values are now much more similar: for example, for a precursor Ic, ε_ω is smaller than in a single crystal if $\gamma_t/\gamma_{III} < 3.127\%$, which compares to $< 29.72\%$ in a strong faceting model. Furthermore, the coupling term ε_c is now very small, which is possibly a consequence of a breakdown of the identical segments assumption, as discussed in 3.7.

3.6 Kinetic v Thermodynamic Surfaces

The major difference between the experimental results presented here, and any previously reported, is the totally different surface structure of the Dhs. With the form reported here observed over a reasonable temperature range and two different substrates, an explanation for this difference is required. The annealing appears to be responsible, as is explained below.

It is established that early growth occurs through atom, or very small cluster, addition to independent nuclei, with coalesence and secondary nucleation arising at a later stage (see Pashley et al 1964). This has been confirmed when MTPs are present by Allpress and Sanders 1967) (see also 2.6). Furthermore, it is also established that atom by atom, or layer growth, is competitive, leading to the formation of low index faces; the energy liberated by atom addition to a face is related to $-\gamma_s(\theta,\phi)$ with high γ_s and favourable nucleation sites growing to their eventual elimination.

Therefore no relatively large γ_s faces present in the modified Wulff construction, or the notches, which are easy nucleation sites (Frank 1949), are stable to atom addition. The only stable faces will probably be the (111) facets not involved in the notches, as these probably have the lowest specific surface work. Hence growth by atom addition can be expected to produce decahedra and icosahedra, a prediction which appears to be consistent with the previously reported structures (e.g. Ino 1966).

It is only if the surfaces are equilibrated after growth is completed that thermodynamic effects become important, leading to the experimentally observed and theoretically predicted structures. The formation of decahedra and icosahedra by evaporation which become

rounded during annealing has been recently observed by Takhashi et al (1978), although this was attributed to contamination.

3.7 Discussion

The agreement obtained between the experimental observations and the theoretical results presented here would appear to be promising: the rather surprising re-entrant surfaces observed in the Dhs are reproduced in the strong faceting model. It seems that the very simple decahedra and icosahedra frequently taken to be the MTP structures are really a consequence of the growth process, with the thermodynamically most stable shapes being far more complicated. These more complicated shapes have a very important consequence as will be seen more fully in 4.4: the total surface energy of the Dhs appears to be lower than that of a single crystal.

An important area which appears to require a more extensive analysis is the assumption in 3.4.3 that the precursor segments are identical: this need not be the case. A more rigorous analysis (included in Appendix 3.2) without this assumption has been attempted by the author based upon the Wulff construction proof of Laue (1943). This shows that the modified Wulff construction corresponds to a stationary value in the energy. However, stationary points can be minima, maxima or saddle points. For a full analysis, the second derivatives must be analysed. Further investigation, unfortunately, showed that no general answer could be provided (with this method). More detailed analyses employing, for example, the geometric method of Dinghas (1943) may clarify this important question.

It is suspected that the question of minima or maxima depends upon the form of $\gamma_s(\theta,\phi)$. This can be seen by considering the

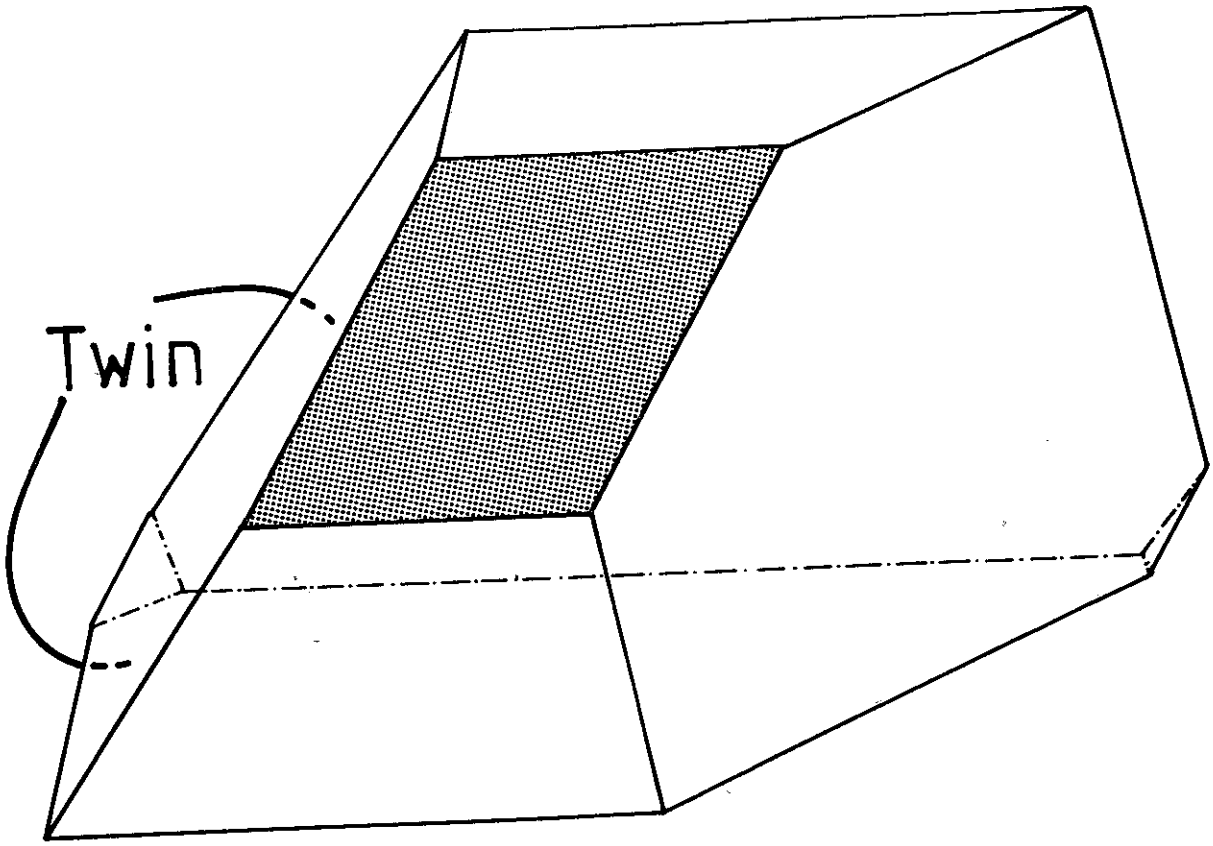

Figure 3.7b) 30° isometric for a Strongly Faceted Dh precursor segment. For clarity, γ_t has been grossly exaggerated in the figure.

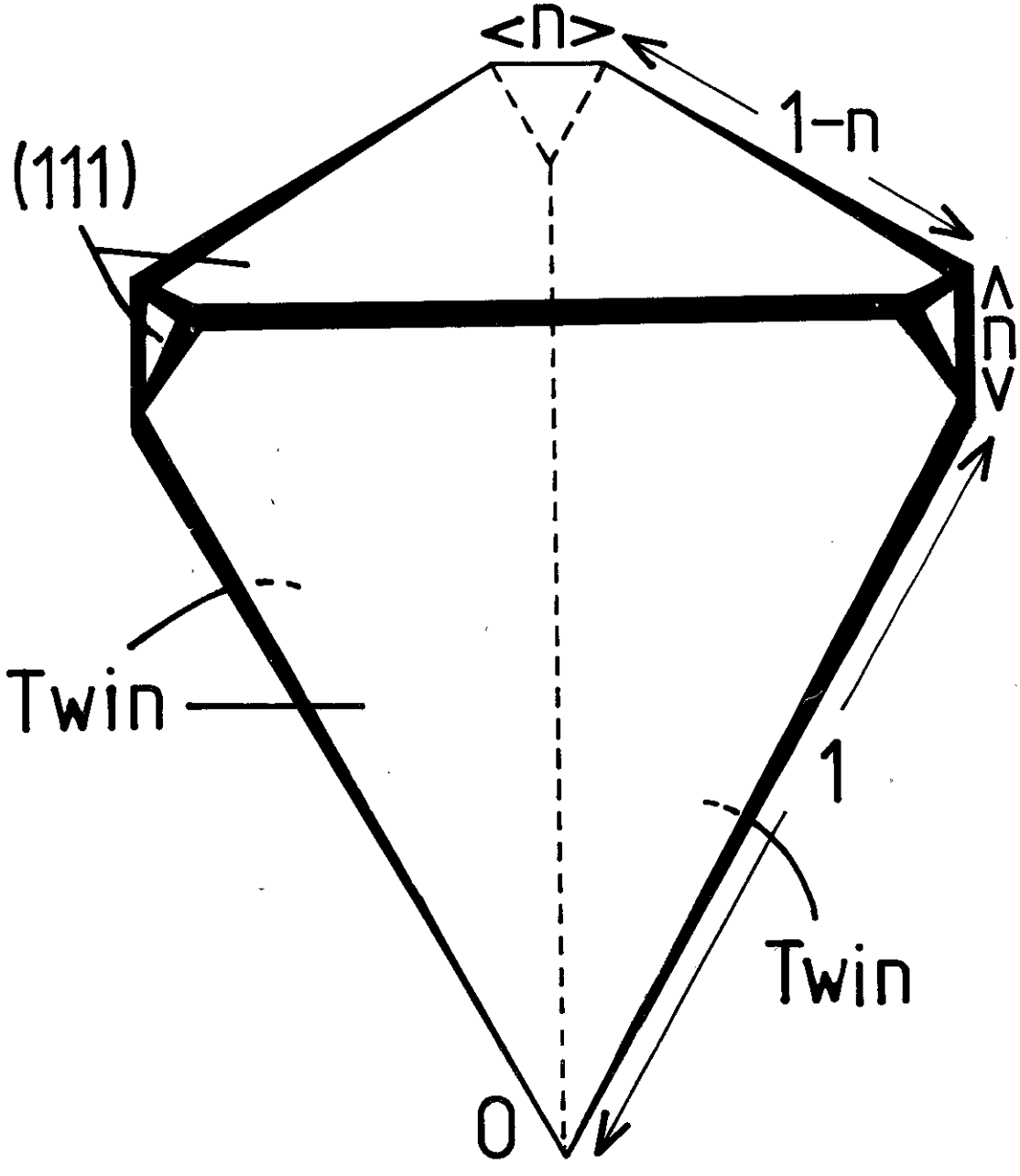

Figure 3.8 The precursor segment of an Ic with the Strong Faceting Model. γ_t has been grossly exaggerated in the figure.

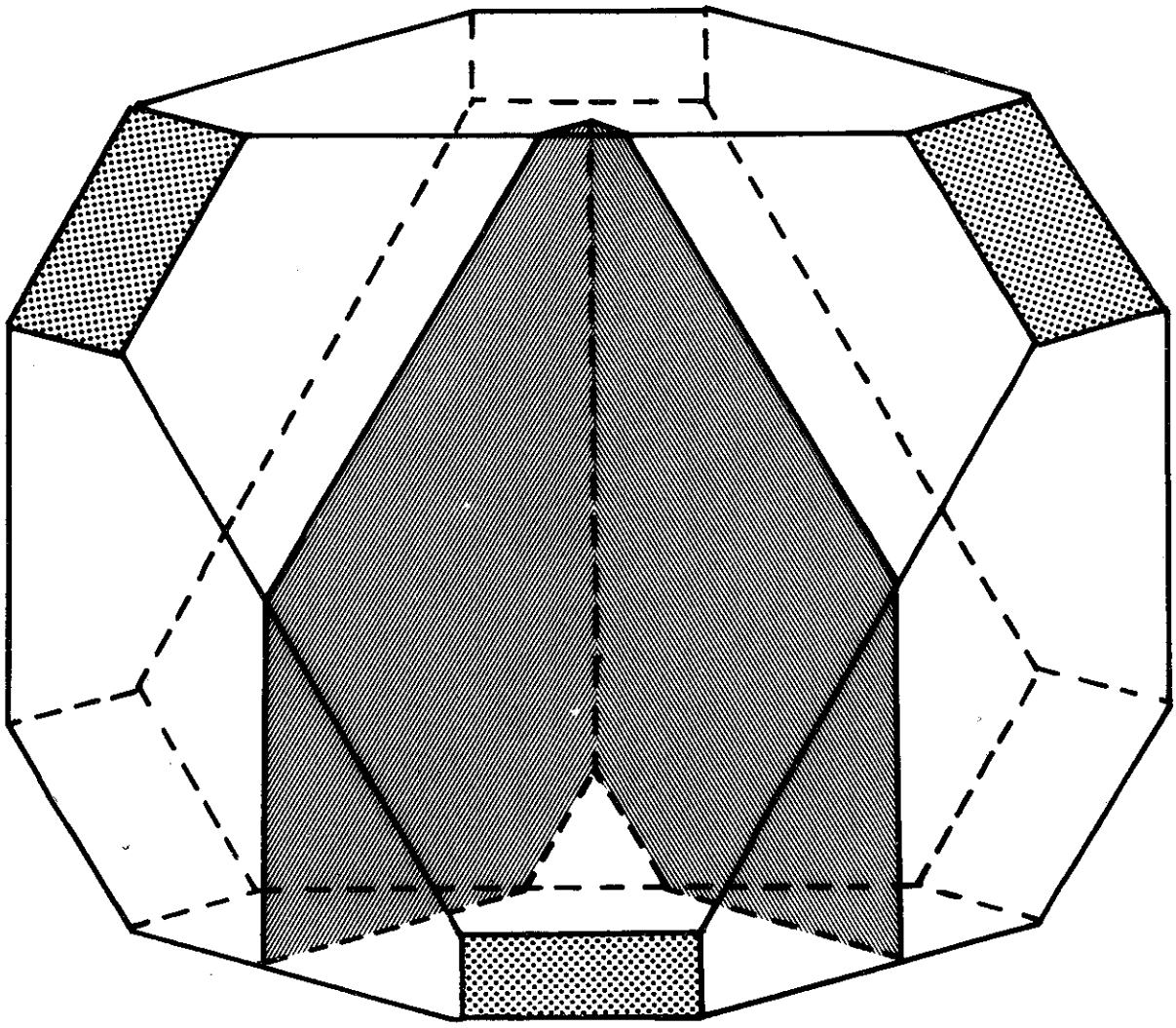

Figure 3.9 A complete modified Wulff construction for the Strongly Faceted Dh precursor segment. The total shape is that os a single crystal, from which the precursor Dh segment is extracted by the twin facets (shaded).

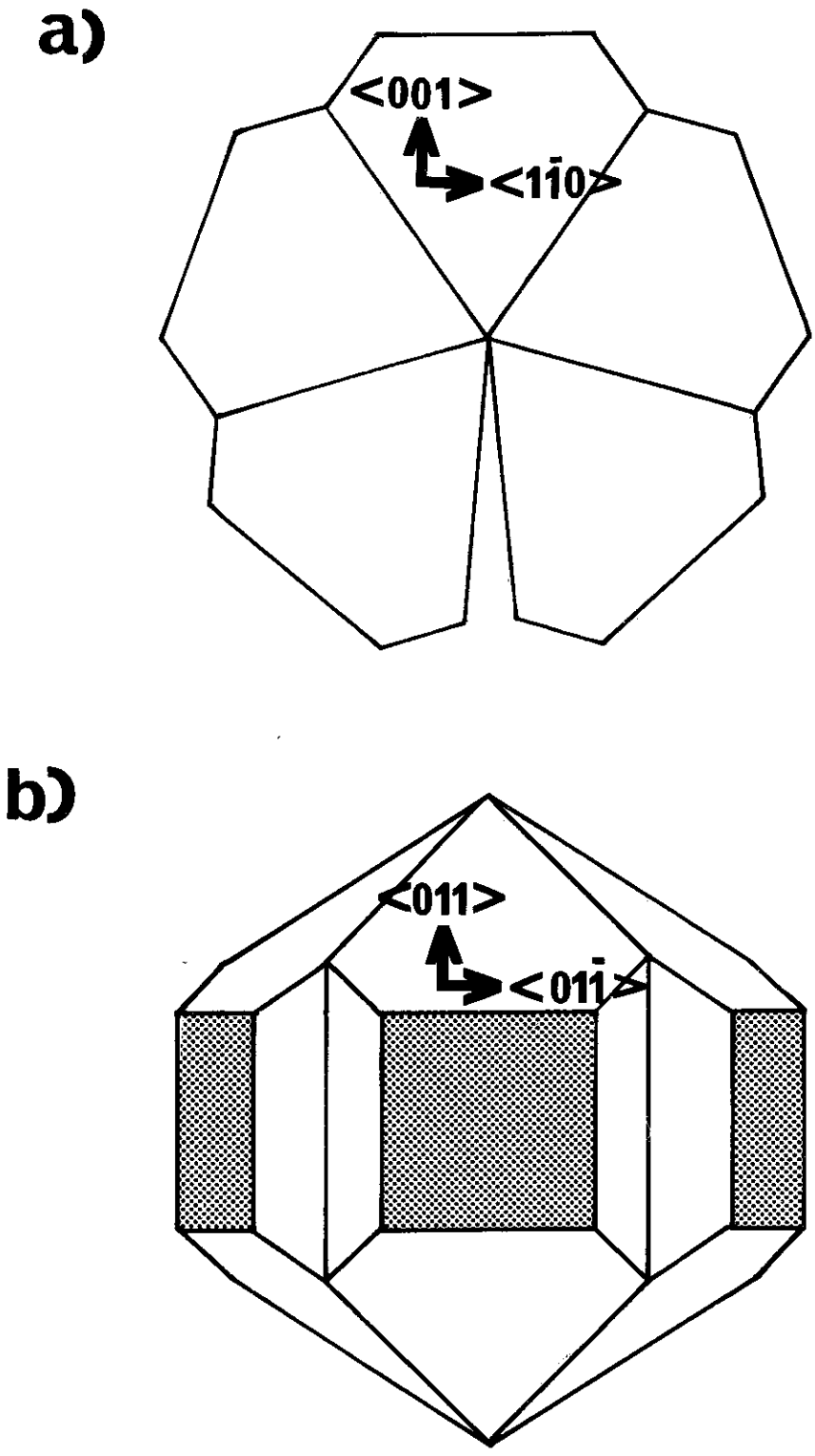

Figure 3.10 Scale diagrams of a Strongly Faceted precursor Dh, drafted for $\beta=1/3$ and n=0.5%: a), <110> projection and b), <100> projection (front surface only). The extra faceting due to the twin boundaries has disappeared in the drafting. The similarity of Figure 3.10a) to the particle in Figure 3.2 should be noted.

problem as a constrained minimisation; the variables are not all free, as the planes which end up as the twin boundaries must occur in matching pairs. Constrained minimisations behave very differently to unconstrained minimisations: the number of possible search directions is limited by the constraints. When the faceting is very pronounced there may simply be insufficient degrees of freedom for the particle to "find" a lower energy configuration; with very little faceting (i.e. isotropic faceting model) a route may be available to a lower energy. This suggests that the liquid-like model for coalescence (Pashley et al 1964) may sometimes be inaccurate. Evidence indicating this is presented in Chapter 6.

The validity of a continuum approximation is an important question, specifically in its treatment of surface facets, $\gamma_S(\theta,\phi)$ as size and shape independent, and the neglect of edge or corner terms.

A severe problem with the modified Wulff construction arises if the surface facets are treated atomistically, as any facet must be an integer multiple of the unit surface cell in its dimensions. Even with a relatively large particle, it may not be possible to fit all the theoretical facets, simultaneously, on the particle surface (particularly if any high index facets are present). Therefore the ε_ω values derived above are really upper bounds to the true values.

The other problems can be best discussed with a pseudo-potential formalism (see, for example, Harrison 1966): dividing the total energy into two components, a volume dependent term and an oscillatory interatomic pair potential. The effect of a surface can be considered as modifiying the local volume and pair terms. Both these energy terms can be expected to show a total volume dependence, whilst the size of the particle will effectively truncate the interatomic potential. Hence the energy sum producing $\gamma_S(\theta,\phi)$ will probably show a reasonably

sizes, and may even be slightly position dependent. Additionally, the neglect of edge and corner atoms can be seen as a multiple counting correction: the combined changes in local volume and pair potential interactions for the two surfaces involved are almost certainly larger than the true values. The corrections involved are probably negative energy terms, but when comparing different particles their neglect should not introduce appreciable errors.

Finally, it should be noted that the surface structures of the MTPs observed here, or in any comparable experiment, are true experimental variables: $\gamma_s(\Theta,\phi)$ will be strongly effected by the conditions employed, such as the trace gas absorbents. The strong variability of the ξ_ω parameter with the details of faceting has important consequences, as will be seen in 4.4.

Appendix 3.1

A particularly useful relationship for evaluating the total surface energies is that for any angular domain D of a Wulff or modified Wulff construction drawn to a scale $\gamma_{111} = c$

$$\varepsilon_\omega^D = \left[\frac{9}{c^2}\int^D \frac{\gamma_s(\theta,\phi)}{\gamma_{111}} dS\right]^{1/3} = \left[\frac{27}{c^3}\int^D dV\right]^{1/3}.$$

To prove this, consider an arbitrarily small element of surface dS_i, for which the specific surface work is γ_i. The normal distance from the plane of dS_i, r_i, is given by

$$r_i = \gamma_i c/\gamma_{111}.$$

Therefore the contribution by the cone from dS_i to the origin is

$$dV = 1/3\, dS_i\, \gamma_i c/\gamma_{111},$$

and the contribution to the total surface energy is

$$\gamma_s(\theta,\phi)\, dS = \gamma_i\, dS_i.$$

Integrating over any domain D then

$$\varepsilon_\omega^D = \frac{1}{\gamma_{111}} \frac{\int^D \gamma_s(\theta,\phi) dS}{\left[\int^D dV\right]^{2/3}}$$

$$= \left[\frac{9}{c^2}\int^D \frac{\gamma_s(\theta,\phi)}{\gamma_{111}} dS\right]^{1/3} = \left[\frac{27}{c^3}\int^D dV\right]^{1/3}.$$

The scale c is arbitrary, and can conveniently be placed equal to 1 in many cases, so that

$$\varepsilon_{\omega}^{D} = \left[9\int^{D} \frac{\gamma_S(\theta,\phi)}{\gamma_{III}}\, dS\right]^{1/3} = \left[27\int^{D} dV\right]^{1/3}.$$

Appendix 3.2

In this appendix it is shown that the modified Wulff construction corresponds to a stationary value of the total surface energy at constant volume. The method used is based upon the proof by Laue (1943) of the Wulff construction.

A co-ordinate system for the problem is required, as described below and illustrated in Figure 3.12. Firstly, consider the micro-crystallites as separate bodies, each of them having its own origin. Define now a set of distances, m_i, to denote the normal distances from the relevant origins to each of the external facets not involved in the twin boundaries. Let the surface area of these facets be M_i, with specific surface works γ_i. Next consider those facets which produce the twin boundaries. These must be treated with care to avoid double counting errors. They must occur in matching pairs, and can be divided into two sets. For this, consider n_j and N_j as, respectively, the normal distance to the appropriate origin and the surface area for $\frac{1}{2}$ of these facets, with n'_j and N'_j being the variables (similarly defined) for the complementary facets.

The basic equations can now be written down. The total surface energy of the system, S, can be written

$$S = \sum_i \gamma_i M_i + \sum_j \gamma_t N_j .$$

The total volume, V, can be written

$$V = \tfrac{1}{3}\sum_i m_i M_i + \tfrac{1}{3}\sum_j (n_j N_j + n'_j N'_j).$$

Finally, the Lagrangian to be minimised, L, can be written

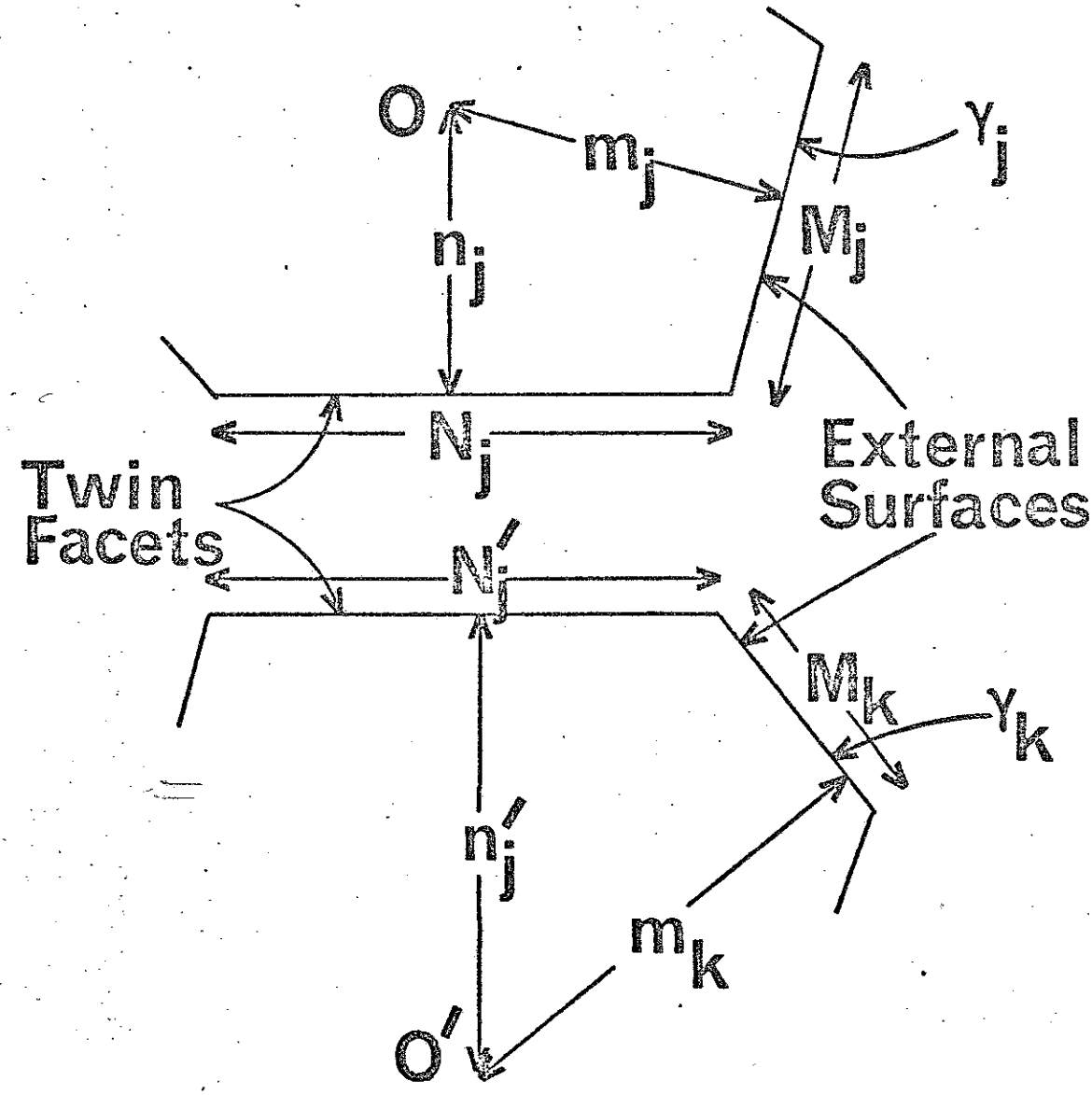

Figure 3.12 The co-ordinate system for analysing the modified Wulff construction, the details of which are explained in the text.

and is subject to the constraints (for all j) that

$$\mathcal{N}_j = \mathcal{N}_j'$$

The Gothic notation is employed to denote the set of points on the planes of area N_j or N_j'.

To obtain a solution, consider differentiating L with a linear combination of the variables

$$p_i = \sum_q a_q m_q + \sum_r b_r n_r + \sum_s c_s n_s'.$$

This search direction is chosen such that the above constraints are all satisfied along it. This gives

$$\frac{\partial L}{\partial p_R} = 0 = \sum_i \gamma_i \frac{\partial M_i}{\partial p_R} + \sum_j \gamma_t \frac{\partial N_j}{\partial p_R} - 2\lambda \frac{\partial V}{\partial p_R}.$$

Noting the relationship (after Laue 1943) that

$$\frac{\partial V}{\partial m_q} = M_q = \frac{1}{2} \sum_i m_i \frac{\partial M_i}{\partial m_q} + \frac{1}{2} \sum_j \left(n_j \frac{\partial N_j}{\partial m_q} + n_j' \frac{\partial N_j'}{\partial m_q} \right)$$

and, furthermore, that $N_j = N_j'$ when the constraints are satisfied

$$\frac{\partial L}{\partial p_R} = 0 = \sum_i (\gamma_i - \lambda m_i) \frac{\partial M_i}{\partial p_R} + \sum_j (\gamma_t - \lambda(n_j + n_j')) \frac{\partial N_j}{\partial p_R}.$$

For a general p_k, a solution to this equation (and the similar equations) is that

$$\frac{\gamma_i}{m_i} = \frac{\gamma_t}{n_j + n_j'} = \lambda \qquad \text{for all } i, j.$$

The values of n_j and n'_j are further constrained by the geometry of the system. Except for a few, peculiar, cases the above conditions are only satisfied simultaneously with the matching pairs constraint if

$$n_j = n'_j.$$

For other possibilities, the different microcrystallites cannot be fitted together. Hence the total surface energy of the precursor MTP is stationary at constant volume if

$$\frac{\gamma_i}{m_i} = \frac{\gamma_k}{2n_j} = \frac{\gamma_k}{2n'_j} = \lambda \qquad \text{for all } i,j.$$

This is the condition for the modified Wulff construction used in 3.4.2.

It should be noted that the above solution is only one of several (for example, some of the precursor segments can vanish). Unfortunately this type of approach (by Lagrangian Variables) is rather unwieldy for investigating the nature of any stationary points - large determinants have to be evaluated. Furthermore, the elastic energy terms in Chapter 4 may be important. The symmetric modified Wulff construction should also be a stationary point for these, and their presence may be important in determining its nature.

CHAPTER 4

ELASTIC ENERGIES AND THE ENERGY BALANCE IN MTPS

4.1 Introduction

The thermodynamic stability of MTPs is an important problem to which no clear answer is as yet available. In particular, there is no completely satisfactory answer as to why Dh should occur. The intention of this chapter is to develop a general model for MTP thermodynamics which includes the effects of typical (and as is shown, very important) experimental variables such as any surface impurities.

The construction of this chapter is a little complicated as a number of different energy terms are considered. The basic approach throughout is the application of inhomogeneous isotropic elasticity theory. This is employed in 4.2 to evaluate the internal strain energies present in MTPs when the individual microcrystallites are strained to eliminate the angular gaps.

In 4.3 the complicated and important effects of elastically distorting the MTP surfaces are analysed. The results from 4.2 and 4.3 are then combined with the results from the modified Wulff construction (3.5) for an evaluation of the energy balance of MTPs and single crystals in 4.4. As the model is relatively general, it is possible to consider the effects of surface impurities, a topic which is discussed in 4.5. Finally, the results obtained and some of the likely consequences of atoms rather than a continuum are discussed in 4.6.

The predominant feature of the results is rather surprising: the thermodynamics of MTPs appear to be very sensitive to the experimental conditions. With favourable conditions the Ics are stable for sizes up to about 20 nm, whilst the Dhs are either metastable

intermediaries or stable in their own right between ~ 20 nm and ~ 60 nm. However, it is possible for MTPs to be unstable regardless of size, and hence not appear.

4.2 Internal Strain Solutions

4.2.1 Introduction

To understand the free energies of MTPs, an estimate of the energy spent in eliminating the angular gaps is required. This can be obtained utilising inhomogeneous isotropic elasticity theory. A solution for the decahedral particles has been previously derived by de Wit (1972), based upon the original equations of Volterra (1907). This is briefly described in 4.2.2, employing a slightly different form avoiding an axial cut-off. In 4.2.3 a new solution for the icosahedral particles is derived.

When describing these solutions the process will be considered in two steps. Initially a purely angular "closure displacement" or a "closure strain" is applied to transform the precursor MTPs into simply connected bodies without any gaps. The second step involves deriving the "equilibrium displacements" required to hold these closure strains in equilibrium.

4.2.2 Decahedral Particles

A suitable closure displacement for these particles is

$$u_\theta = \rho\,\theta\,\Delta\Omega^{Dh}/4\pi \,,$$

corresponding to the closure strain

$$e_{\theta\theta} = \Delta\Omega^{Dh}/4\pi$$

both of which are expressed in cylindrical polar co-ordinates, with the z-axis oriented along the common axis of the five segments. For a three dimensional Dh, no simple solution appears to exist for the equilibrium displacements. However, if plane strain ($e_{zz} = u_z = 0$), and a circular surface are assumed, then an approximate expression for them can be obtained. This takes the form

$$u_\rho = \frac{\mu \Delta\Omega^{Dh}}{4\pi(\lambda+2\mu)} \rho \ln \rho/a - \frac{\Delta\Omega^{Dh}}{8\pi}\rho$$

for a circle of radius a, with boundary conditions of zero pressure on the external surface, and zero displacements at the origin. This yields strains of

$$e_{\rho\rho} = \frac{\mu \Delta\Omega^{Dh}}{4\pi(\lambda+2\mu)} (\ln \rho/a + 1) - \frac{\Delta\Omega^{Dh}}{8\pi} ;$$

$$e_{\theta\theta} = \frac{\mu \Delta\Omega^{Dh}}{4\pi(\lambda+2\mu)} \ln \rho/a + \frac{\Delta\Omega^{Dh}}{8\pi} ;$$

$$e_{\theta\rho} = e_{\rho z} = e_{z\theta} = e_{zz} = 0 ;$$

a cubic dilatation

$$\delta = \frac{\mu \Delta\Omega^{Dh}}{4\pi(\lambda+2\mu)} (2 \ln \rho/a + 1),$$

and a volume independent strain energy W_D^{Dh} given by

$$W_D^{Dh} = 2\mu \left\{ \frac{\lambda \Delta\Omega^{Dh}}{8\pi(\lambda+2\mu)} \right\}^2 .$$

All these strains become infinite on the z-axis.

To avoid this, de Wit (1972) introduced an axial cut-off. However, in very large particles (which de Wit was considering) extensive strain relief is likely through dislocations, whereas in small particles it is unreasonable to consider evaluating the stresses at less than a nearest neighbour distance (from the origin). With this restriction the stresses never become excessive. For example, 0.1 nm from the centre of Dhs 5 nm and 10 nm in radius, the cubic dilatation is only $\sim 2.8\%$ and $\sim 3.5\%$ respectively (in silver). It is therefore reasonable to avoid an axial cut-off.

It should be noted that no further homogeneous strains along the z direction (e_{zz} = constant) are required for the integrated $\hat{zz}$ stress to be zero; this condition is already met ($\int_0^a \rho \delta \, d\rho = 0$). A more complete three-dimensional solution would relieve these unbalanced stresses, probably by some form of extension parallel to the z-axis, and a further radial contraction.

4.2.3 Icosahedral Particles

The problem for an Ic is similar to that of an Dh, albeit more complicated. Full closure can be achieved by incorporating six screw disclinations oriented along the five-fold symmetry axes as mentioned in 2.2. Rather than attempting to solve this complicated general problem, a simpler approximate solution is derived here.

It is possible to consider the average value of the closure strains, ignoring the complicated angular dependence. This corresponds to

$$e_{\theta\theta} = e_{\phi\phi} = \Delta\Omega^{Ic}/8\pi \quad ; \quad e_{\theta\phi} = 0$$

These strains cannot exist in any simply-connected body, as no displacement functions u_θ, u_ϕ exist to produce them, but they represent a good approximation to the true strains.

One further approximation is necessary - that the external surface of the precursor MTP is completely spherical. This is probably a reasonable approximation, as even when employing the strong faceting model (3.5) the deviation from a spherical shape is not particularly large.

The equilibrium strains can now be considerably simplified because of the spherical symmetry. No further angular strains are necessary, only an orientation-independent radial displacement. This can be obtained from the equilibrium equations (see appendix) in the form

$$u_r = \frac{\Delta\Omega^{Ic}\mu r \ln r/a}{6\pi(\lambda+2\mu)} - \frac{r\Delta\Omega^{Ic}}{12\pi}$$

where a is the particle radius. The derivation is given in the appendix. This yields the final strains:

$$e_{rr} = \frac{\Delta\Omega^{Ic}\mu}{6\pi(\lambda+2\mu)}(\ln r/a+1) - \frac{\Delta\Omega^{Ic}}{12\pi} \quad ;$$

$$e_{\phi\phi} = e_{\theta\theta} = \frac{\Delta\Omega^{Ic}\mu}{6\pi(\lambda+2\mu)} \ln r/a + \frac{\Delta\Omega^{Ic}}{24\pi} \quad ;$$

$$e_{r\theta} = e_{\theta\phi} = e_{\phi r} = 0 \quad ;$$

a cubic dilatation of

$$\delta = \frac{\Delta\Omega^{Ic}\mu}{(3\ln r/a+1)},$$

and an elastic strain energy density of

$$\omega_D^{Ic} = \frac{2\mu}{3}\left(\frac{\Delta\Omega^{Ic}}{24\pi}\,\frac{(3\lambda+4\mu)}{(\lambda+2\mu)}\right)^2$$

which is again volume independent.

These stresses become infinite at the origin, suggesting that a central cut-off should be incorporated. However, the region near the origin contributes very little to the total strain energy, so this appears to be an unnecessary refinement. For example, the cubic dilatation 10% out from the centre of a particle is ~10%, but the energy stored within this radius is only ~1% of the total.

Finally, it should be noted that many of the properties normally associated with elastic solutions are not appropriate for the terms described above. The strain terms obtained are not true "trial solutions", but only approximations to the mean values, averaged over the angular co-ordinates. Hence, no displacements u_r, u_θ, u_ϕ exist which can produce these strains; the compatibility equiations for the strains are not obeyed; the cubic dilation is not a solution of Poisson's equation, and the total strain energy is not an upper bound to the true value (i.e. the variation principle cannot be applied). Details of the connection between these properties can be found in many textbooks, e.g. Love (1944).

and an elastic strain energy density of

$$\omega_D^{Ic} = \frac{2\mu}{3}\left(\frac{\Delta\Omega^{Ic}}{24\pi}\frac{(3\lambda+4\mu)}{(\lambda+2\mu)}\right)^2$$

which is again volume independent.

These stresses become infinite at the origin, suggesting that a central cut-off should be incorporated. However, the region near the origin contributes very little to the total strain energy, so this appears to be an unnecessary refinement. For example, the cubic dilatation 10% out from the centre of a particle is ~10%, but the energy stored within this radius is only ~1% of the total.

Finally, it should be noted that many of the properties normally associated with elastic solutions are not appropriate for the terms described above. The strain terms obtained are not true "trial solutions", but only approximations to the mean values, averaged over the angular co-ordinates. Hence, no displacements u_r, u_θ, u_ϕ exist which can produce these strains; the compatibility equiations for the strains are not obeyed; the cubic dilation is not a solution of Poisson's equation, and the total strain energy is not an upper bound to the true value (i.e. the variation principle cannot be applied). Details of the connection between these properties can be found in many textbooks, e.g. Love (1944).

4.3 Surface Strain Energies

4.3.1 Introduction

An important energy term with MTPs is the energy stored in elastically distorting their surfaces, their "surface strain energies". With the highly strained surfaces present in MTPs, this term is important when the particle energies are compared. This section is concerned with a model for this term. In 4.3.2 a precise definition for the strain dependence of the excess surface free energy is provided, permitting a clear separation between the plastic and elastic components. (There is considerable confusion in the literature with the usage of these terms.) This is followed in 4.3.3 by a discussion of the physical background to the two leading strain-dependent terms. Experimental evidence for the "surface stress" tensor (defined in 4.3.2) is briefly reviewed, and criticised, in 4.3.4. Finally, in 4.3.5 a model for the first order surface strain energies in MTPs is described.

4.3.2 Definition of the Strain Dependence of the Excess Surface Free Energy

The excess surface energy per unit area of unstrained surface, γ_e, can be expanded as

$$\gamma_e = \gamma_s + \sum_{ij} g_{ij} e_{ij} + \sum_{ij,kl} a_{ijkl} e_{ij} e_{kl} + \ldots\ldots$$

where γ_s is the specific surface work encountered in Chapter 3, and g_{ij} is the "surface stress tensor". This definition of the

strain dependence, which differs from others available in the literature (e.g. Linford 1972, 1973), has been adopted for three reasons. Firstly, the notation and usage (energy integrals over the unstrained state) are consistent with standard elasticity theory. Secondly, the terms g_{ij} and a_{ijkl} have simple interpretations in an elastic model. Finally, no correlations are made with the liquid surface tension term, which is a bad analogy as strains in a liquid are conceptually different to those in a solid.

4.3.3 Origin of the Strain Dependence

It is useful to consider the physical origin of the two terms g_{ij} and a_{ijkl}. In a bulk solid, an equilibrium exists between the (attractive) electron gas and (net repulsive) atom-atom interactions. However, equilibrium need not exist at the surface retaining the bulk atom positions; atoms are lost and the electron gas rearranges (e.g. Lang and Kohn 1970, 1971). This provides a driving force for atom rearrangements, both perpendicular to, and in, the surface plane, but due to the atoms in the bulk material the latter possibility cannot occur (for an infinite surface).[1] In elastic terms, tractions at the "ends" of the infinite surface sustain stresses throughout the surface layer, conserving the average interatomic spacing. The integral of the stress tensor throughout the surface layer corresponds, exactly, to the surface stress tensor g_{ij}. All the components of g_{ij}

[1] It is possible though to accomodate an expansion in the inter-atomic distances by reconstructing the surface. Hence the common observationsof reconstructed surfaces suggest that g_{ij} is often negative.

correspond to the surface stress term f_{rr} considered by Mays et al (1968), in which the "rr" notation is rather misleading. It should be noted that g_{ij} has components in the surface plan only, as there can be no unbalanced stresses normal to a surface.

The second order term a_{ijkl} arises from the different elastic moduli present in the surface layer. Assuming the surface stress tensor to be zero, the term $\sum_{i,j,k,l} a_{ijkl} e_{ij} e_{kl}$ corresponds to the difference between the energy required to distort the surface layer and a corresponding region of bulk material. As such, it will be considered as part of the limitations of an isotropic elasticity model, and briefly discussed in 4.6.

4.3.4 Magnitude of the Surface Stress Tensor

The values of g_{ij} are not well understood. In principle they can be derived from the lattice contractions in small particles (e.g. Mays et al 1968) or thin platelets (Smart et al 1972), but the results obtained show considerable scatter. This is probably a consequence of trace surface impurities, to which the results should be particularly sensitive (see 4.5). Furthermore, interpretation of results with small particles is complicated by any lattice changes associated with internal defects, surface relaxations or multiple-twinning. For example, modelling the effects of surface relaxations by a thin surface shell of abnormal lattice parameter produces, to first order, an average lattice parameter inversely proportional to the particle radius. This is exactly the same dependence produced by a surface stress.

For the purposes of this chapter the approximation $g_{111} = \tilde{\gamma}_{111}$

of g_{ij} for a (111) face. This assumes that the surface stresses are positive, which need not be true. The "standard" relationship

$$g_{ij} = \gamma_s \delta_{ij} + \partial\gamma_e/\partial e_{ij} \qquad (\delta_{ij} = \text{Kronecker delta})$$

(Shuttleworth 1950, Erikkson 1969) is not true for the strict definition applied in 4.3.2; $\gamma_s \delta_{ij}$ is a plastic term and does not appear. The term $\partial\gamma_e/\partial e_{ij}$ may be genative, as suggested by the common appearance of reconstructed surfaces. The effects of different magnitudes will be considered when the energy balance is evaluated in 4.4.

4.3.5 Numerical Values

A numerical evaluation of the surface strain energy seems to require a number of approximations. Three different effects must be considered: direct interactions with the surface strains in MTPs; alterations to the equilibrium shapes of the particles; and perturbations to the internal strain field. In this section only the first order effects arising from the surface stress tensor g_{ij} are considered.

The last of the three effects can be avoided when particle energies are being compared. With a perfect elastic solution the closed MTPs are internally equilibrated elastic systems without any applied surface tractions or body forces. In terms of elasticity theory, the surface stress tensor corresponds to a set of surface tractions acting on the particles. However, it has been shown by Eshelby (1951, 1956) that there is no interaction energy between

any applied surface tractions and an internally equilibrated body. For this effect MTPs can thus be considered as strain-free single crystals.

This interaction energy in a single crystal is small. For example, with a spherical single crystal and an orientation-independent g_{ij}, the net change in free energy is

$$\Delta G = - \frac{\pi a}{k} \left(\sum_i g_{ii} \right)^2$$

where a is the particle radius, and k the bulk modulus. Therefore, when the free energy of an MTP is compared to a single crystal, only a small change in a small term (from the different faceting) arises. This can be safely ignored.

The direct interaction with the surface strains, and the alterations to the equilibrium shape appear to be intractable. The combined effect of the two terms involves substituting the excess surface free energy γ_e in 4.2 for the specific surface work employed inthe modified Wulff construction (3.4). However, the construction is now invalid; γ_e in general varies across any flat face, whilst a Wulff construction is only applicable for a function dependent solely upon the surface normal. However, the solutions available for the surface strains are only approximate mean values, and no evidence is as yet available for the orientation dependence of the surface stresses. Hence, it is reasonable to attempt only an approximate solution. This will be chosen so that the modified Wulff construction can still be employed. Explicitly, the relationship

$$\sum_{ij} g_{ij} e_{ij} = \frac{g_{111}}{\gamma_{111}} \left(e_{\theta\theta} + e_{\phi\phi} \right) \gamma_s(\theta,\phi)$$

will be assumed, where $e_{\theta\theta}$ and $e_{\phi\phi}$ are the surface strains derived in 4.2. Terms involving strains with components normal to the surface do not arise, as g_{ij} exists only in the surface plane (see 4.3.3).

This term can now be included in the modified Wulff constructions, leading to a new term ε_g given by

$$\varepsilon_g = \frac{1}{g_{111}} \frac{\int \sum_{ij} g_{ij} e_{ij} \, dS}{[\int dV]^{2/3}}$$

$$= \frac{\Delta\Omega^{Ic}}{12\pi} \varepsilon_\omega \approx \varepsilon_\omega/25 \qquad \text{for an Ic, and}$$

$$= \frac{\Delta\Omega^{Ic}}{8\pi} \varepsilon_\omega \approx \varepsilon_\omega/100 \qquad \text{for an Dh,}$$

with the total surface-like energy given by

$$V^{2/3} \left(\varepsilon_\omega \gamma_{111} + \varepsilon_g g_{111} \right)$$

The twin dependent term ε_ω is employed here (rather than ε_s) to include a strain dependence of the twin boundary energies.

These values are inaccurate, as there is little reason to believe that the angular variation of $\sum_{ij} g_{ij} e_{ij}$ matches that for $\gamma_s(\theta,\phi)$, and the true solutions for $e_{\theta\theta}$, $e_{\phi\phi}$ at the surface are unknown. However, they are probably good estimates. The ε_ω values vary by only 10% between the extremes of faceting (3.5). The icosahedral surface strains are good approximations to the average values. The extra strains which relieve the $\hat{z}z$ stress in a Dh probably involve an extension along the z-axis ($e_{zz} < 0$) and a radial contraction ($e_{\theta\theta} > 0$), and these further terms will largely cancel. Hence the values given are probably accurate to about ±20%.

4.4 Energy Balance

It is now possible to analyse the relative energies of the different particles. The total free energy of any particle, G, can be expressed in the form

$$G = (\varepsilon_\omega \gamma_{111} + \varepsilon_g g_{111}) V^{2/3} + W_D V + H(V)$$

where H(V) includes any further terms which are independent of shape or strain (e.g. the cohesive energy). The general behaviour of the total free energy for the three different particle types (single crystals, Dhs and Ics) is shown in Figure 4.1.

The relative energies of any two particle types can be parameterised by a "cross-over diameter", $D_{a,b}$. This is the diameter of a spherical particle with the volume where the total free energies of particle types "a" and "b" are equal. This is given by

$$D_{a,b} = \left(\frac{6}{\pi}\right)^{1/3} \left(\frac{\gamma_{111}}{\Delta\omega_D}\right) \left(\Delta\varepsilon_\omega + \frac{g_{111}}{\gamma_{111}} \Delta\varepsilon_g \right)$$

The total free energy of particle type "a" is smaller than that of "b" for $V < \frac{\pi}{6} D_{a,b}^3$.

Numerical values for these diameters are given in Table 4.1 for the five fcc metals for which data is available. These were evaluated from the surface energy parameters (Table 4.2) and the elastic strain energy densities (Table 4.3). Values for the twin boundary energies and specific surface works are included in Table 4.2, the elastic moduli in Table 4.3.

The expression for the cross-over diameters can be divided into two parts: the ratio of the specific surface work to the

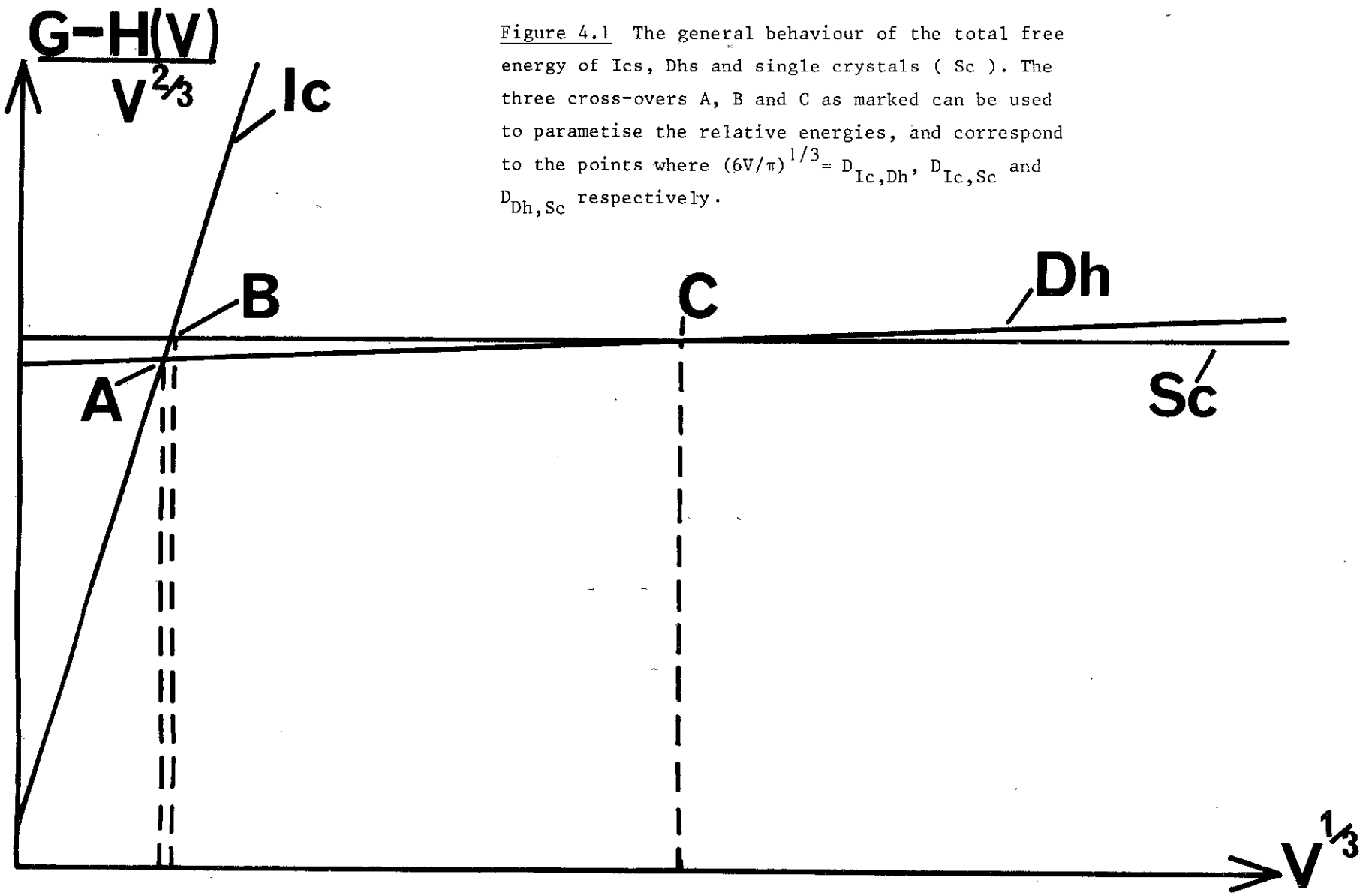

Figure 4.1 The general behaviour of the total free energy of Ics, Dhs and single crystals (Sc). The three cross-overs A, B and C as marked can be used to parametise the relative energies, and correspond to the points where $(6V/\pi)^{1/3} = D_{Ic,Dh}$, $D_{Ic,Sc}$ and $D_{Dh,Sc}$ respectively.

TABLE 4.1

Values for the Cross-over Diameters, which provide estimates of the relevant, experimental particle sizes

		Ag	Al	Au	Cu	Ni
Strong Faceting Model						
$D_{Dh,S}$	(nm)	92.7	-ve	67.4	47.3	-ve
$D_{Ic,S}$	(nm)	18.7	7.6	20.6	15.3	11.3
$D_{Ic,Dh}$	(nm)	18.0	11.8	19.9	14.9	11.8
Zero Faceting Model						
$D_{Dh,S}$	(nm)	-ve	-ve	-ve	-ve	-ve
$D_{Ic,S}$	(nm)	-ve	-ve	-ve	-ve	-ve
$D_{Ic,Dh}$	(nm)	0.5	-ve	0.5	0.0	-ve

TABLE 4.2

Surface Energy Parameters. The specific surface works (γ_{111}) have been extrapolated from the values give by Linford (1973) to 300° C employing a surface entropy of 1.2 $mJm^{-2}K^{-1}$ (Chadwick and Kirchner 1970). Twin boundary energies (γ_t) are half the Stacking fault energies given by Coulomb (1978).

	Ag	Al	Au	Cu	Ni
$\gamma_{111}(Jm^{-2})$	1.90	0.996	2.26	2.51	2.96
$\gamma_t(mJm^{-2})$	10.0	62.5	17.5	22.5	62.5
$\gamma_t/2\gamma_{111}(\%)$	0.264	3.14	0.388	0.488	1.05
$\varepsilon_\omega+\varepsilon_g$ - Strong Faceting Model					
Single Crystal	5.50	5.50	5.50	5.50	5.50
Dh	5.48	5.65	5.48	5.49	5.52
Ic	5.09	5.23	5.09	5.10	5.13
$\varepsilon_\omega+\varepsilon_g$ - Zero Faceting Model					
Single Crystal	4.84	4.84	4.84	4.84	4.84
Dh	4.87	5.05	4.88	4.88	4.92
Ic	4.85	5.25	4.87	4.88	4.96

TABLE 4.3

Elastic Moduli and the Elastic Strain Energy Densities in NTPs. Values for the elastic moduli were taken from the International Table of Standards (1978).

	Ag	Al	Au	Cu	Ni
(GPa)	83.6	58.1	198.0	123.0	126.0
(GPa)	30.3	26.1	27.0	48.3	76.0
W_D^{Dh} (10^6 Pa)	0.509	0.362	0.833	0.658	0.782
W_D^{Ic} (10^6 Pa)	51.8	44.4	55.9	81.9	122.0

strain energy density difference ($\gamma_{111}/\Delta W_D$), and a "balance" term ($\Delta\varepsilon_\omega + \frac{g_{111}}{\gamma_{111}}\Delta\varepsilon_g$) containing the effects of faceting, twin boundaries and surface stresses. The first part is relatively insensitive to the metal involved, values of $3.36(\pm0.5)\,\mu$ and $0.0315(\pm0.009)\,\mu$ being good approximations for comparing Dhs and Ics respectively to single crystals. These values are probably too large, the strain energy densities in both cases probably being overestimates (certainly so by the Variational Principle for the Dhs). However, both appear to be significant improvements upon Ino's (1969) results, being approximately 95% (Dh), and 65% (Ic) smaller. The specific surface works are probably relatively accurate (±25%), the major uncertainty being the surface entropy. More importantly, very large reductions are likely when adsorbed species are present (see 4.5).

The ratio term never affects the most important result, the signs of the cross-over diameters, only their magnitudes. The signs are determined by the balance term, which is sensitive to the degree of faceting, the twin boundary energy and the surface stresses. All three terms are of similar magnitude, as shown in Table 4.4 (for silver and aluminium) so that small variations have large effects. This can be seen for the twin boundary energies by comparing the silver and aluminium values, and for the faceting by comparing the strong and zero faceting models (Tables 4.2 and 4.4). The linear variation with the surface stress magnitude g_{111} has not been explicitly calculated, but can be deduced from the sub-totals in Table 4.4. It should be noted that these indicate positive cross-over diameters for silver if $g_{111} = 0$, even for the zero-faceting model. This feature is shared by all the metals except aluminium.

TABLE 4.4

Relative Contributions of the Three Effects for Silver and Aluminium: the faceting ($\Delta\varepsilon_\omega$), the twin boundaries ($\Delta\varepsilon_\omega - \Delta\varepsilon_s$), and the surface stresses ($\Delta\varepsilon_g$). Values are shown relative to single crystals with the same faceting, with the signs shown identical to those in the cross-over diameters, i.e. positive is favourable to MTP formation. The sub-totals illustrate the effect of neglecting the surface strain energies .

	Decahedral MTPs Faceting		Icosahedral MTPs Faceting	
	Strong	Zero	Strong	Zero
SILVER:				
$\Delta\varepsilon_s$	0.092	0.033	0.609	0.206
$\Delta\varepsilon_\omega - \Delta\varepsilon_s$	-0.016	-0.016	-0.001	-0.035
Subtotals, appropriate for considering $g_{111} = 0$	0.076	0.017	0.608	0.171
$\Delta\varepsilon_g$	-0.054	-0.048	-0.194	-0.186
Total for $g_{111} = \gamma_{111}$	0.022	-0.031	0.404	-0.015
ALUMINIUM:				
$\Delta\varepsilon_s$	0.092	0.033	0.609	0.206
$\Delta\varepsilon_\omega - \Delta\varepsilon_s$	-0.187	-0.192	-0.140	-0.414
Subtotals, appropriate for considering $g_{111} = 0$	-0.095	-0.159	0.469	-0.208
$\Delta\varepsilon_g$	-0.054	-0.050	-0.202	-0.202
Total for $g_{111} = \gamma_{111}$	-0.149	-0.209	0.268	-0.410

Clearly the results are sensitive to the model adopted, and should be interpreted only as indicating the conditions favourable to MTP formation: extensive faceting, particularly any which favours the appropriate angular regions (3.4); small values of the twin boundary to specific surface work ratio; and small to negative values of the surface stress tensor.

One important new result is the position of the Dhs, particularly in the strong faceting model. In the previous continuum analysis by Ino (1969), these particles were always unstable compared to single crystals ($D_{Dh,S} < 0$), but metastable compared to tetrahedra. As a consequence of the improved treatment for the surfaces of these particles (3.4), they now appear intermediary between Ics and single crystals, possibly being the most stable type in a narrow size regime.

Another important aspect is that the cross-over diameters can take negative values, i.e. in certain conditions MTPs will be unstable at all sizes. In all previous theories, Ics were predicted to be the most stable form at very small sizes, which is inconsistent with their absence in certain experiment systems.

4.5 Adsorption

An important application of the energetic formulation presented is in understanding the effect of gas adsorption (or absorption). This is probably the most important variable determining the type of particles produced.

The free energy of adsorption, $\Delta\varsigma^{ads}$, can be expanded in the form:

$$\Delta\varsigma^{ads}(\theta,\phi) = \gamma_S^{ads}(\theta,\phi) + \sum_{ij} g_{ij}^{ads} e_{ij} + \ldots\ldots$$

and its effects included by adding the two terms to the corresponding clean metal parameters.

The "specific adsorption work", $\gamma_s^{ads}(\theta,\phi)$, is negative and normally quite large. Its major effect appears to be a promotion of faceting (see for example Blakeley and Somorjai 1977 and Flytzani-Stephanopoulos et al 1977) possibly by a nearly isotropic reduction in the effective $\gamma_s(\theta,\phi)$ (Rhead and McLean 1964). The influence on MTP stability will be mixed; cross-over diameters will drop with the reduction in the effective specific surface work, and the increase in the effective twin component will rise through the increased faceting.

The "adsorption surface stress tensor", g_{ij}^{ads}, does not seem to have appeared in the literature to date. Its sign and magnitude probably depend upon the adsorption species. For example, a monolayer of nickel on silver in layer register probably has $g_{ij}^{ads} > 0$, the nickel lattice parameter being considerably smaller. Conversely a monolayer of silver on nickel probably has $g_{ij}^{ads} < 0$. Strong promotion of MTP formation obviously occurs for negative values.

Clearly, quite large gas dependence can be expected in the most stable forms, and hence the observed structures. This is consistent with the considerable variations in particle epitaxy and morphology that can occur when the experimental conditions are altered. Some preliminary experiments have provided a partial confirmation for this prediction. When samples of gold on either NaCl or amorphous alumina were annealed at 500° C for 30 minutes in either air at atmospheric pressure, 400 Pa of argon, or a vacuum of $< 3 \times 10^{-3}$ Pa, large numbers of MTPs were observed in the 0- 20 nm

in 400 Pa of hydrogen for the same period, almost exclusively single crystals were observed for sizes ~5 nm. However, further work on these lines seems required; the structure variations were reproducible, but the epitaxy on the NaCl substrate was not.

4.6 Discussion

The precise thermodynamics of small particles are still unclear, although a number of the general trends are now apparent. The formation of MTPs is favoured by extensive faceting, small twin boundary energies and small or negative surface stresses. If sufficient of these conditions are met, Ics will be the most stable particles at very small sizes, with Dhs either metastable intermediaries or stable in their own right within a narrow size regime. For other experimental conditions, MTPs may be thermodynamically unstable at all sizes, and not appear. The presence of any surface impurities should be particularly important in determining whether MTPs occur, a prediction partially substantiated by some preliminary results.

The extreme sensitivity of the particle stabilities and faceting to impurities should be important in catalysis. Many simple models for the action of various promoters or poisons employ a blocked site model; trace elements chemisorb preferentially onto certain active sites, preventing them from participating in any reactions.. A further indirect mechanism can now be proposed: modification of the relative concentrations of the active sites through a change in the faceting or particle type. This model is amenable to direct experimental test by high resolution analysis of, for example, active and poisoned catalysts, work which should

be of considerable interest.

However, when analysing any experimental distribution of particles, it should be remembered that the thermodynamic criteria may not be the controlling effects. There is a second, trivial solution where the particle energies are equal - at zero volume. Therefore at the earliest stages of particle growth (e.g. < 100 atoms) a Boltzmann distribution of particle types is likely, equilibrated by the vibrational transformations mentioned in 2.4. With further growth, these particle transformations will become inhibited, so that the observed particles may represent the effects of particle coalescence superimposed upon an earlier "frozen" distribution.

With atoms rather than a continuum, other energy terms may be important. As mentioned in 3.7, the specific surface work is size dependent, a feature probably shared by the surface stresses. The elastic moduli are also size and position dependent. This latter effect corresponds to the second order surface stress term $a_{ijkl}e_{ij}e_{kl}$, and is probably negative (i.e. favourable to MTPs); loss of atoms should soften the retaining forces.

An interesting effect, analogous to the surface stresses, may occur near the five-fold axes. The atomic co-ordination in this region is different to that in an fcc material; for example, atoms on the axis have only five second nearest neighbours, all normal to the axis. This produces a zero-point double stress tensor, which might counteract the large stresses arising near these axes in the elastic solutions.

More accurate calculations of the particle energies employing, for example, pseudo-potentials would clearly be of considerable

interest. However, these will need to faithfully represent the specific surface work; the surface stresses; the internal elasticity; any inhomogeneous relaxations, and be fully minimised with respect to the surface shape - a task of considerable complexity. Alternatively, useful qualitative results might be obtained with inhomogeneous relaxations and the modified Wulff construction, employing, for example, a Mie Potential.

Another approach might be through an improved understanding of the surface stresses and the adsorption surface stresses. The latter quantity may be amenable to experimental measurement by the incorporation of a strain stage into standard UHV equipment with flash desorption capabilities. Measurements of the clean metal surface stresses appears, in contrast, to require an experimental innovation.

In conclusion, the thermodynamics of MTPs are controlled by the experimental conditions employed. When they do occur, the Ics can be stable up to sizes of about 20 nm, with the Dhs either metastable intermediaries or stable in their own right for sizes between 20 nm and 60 nm. However, in some cases (such as for gold particles in a hydrogen atmosphere) they may never be stable.

Appendix 4.1

In spherical polar co-ordinates, the displacements u_θ, u_ϕ, u_r are related to the strains by:

$$e_{rr} = \frac{\partial u_r}{\partial r} \quad ; \quad e_{\theta\theta} = \frac{1}{r}\frac{\partial u_\theta}{\partial \theta} + \frac{u_r}{r} \; ;$$

$$e_{\phi\phi} = \frac{1}{r\sin\theta}\frac{\partial u_\phi}{\partial \phi} + \frac{u_\theta}{r}\cot\theta + \frac{u_r}{r} \; ;$$

$$2e_{r\theta} = r\frac{\partial}{\partial r}\left(\frac{u_\theta}{r}\right) + \frac{1}{r}\frac{\partial u_r}{\partial \theta} \; ; \quad 2e_{r\phi} = \frac{1}{r\sin\theta}\frac{\partial u_r}{\partial \phi} + r\frac{\partial}{\partial r}\left(\frac{u_\phi}{r}\right),$$

and $$2e_{\theta\phi} = \frac{\sin\theta}{r}\frac{\partial}{\partial \theta}\left(\frac{u_\theta}{\sin\theta}\right) + \frac{1}{r\sin\theta}\frac{\partial u_\theta}{\partial \phi},$$

the cubic dilatation is given by

$$\delta = e_{rr} + e_{\theta\theta} + e_{\phi\phi},$$

the strain energy in any element of volume is given by

$$W_D = \frac{1}{2}(\lambda + 2\mu)\delta^2 + 2\mu\left(e^2_{\theta\phi} + e^2_{\phi r} + e^2_{r\theta} - e_{\theta\theta}e_{\phi\phi} - e_{rr}e_{\theta\theta}\right),$$

and the equilibrium equations for the stresses are.

$$\frac{\partial \hat{r}\hat{r}}{\partial r} + \frac{1}{r}\frac{\partial \hat{r}\hat{\theta}}{\partial \theta} + \frac{1}{r\sin\theta}\frac{\partial \hat{r}\hat{\phi}}{\partial \phi} + \frac{1}{r}\left(2\hat{r}\hat{r} - \hat{\theta}\hat{\theta} - \hat{\phi}\hat{\phi} + \hat{r}\hat{\theta}\cot\theta\right) = 0 \; ;$$

$$\frac{\partial \hat{r}\hat{\theta}}{\partial r} + \frac{1}{r}\frac{\partial \hat{\theta}\hat{\theta}}{\partial \theta} + \frac{1}{r\sin\theta}\frac{\partial \hat{\theta}\hat{\phi}}{\partial \phi} + \frac{1}{r}\left(\left[\hat{\theta}\hat{\theta} - \hat{\phi}\hat{\phi}\right]\cot\theta + 3\hat{r}\hat{\theta}\right) = 0,$$

and $$\frac{\partial \hat{r}\hat{\phi}}{\partial r} + \frac{1}{r}\frac{\partial \hat{\theta}\hat{\phi}}{\partial \theta} + \frac{1}{r\sin\theta}\frac{\partial \hat{\phi}\hat{\phi}}{\partial \phi} + \frac{1}{r}\left(3\hat{r}\hat{\phi} + 2\hat{\theta}\hat{\phi}\cot\theta\right) = 0$$

With the closure strains

$$e_{\theta\theta} = e_{\phi\phi} = \frac{\Delta\Omega^{Ic}}{8\pi}, \quad e_{\theta\phi} = 0$$

added to an unknown radial displacement u_r, the strains are

$$e_{rr} = \frac{\partial u_r}{\partial r} ; \qquad e_{\theta\theta} = e_{\phi\phi} = \frac{\Delta\Omega^{Ic}}{8\pi} + \frac{u_r}{r} ;$$

$$e_{\theta\phi} = e_{\phi r} = e_{r\theta} = 0 , \text{ and}$$

$$\delta = \frac{1}{r^2}\frac{\partial}{\partial r}(r^2 u_r) + \frac{\Delta\Omega^{Ic}}{4\pi} .$$

Hence, the equilibrium equations above are satisfied if

$$(\lambda+2\mu)\frac{\partial}{\partial r}\left\{\frac{1}{r^2}\frac{\partial}{\partial r}(r^2 u_r)\right\} = \frac{\Delta\Omega^{Ic}\mu}{2\pi r}$$

i.e.

$$u_r = \frac{\Delta\Omega^{Ic}\mu r \ln r}{6\pi(\lambda+2\mu)} + Ar + B/r^2$$

where A and B are constants of integration.

Considering now the two boundary conditions:

$$\lim_{r\to 0} u_r = 0 \quad \text{and} \quad \hat{rr} = 0 \quad \text{at } r = a$$

where a is the particle radius, then

$$B = 0 \qquad \text{and}$$

$$A = -\frac{\Delta\Omega^{Ic}\mu \ln a}{6\pi(\lambda+2\mu)} - \frac{\Delta\Omega^{Ic}}{12\pi} .$$

CHAPTER 5

HIGH RESOLUTION STUDIES OF MTPs

5.1 Introduction

The most straightforward, and potentiallv the most powerful, method for examining small particles (ca 20 nm or less) is lattice imaging in a high resolution electron microscope. In addition to observing any internal defects, an effective micro-diffraction pattern is obtained with high spatial resolution. Three major problems arise: firstly, the image is not a complete representation of the object as the microscope does not faithfully transfer the contrast and position of all the lattice information; secondly, it is difficult to ensure that any strains are suitably projected so as to be visible and readily interpretable in the image, and finally, severe anomalies can occur through thickness variations and strains (Hashimoto et al 1961) particularly with dislocations (Cockayne et al 1971).

There are considerable advantages in employing higher accelerating voltages for obtaining lattice images. Relative to 100kV, diffraction angles at 500kV, for example, are reduced by a factor of ~2.6, thereby substantially reducing the effects of spherical aberration. Furthermore, values of the excitation parameters drop, and these reduce the effects of thickness variations or strains. However, these gains are offset by the increased many-beam nature of the diffraction, which complicates any image interpretation.

This chapter is concerned with results obtained using the Cambridge University 600kV H.R.E.M. (Cosslett et al 1979) on the internal structure of small gold and silver MTPs. These demonstrate the presence of very fine variations in the lattice fringes and some possible partial dislocations. However, the ready production of artifacts in lattice images of small particles makes the interpretation of these features ambiguous.

5.2 Interpretation of Lattice Fringes

To interpret lattice fringes requires an, a priori, understanding of how they are produced and how artifacts may occur. That is the subject of this section. The basic theory is well established, being described in many textbooks (e.g. Hirsh et al 1965), but its detailed application to small particles composed of many overlapping microcrystallites has not appeared in the literature.

5.2.1 Theory of Lattice Fringe Formation

To a first approximation, lattice fringes can be derived from the standard two beam dynamical approximation. The total exit wave from crystal can be written (after Hirsh et al 1965)

$$\Psi = \phi_0 e^{2\pi i \underset{\sim}{k}_0 \cdot \underset{\sim}{r}} + \phi_g e^{2\pi i \underset{\sim}{k}_g \cdot \underset{\sim}{r}}$$

where $\phi_g = \sin^2(\beta/2) e^{2\pi i \gamma_1 t} + \cos^2(\beta/2) e^{2\pi i \gamma_2 t}$;

$\phi_0 = \frac{1}{2} \sin\beta \left(e^{2\pi i \gamma_2 t} - e^{2\pi i \gamma_1 t} \right)$;

$\gamma_1 = s + \left(s^2 + 1/\xi_g^2 \right)^{1/2}$;

$\gamma_2 = s - \left(s^2 + 1/\xi_g^2 \right)^{1/2}$, and

$\cot\beta = s \xi_g$

s being the excitation parameter, t the thickness and ξ_g the extinction distance.

The image intensity (for a perfect microscope) can then be written

$$I \propto \Psi\Psi^* = |\phi_0|^2 + |\phi_g|^2 + |\phi_0||\phi_g| \cos(2\pi \underset{\sim}{g}.\underset{\sim}{r} - \alpha)$$

where

$$\alpha = \mathrm{Tan}^{-1}\{\cos\beta \tan(\pi t(\gamma_1-\gamma_2)\} \quad \text{Sin}[\pi t(\gamma_1-\gamma_2)]>0$$
$$\text{"} \qquad -\pi \qquad \text{Sin}[\pi t(\gamma_1-\gamma_2)]<0$$

$\underset{\sim}{g}$ being the reciprocal lattice vector. The cosine term corresponds to the lattice fringes, superimposed upon an essentially uniform background.

5.2.2 Effects of the Dynamical Phase Shift

The dynamical phase shift is the source of many problems. It alters with variations in either the crystal thickness or orientation, and can thus lead to artifacts. In small polycrystals with steeply sloping sides, thickness variations are always present and are analysed here in detail, extending the original work by Hashimoto et al (1961).

The shape of any individual microcrystallite can be approximated to a wedge, with the thickness variation specified by a "thickness" vector", $\underline{m}$, defined by

$$\underset{\sim}{\nabla} t = \underline{m}$$

so that $t = \underline{m} \cdot (\underset{\sim}{\rho} - \underline{c})$, where $\underset{\sim}{\rho}$ is the position vector in the object plane and $\underline{c}$ a constant vector. This thickness vector has a direct experimental significance in the diffraction pattern. Substituting

Figure 5.1 Plot of the shift coefficient A as a function of the crystal thickness (assuming that $A = d\alpha/dt$). The curves for four different values of the ratio $\varepsilon_g^{eff}/\varepsilon_g$ are shown, with the relevant values shown on the right-hand side.

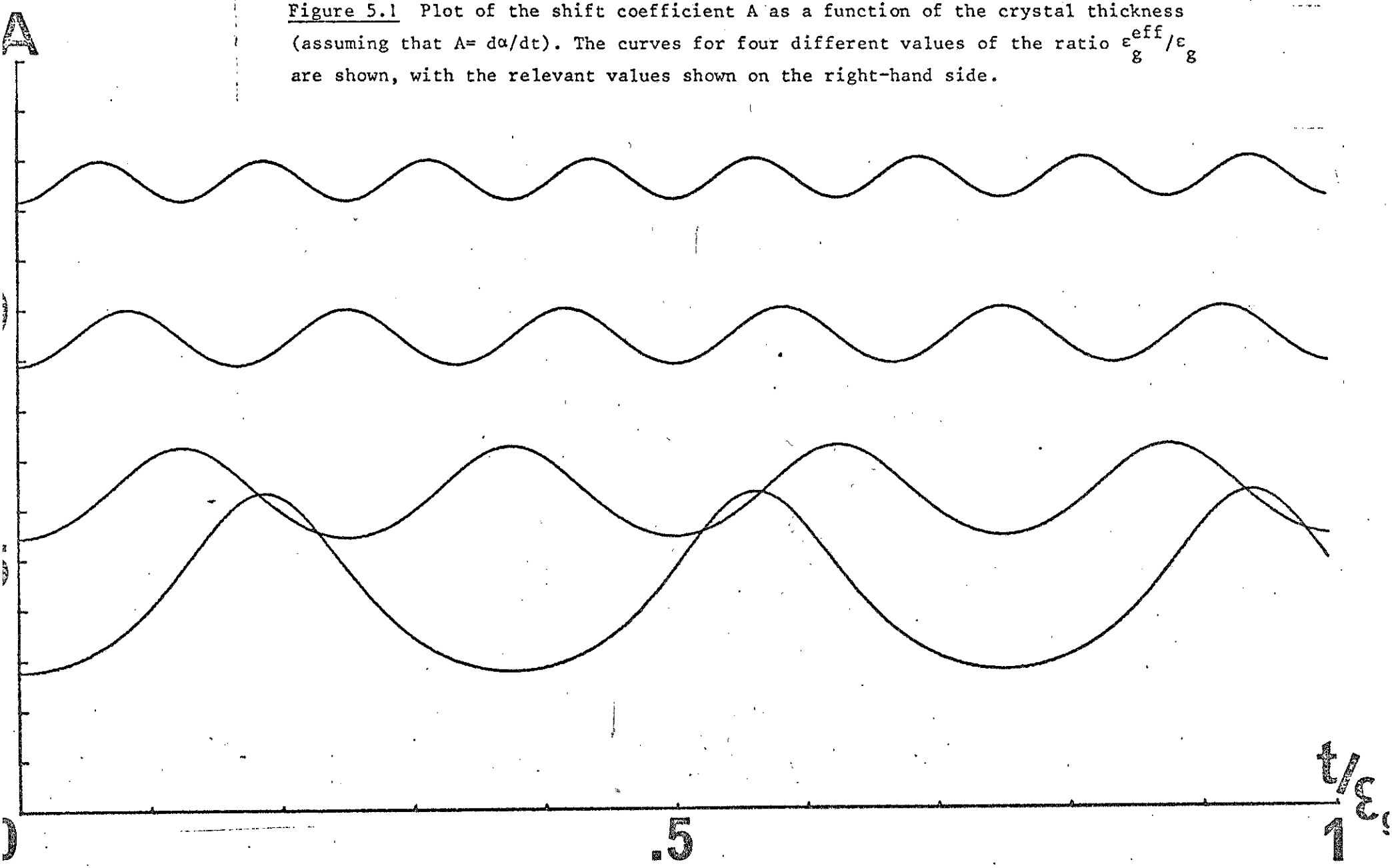

diffraction pattern. This contains four spots (rather than two) at $\underline{m}\gamma_1$, $\underline{m}\gamma_2$, $\underline{g} + \underline{m}\gamma_1$, $\underline{g} + \underline{m}\gamma_2$. This splitting has been observed for MgO smoke crystals by Cowley and Rees (1946, 1947) and Honjo (1947), with a multiplicity of spots in the more general n beam dynamical case (Moliere and Wagenfeld 1958 and Lehmpfuhl and Reissland 1968). Furthermore, interference between these beams produces the various fringe patterns: the two "undiffracted beams" ($\underline{m}\gamma_1$ and $\underline{m}\gamma_2$) the bright field thickness fringes; the two "diffracted beams" ($\underline{g} + \underline{m}\gamma_1$, $\underline{g} + \underline{m}\gamma_2$) the dark field thickness fringes, and all four together, the lattice fringes.

The effect of on the fringe pattern can be expressed by two terms: a shift of the lattice reciprocal vector to the new value $\underline{g} + \underline{Am}$, and the inclusion of steps of π at the minima of either $|\phi_0|$ or $|\phi_g|$. The shift coefficient, A, is nearly constant with thickness, particularly so for a large excitation parameter where it takes the value $2\pi (S^2 + 1/\xi_g^2)^{1/2}$ (i.e. $2\pi / \xi_g^{eff}$, where ξ_g^{eff} is the effective extinction distance). Values for the variation of A with thickness are plotted in Figure 5.1 for various excitation parameters. It should be noted that (in the two beam theory) this term arises solely from the interference of the 2 undiffracted beams ($\underline{m}\gamma_1$, $\underline{m}\gamma_2$). With n beam diffraction, a similar term is likely, "carried" by the diffracted beams (i.e., formed by the mutual interference of the split diffracted beams).

Hence the fringes produced, even with a perfect microscope, need not faithfully represent the spacing or orientation of the atomic planes. With $|m|$ typically in the range $\sqrt{2} - 2\sqrt{2}$, alterations of a few degrees in orientation and a few per cent in spacing are possible. Only at an exact Bragg orientation (where A = 0) or (by symmetry) at an exact three beam condition is a true image of the lattice planes

produced. Furthermore, the artificial steps of $\frac{1}{2}$ a lattice fringe occurring at the minima of either $|\phi_0|$ or $|\phi_g|$ might, for example, be confused with stacking faults.

Further effects also occur with overlapping microcrystallites. The phase shifts are magnified for Moire fringes, and are transmitted between wedges. To illustrate the latter effect, it is convenient to consider two overlapping wedges, exactly Bragg oriented for two beam diffraction, with their diffraction vectors parallel but unequal in magnitude (as shown in Figure 5.2). Passage through the first wedge, produces two undiffracted and two diffracted beams with no net fringe shifts ($A = 0$). The undiffracted beams now travel through the second wedge, producing four new diffracted beams and four undiffracted beams. To a first approximation, no fringe shifts will accumulate for this second set of fringes, as the deviations from a Bragg orientation of the two main beams are very small. However, the diffracted beams from the first microcrystallite are themselves diffracted, this double diffraction occurring well away from a Bragg orientation. Hence these beams accumulate a considerable fringe shift which is dependent upon the thickness of the second wedge. Thus, lattice fringes can be disrupted by the thickness of other microcrystallites, even when the latter produce no fringes themselves.

5.2.3 Effects of the Spherical Aberration

The second source of anomalies is the spherical aberration. Any wave travelling at an angle θ to the optic axis undergoes a phase shift χ where

$$\chi = \frac{\pi}{\lambda}\left(\Delta z\,\theta^2 + \frac{1}{2} C_s \theta^4\right)$$

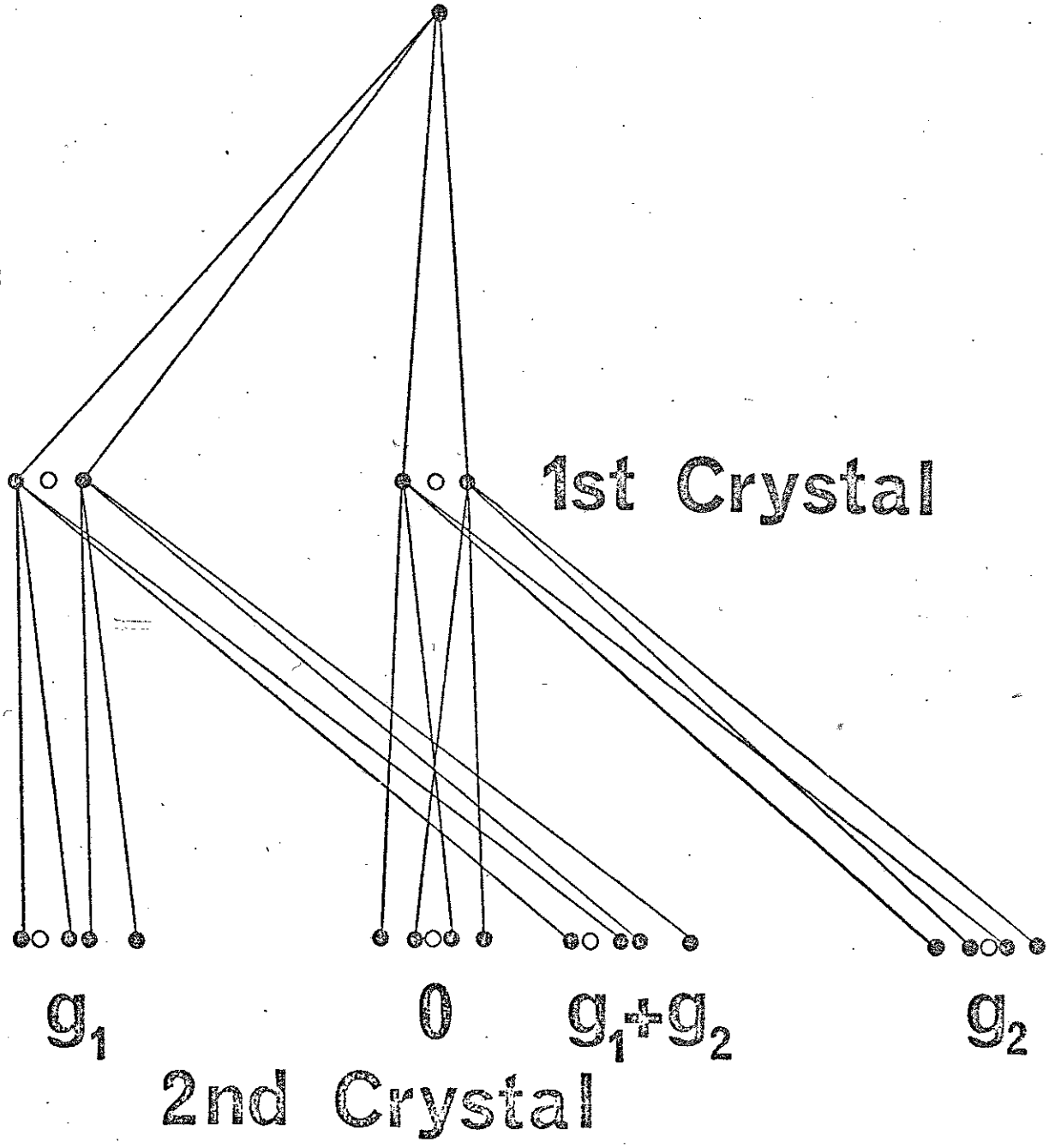

Figure 5.2 Illustration of the transmission of the phase shifts with overlapping microcrystallites. Shown in the figure are the diffraction patterns after the 1st and 2nd crystals with ● for the positions of the diffraction spots and ○ for the relevant diffraction vectors (i.e. the spots present in the absence of the wedge splitting). As explained in the text, double diffraction from the g_1 spot introduces a phase shift which depends upon the thickness of the second crystal.

and is displaced away from its point of origin relative to the optic axis by a vector $\underset{\sim}{\delta}$, where

$$\underset{\sim}{\delta} = \frac{\lambda}{2\pi} \underset{\sim}{\nabla} \chi = \underset{\sim}{\theta} \left(\Delta z + C_s \theta^2 \right).$$

The effect of the phase shift χ is normally discussed by the Contrast Transfer Function, $\sin \chi$. This describes how (i.e. with what amplitudes) the spatial frequencies at the exit surface of a crystal are transferred, by the microscope, to the image. (See, for example, Cowley 1975). However, this approach is not particularly suitable for strong phase objects, such as lattice fringes, especially as it ignores the important effects of the translation $\underset{\sim}{\delta}$.

For lattice fringes the most appropriate condition to consider is positioning the diffracted beams so that they interfere in the image plane with the undiffracted beam arising from the same position in the object, that is $\underset{\sim}{\delta} = \underset{\sim}{0}$. This automatically corresponds to a stationary value (with respect to θ) for χ. Hence no anomalies occur from any small changes in the diffraction vector through the phase shift term. Provided that no attempt is made to allocate the lattice fringes exactly to the lattice planes ($\alpha \neq 0$), this condition appears to allow small variations to be directly resolved.

Unfortunately this is not true, for a reason that has not received as much attention in the literature as it deserves. When $\underset{\sim}{\delta} = 0$, $d|\delta|/d\theta = 2C_s\theta^2$ which is not zero. Therefore any small change of n% in the lattice spacing is accompanied by a relatively large translation (in units of the fringe spacing), given by

$$\Delta|\delta| \frac{\theta}{\lambda} = \frac{2C_s\theta^4 n}{\lambda} \%.$$

For example, with the silver (111) lattice fringes (.235 nm) this change

is 32n% with a Siemens 102 (C_s = 2mm, 100kV), 4n% with the microscope employed here (C_s = 3mm, 500 kV). Hence any small changes present at the crystal exit surface are amplified and distorted by the microscope.

It should be noted that the above comments are only strictly true for two beam lattice fringes. In general, for n beam diffraction, 2n diffracted and n undiffracted beams should be considered (3 beam fringes, with superimposed the wedge splitting discussed in 5.2). Hence, more complicated behaviour is likely, including some loss of contrast. For example, with symmetric three beam fringes, $\frac{1}{4}$ fringe spacing translations of the diffracted beams will produce destructive interference, with no observed lattice fringes.

5.2.4 Summary

To summarise: severe anomalies are to be expected in lattice images of small particles. In general the observed lattice fringes do not have the same orientation or spacing as the actual lattice planes in the object. Any small variations in the object lattice or thickness produce artifacts at the crystal exit surface which are themselves further amplified and distorted by the image translations. As is shown in the following sections, the microscope that was employed provides images of sufficient clarity for these very small changes to be readily detected.

5.3 Experimental Details

Gold and silver were evaporated onto NaCl and KCl, respectively, at 300° C in a vacuum of ~3 x 10^{-3} pascals, the substrates having been previously cleaned in-situ. The samples were then allowed to cool to room temperature in the vacuum (taking ~ 45 minutes), were coated by evaporation with a thin amorphous carbon film and mounted, via flotation on distilled water, on microscope grids. These samples were examined using axial illumination lattice imaging at accelerating voltages of 500 and 575 kV, principally the former, with the Cambridge HREM. An objective aperture was often used which included the (220) beams (.144 nm), although its absence did not materially affect the images obtained. Typical operating conditions were with image magnifications of 300,000 to 400,000 times, considerably defocussed illumination (to provide adequate illumination coherence), and exposure times of $4\frac{1}{2}$ or $7\frac{1}{2}$ seconds. Any residual image astigmatism was normally corrected at magnifications in excess of 600,000 times, using the granularity in the carbon support film.

5.4 Results

The general appearance of the samples is shown in Figures 5.3 and 5.4.

5.4.1 Decahedral MTPs

These particles were found with either <100> or <111> epitaxies. With the <100> orientation an involved and characteristic lattice pattern was observed, as shown in Figure 5.5. The very

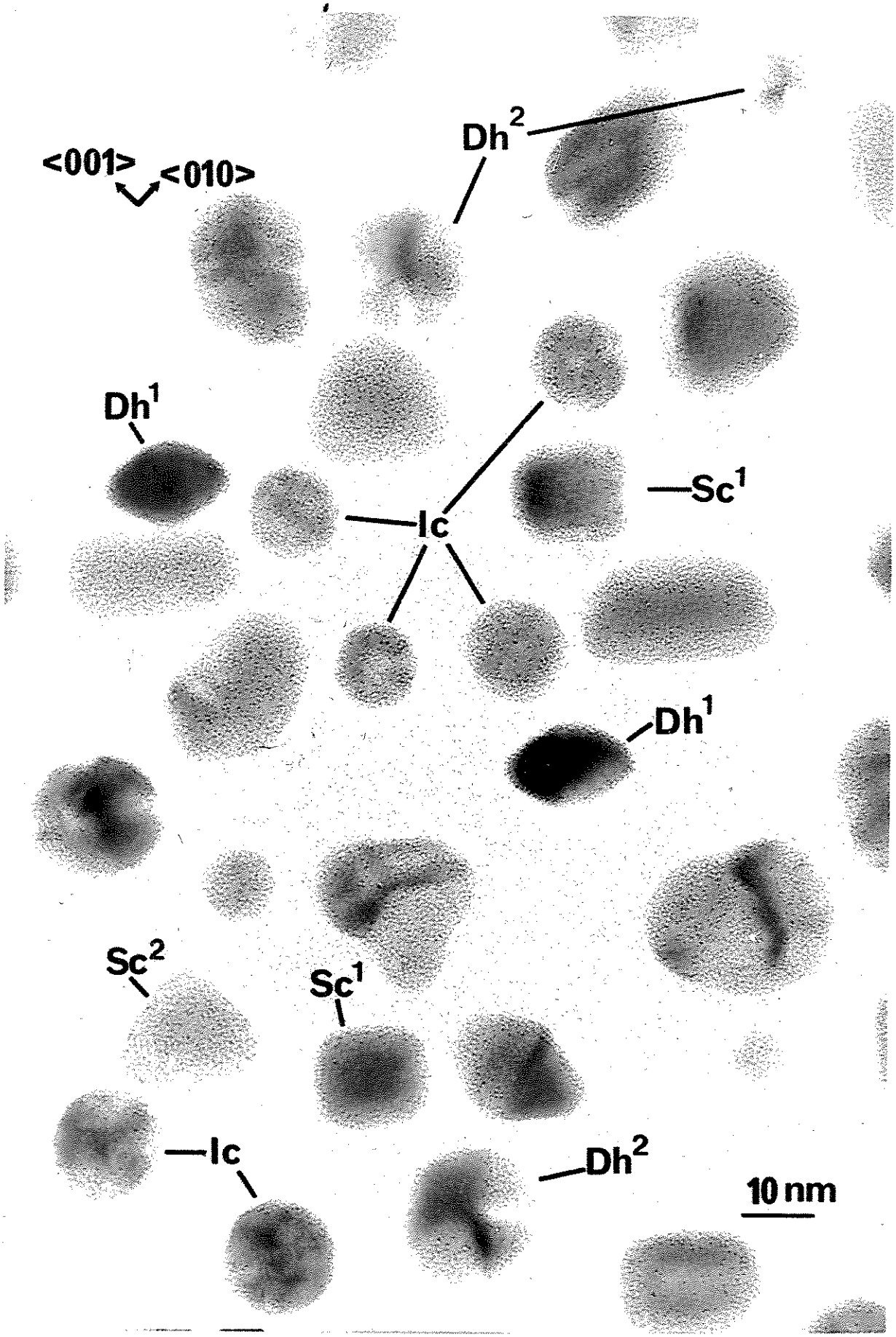

Figure 5.3 A typical region of the Ag sample. The different particle types indicated are: Icosahedral MTPs (Ic_1) ; Decahedral MTPs with <100> and <111> epitaxies (Dh_1 and Dh^2 respectively), and single crystals with <100> (Sc^1) and <111> (Sc^2) epitaxies. The orientation of the sustrate is

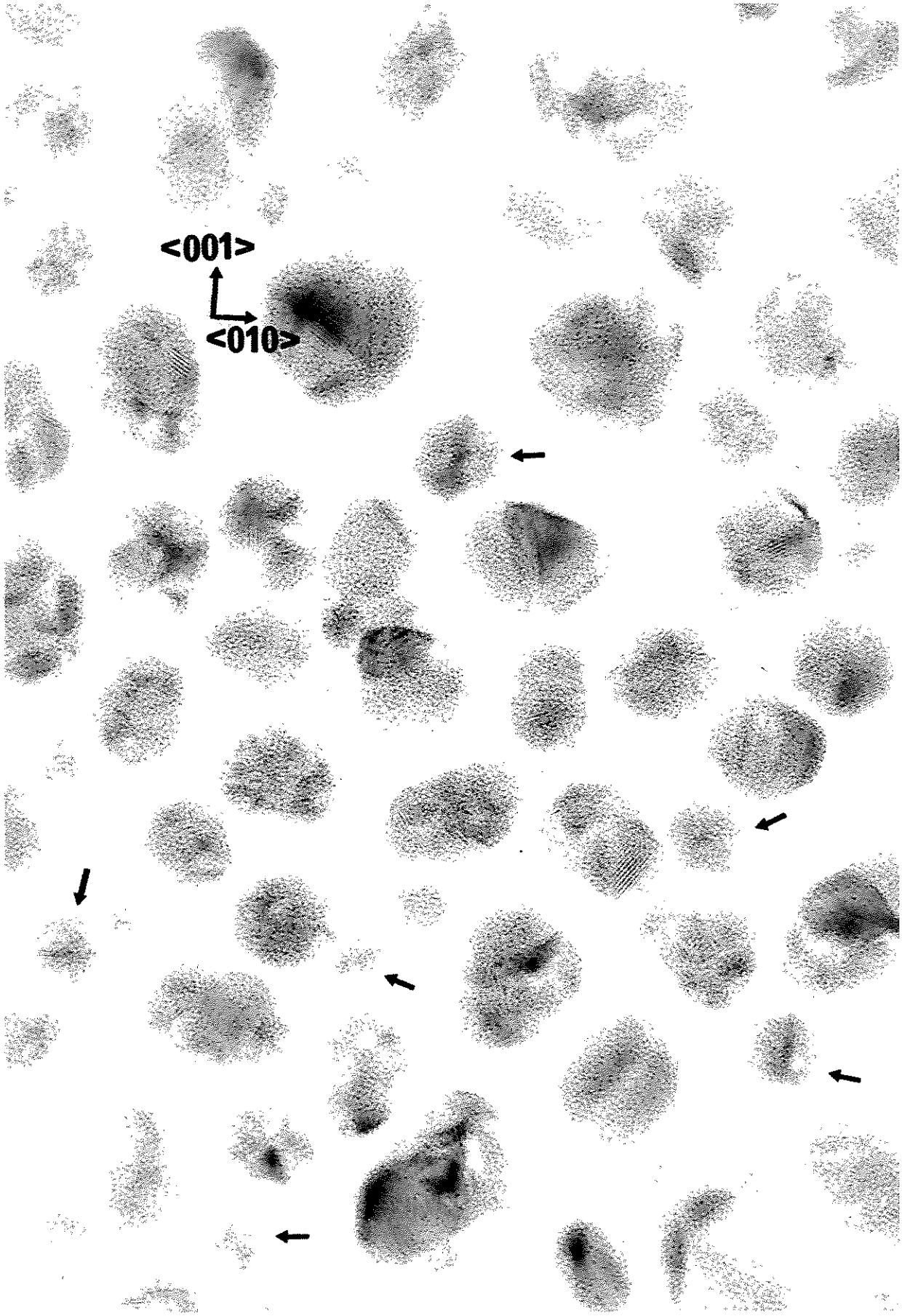

Figure 5.4 A typical field of view of the Au sample. The principal particle types present are Ics (arrowed) and polyparticles (discussed in chapter 6). The epitaxial directions of the substrate are indicated.

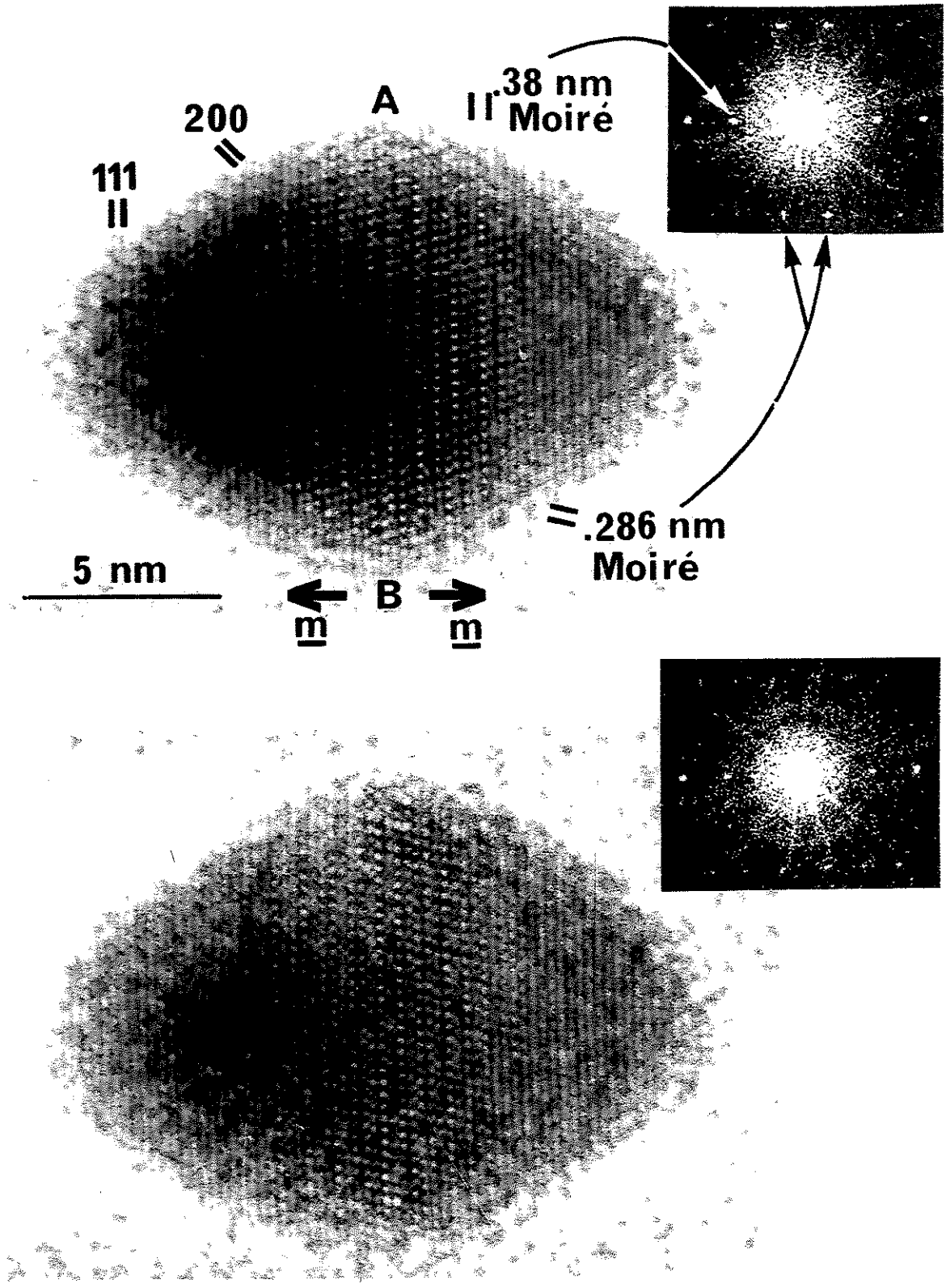

Figure 5.5 Two micrographs of a <100> epitaxed Dh near to the defocus values where δ=0 for the (111) fringes (top) and the (200) fringes (bottom). Optical diffractograms are inset. Of interest are the contrast changes with defocus (the micrographs were printed under identical conditions); the fine variations of the (111) lattice fringes (when viewed from the side), and the kink in the .286 nm double diffraction fringes. This latter feature is due to the reversal in sign of the thickness vector, $\underline{m}$, across the line AB, as indicated.

complicated appearance of the central region of these particles arises from the presence of four double diffraction fringes superimposed upon the three primary lattice fringes (see the inset optical diffractograms, and the analysis in 2.3). The existence of very fine variations in the lattice fringes (as can be seen by viewing them from the side) should be noted in this and the subsequent figures. These are certainly due to small thickness and strain variations. Because of the problems analysed in 5.2, no attempt has been made here to interpret these features.

There is an interesting example here of the dynamical phase shifts analysed in 5.2.2: a distinct kink can be seen in the .286 nm double diffraction fringes along the axis labelled AB in the figure. This is produced by a reversal in the sign of m (for all the diffracting segments) along this axis. This suggests that the particles are similar in their external shape to a decahedron (on its side), without any of the re-entrant surfaces described in 3.3.

The appearance of the <111> oriented Dhs is shown in Figure 5.6. In terms of their diffraction, these appear to correspond to those analysed by Heinemann et al (1979). An interesting problem is posed by the Moire fringes present in these particles which, as observed by Heinemann et al (1979), are straight (see Figure 5.6 from a distance, or see Figure 5.3). These authors have interpreted this result as evidence against the presence of inhomogeneous strains, which they predicted would produce bent Moire fringes. However, this prediction is incorrect. Utilising de Wit's solution for the strains (4.2.2), any point X,Y in the precursor MTP is mapped to the point X',Y' where

$$X' = (\rho + u_\rho)\cos(\theta + u_\theta/\rho) \quad \text{, and}$$

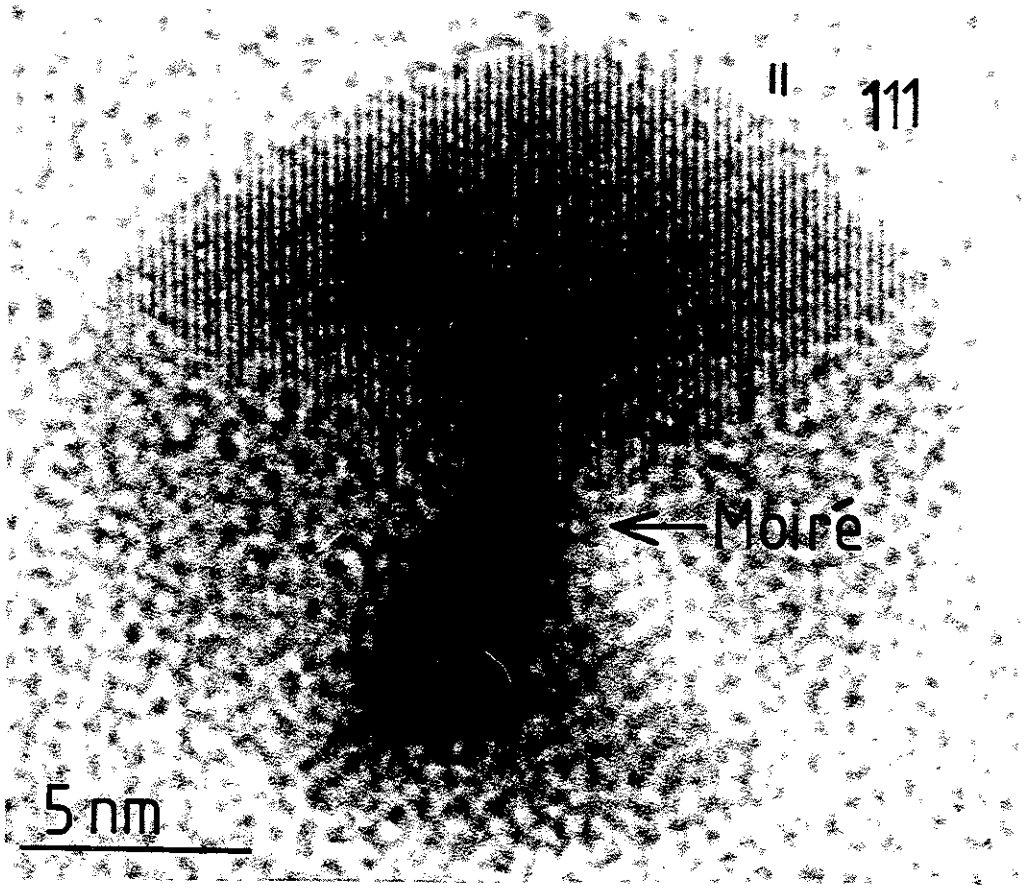

Figure 5.6 Micrograph of a <111> epitaxed Dh. The (111) lattice fringes are slightly bent, probably as a result of small changes in the thickness vector or inhomogeneous strains. The (222)-(220) Moire fringes are straight (to within a degree or two), a feature which, as is explained in the text and illustrated in Figure 5.7, proves very little.

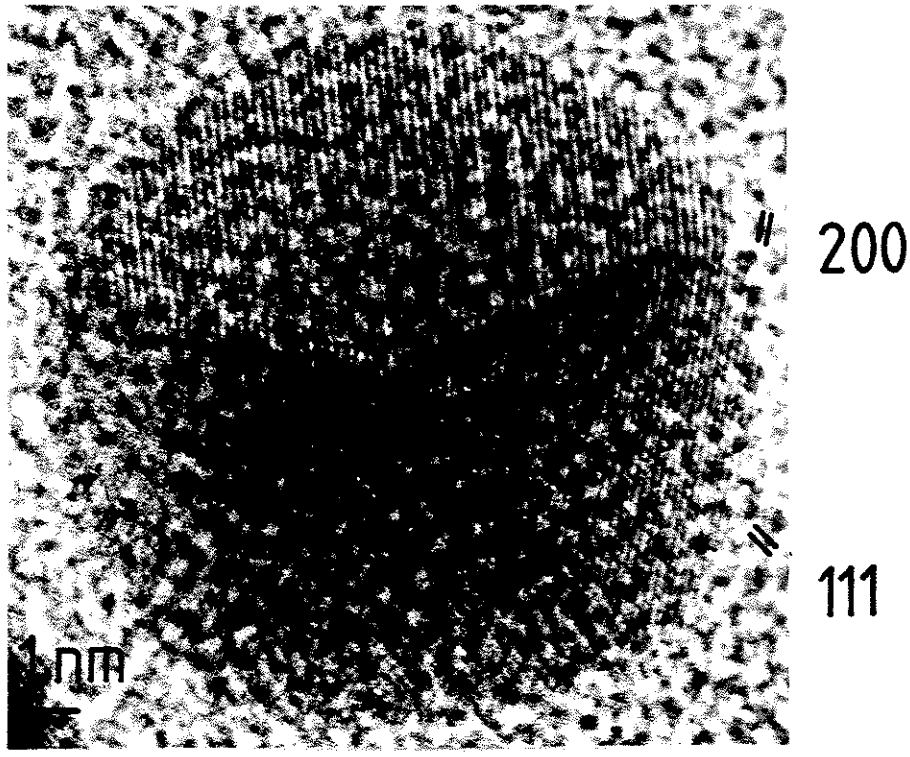

Figure 5.8 A Dh near to the 5-fold symmetry orientation. Two possible partial dislocations are indicated which might be artifacts caused by π (half fringe) phase shifts between the thickness fringes.

Considering now a set of planes parallel to the X axis, these are rotated by an angle ψ where

$$\text{Tan } \psi = dY'/dX'$$

$$\approx \text{Tan}\left(u_0/\rho\right) = \text{Tan}\left(\frac{\Theta \Delta\Omega^{Dh}}{4\pi}\right)$$

Hence the rotations present are very small, and (as noted by de Wit 1972) the accurately drafted strain field is almost undetectable. Even when two sets of planes are superimposed to simulate the formation of these Moire fringes, practically no rotations can be detected, as is shown in Figure 5.7.

A third orientation was observed in a few cases (Figure 5.8) where the particles were tilted to the <110> orientation (probably as a result of disturbances during the transfer of the specimens onto the microscope grids). With the particles in the figure some defects are visible which might correspond to partial dislocations. If these are edge dislocations, they are in the correct positions for a $7\frac{1}{2}^{o}$ (i.e. completely strain relieving) grain boundary. However, there is an alternative explanation. Careful examination reveals that there are thickness fringes present here with $\xi_g^{dt} \approx 85$ Å. The half fringe phase shifts that these are associated with (see 5.2.2) are just visible in the particles and appear to be the cause of these apparent defects.

5.4.2 Icosahedral MTPs

The Ics have no (100) surfaces, in contrast to the Dhs, and so have no <100> epitaxy. In fact, for Ag a complete <112> epitaxy (i.e. along a twin boundary) was observed with the (111) and the (110)

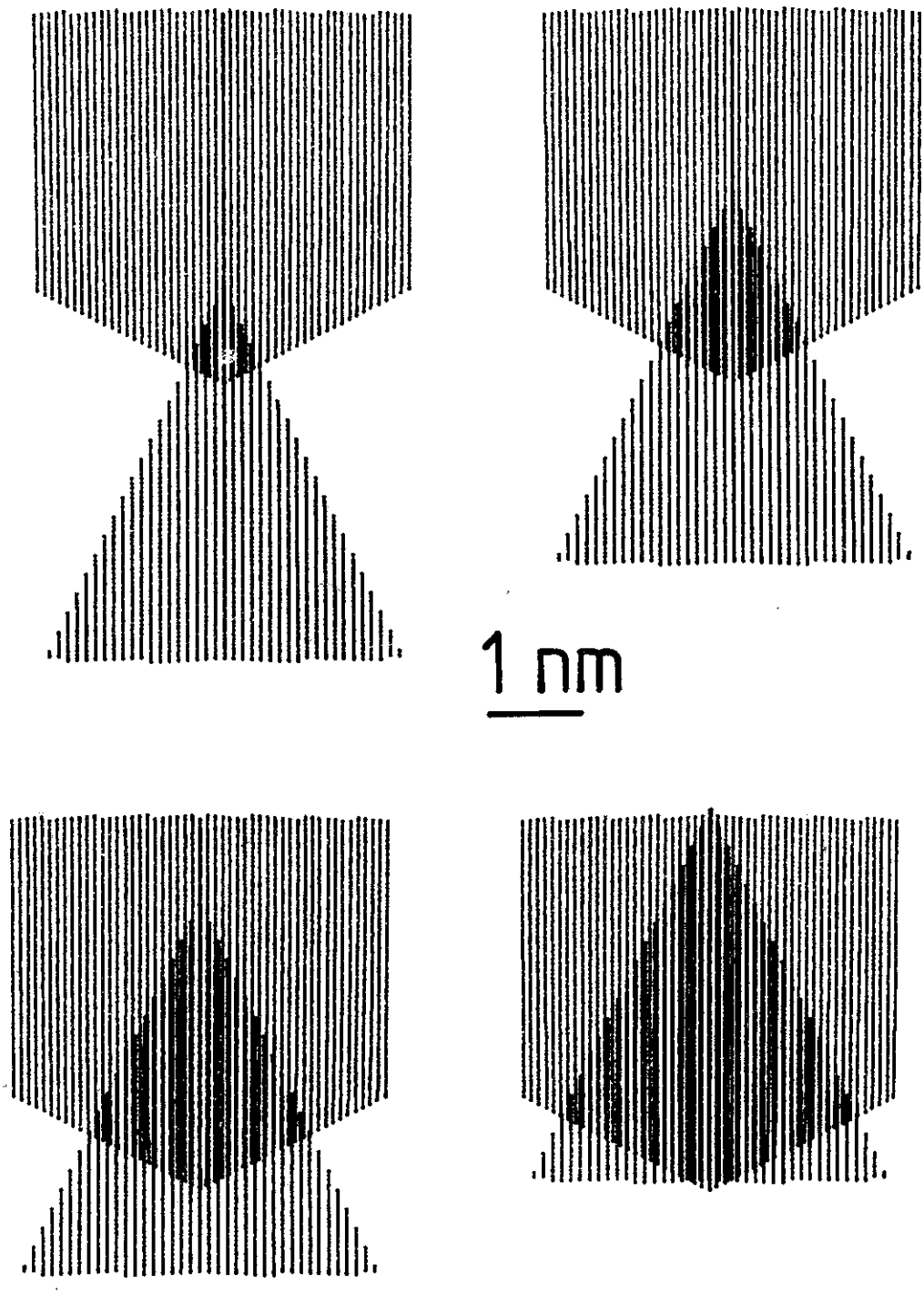

Figure 5.7 Simulation of the (222)-(220) Moiré fringes in a <111> oriented Dh. The figure shows the result of superimposing the (222) and (220) lattice planes in a 10 nm radius particle, using the displacements described in 4.2.2. The rotations of the Moiré fringes are vanishingly small.

planes in two of the microcrystallites parallel to the substrate (100) planes. For gold, the epitaxy was either <111> or (to a lesser extent) <112> , similar to that reported by Heinemann et al (1979).

The lattice fringe configuration for the <112>oriented particles is shown in Figures 5.8 and 5.9 and is in good agreement with the theoretical predictions in 2.3. The large Moire fringes present in these particles (view Figure 5.8 from a distance, or (more clearly) in Figures 5.3 and 5.9) had rather complicated forms, the precise details of which varied from particle to particle. Similar to the analysis presented in 5.4.1 for the Dhs, the reasonably straight nature of these fringes (i.e. the absence of a 30° splitting as predicted by Heinemann et al 1979) proves nothing about the presence or absence of inhomogeneous strains. In fact, any attempt (e.g. that by Gillet et al 1976) to interpret this type of variation in the structure of Moire fringes without precise image calculations is very dangerous. Small thickness variations, inhomogeneous strains or the presence of partial dislocations could produce this behaviour.

A number of clear defects in the lattice fringes were observed in these Ics, two of which are indicated in Figure 5.8. These may be partial edge dislocations. However, it is not clear whether these are real defects present in the object Ics, or anomalies of the imaging process. It is felt that further, corroborative evidence is required before positive interpretations are attempted.

In the particles with the <111> epitaxy a very different fringe configuration was observed, as shown in Figure 5.10 and Figure 5.11. As has been previously analysed in 2.3, this arises from the presence of (111), pseudo-(111) double diffraction and (220)-(222) Moire fringes. These Moire fringes were relatively straight (see Figure 5.11 from a distance or Figure 5.4). This proves very little,

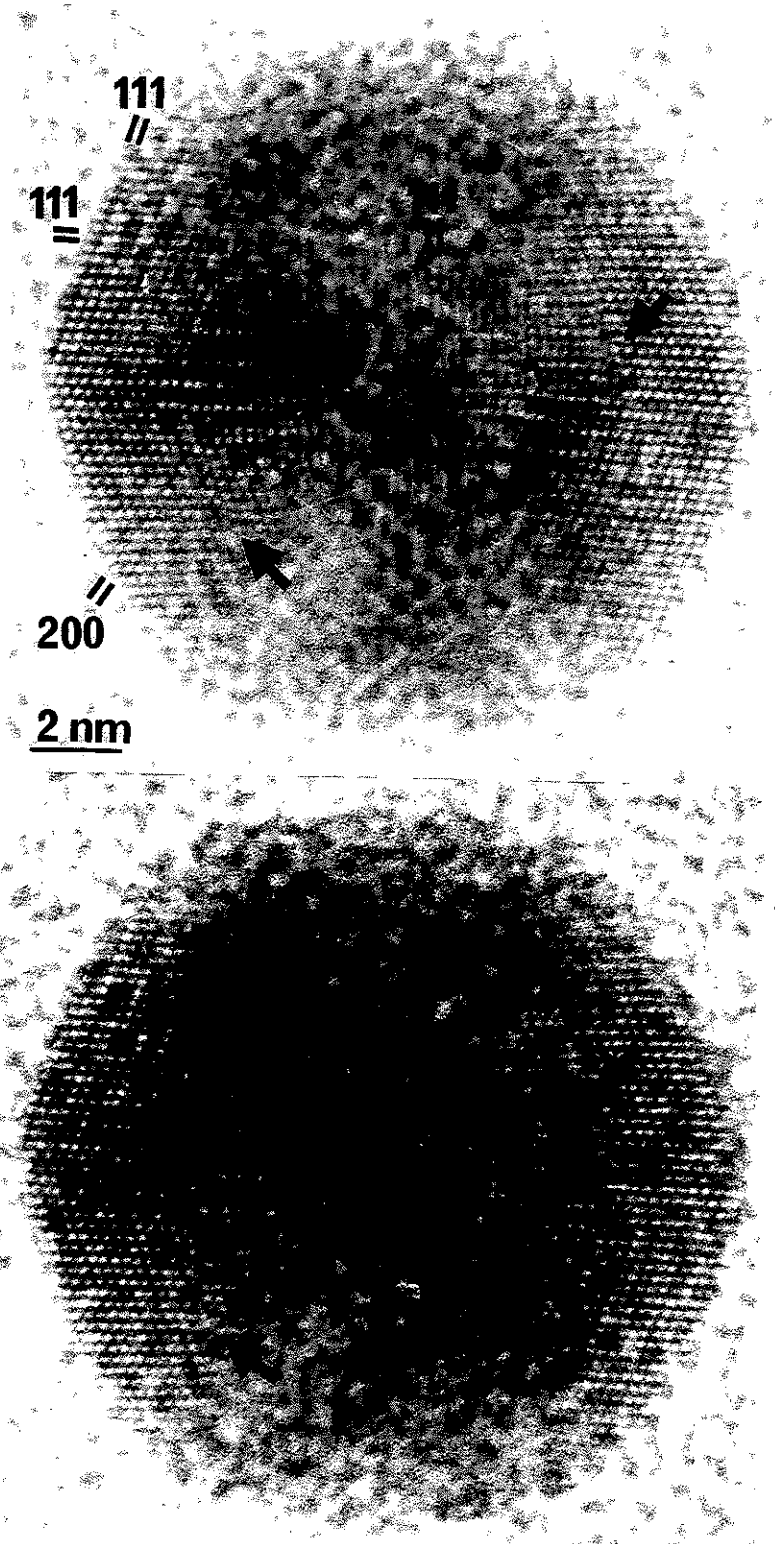

Figure 5.9 Two members from a through focal series of a <112> oriented Ic. The defocus values are those for which δ=0 for the (111) lattice fringes (top) and (200) lattice fringes. The positions of two possible partial dislocations are indicated. Also of interest are the slightly bent nature of all the lattice fringes, and the complicated appearance of the (222)-(220) Moire fringes.

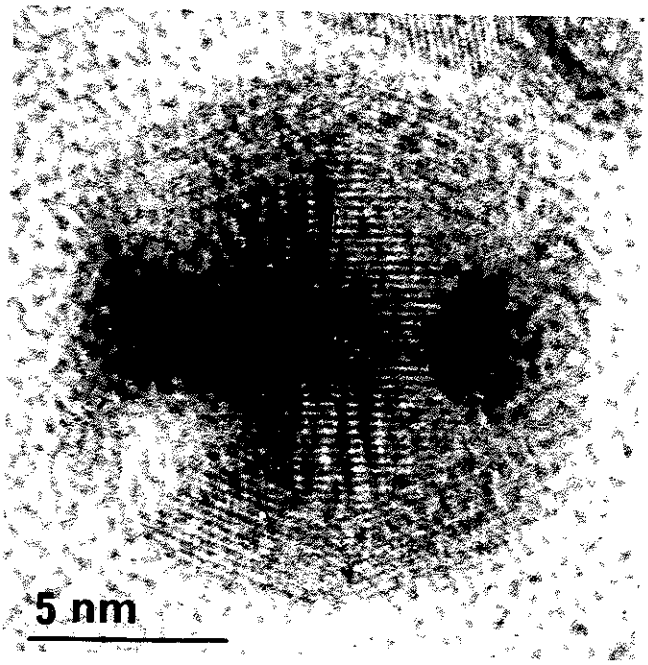

Figure 5.10 A 112 oriented Ic of Au. For reasons that are not understood, the lattice fringes in the Au particles with this epitaxy were not as 'clean' as the corresponding Ag particles.

Figure 5.11 A <111> oriented Ic of Au, with the positions of two possible partial dislocations indicated. The bending of the lattice fringes (all of which are (111) or pseudo-(111) double diffraction fringes) should be noted. The Moire fringes here are almost straight, which proves very little about the presence or absence of inhomogeneous strains. A small Dh near to the 5-fold symmetry orientation is shown on the lower right.

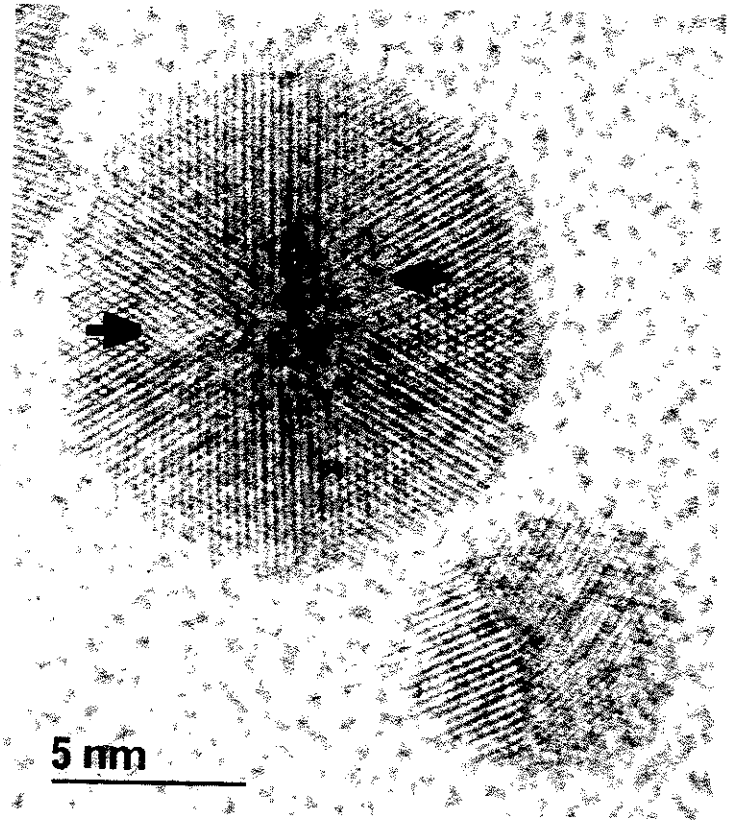

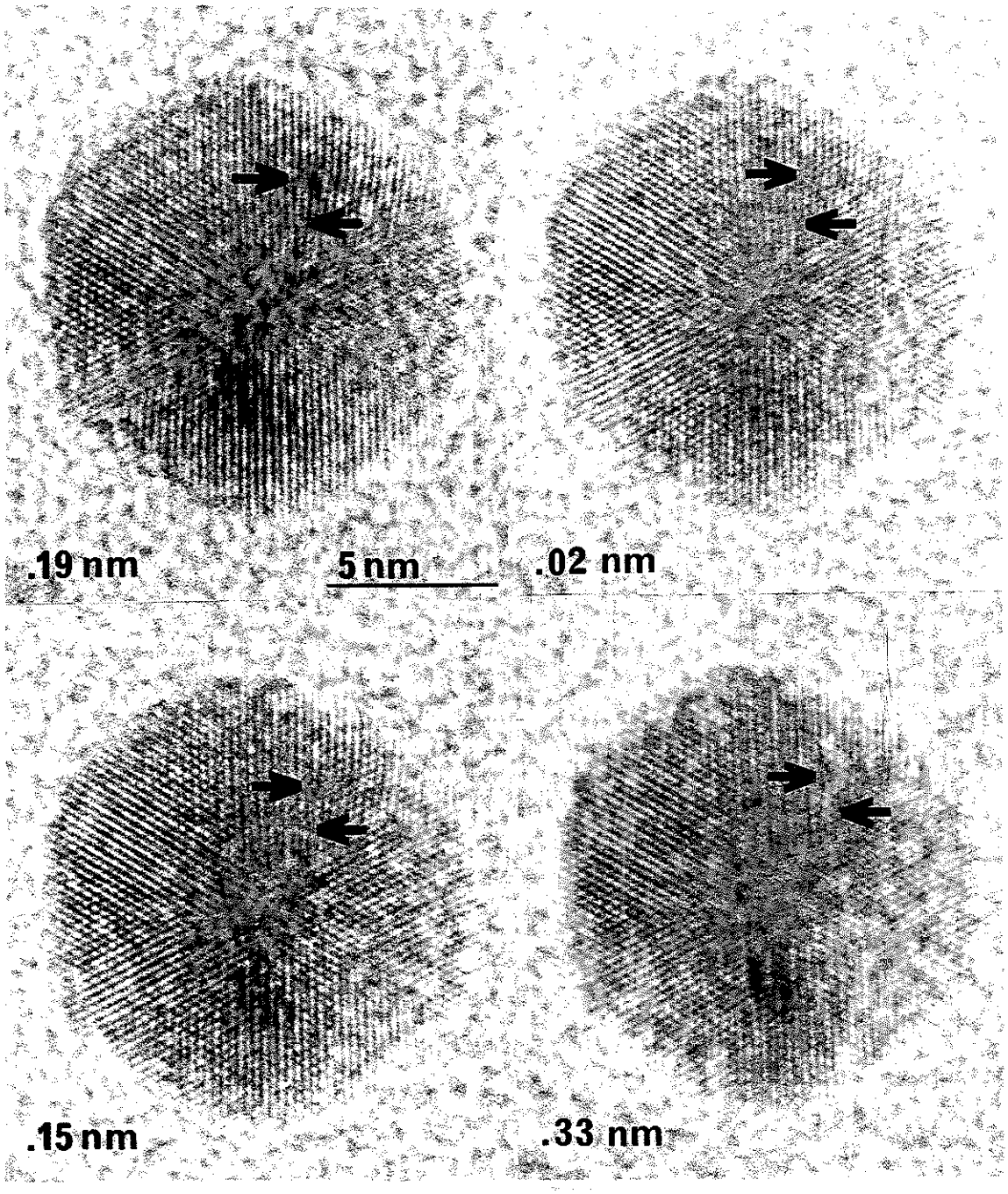

Figure 5.12 Four members from a through focal series of a <111> oriented Ic of silver. Two possible partial dislocations are indicated on the figure. One of the more interesting features is how little the positions of these defects, and the general contrast varies with defocus (quoted on the lower left of each particle as approximate values of $|\underline{\delta}|$ for the (111) fringes).

contrary to the interpretation of Heinemann et al (1979).

A number of possible partial dislocations were imaged in these Ics, two of which are indicated in Figure 5.10. As with the <112> oriented Ics, it is felt that a positive identification of these features requires corroborative evidence.

5.5 Discussion

It should be clear from the results presented above that high resolution lattice imaging is a particularly powerful method of obtaining experimental information from small particles. Very fine fringe-variations and possible partial dislocations have been clearly imaged. However, interpreting the experimental data is not trivial, for the reasons discussed in 5.2: the micrographs are not structural images.

To a large extent these problems with the interpretation of the results occur because the particles under study are complicated . MTPs, which are a collection of microcrystallites with twin boundaries, thickness variations and possible inhomogeneous strains or dislocations, provide an opportunity for all the known artifacts (and probably, as well, those yet to be discovered) to occur. It is for this reason that the observed defects have been interpreted as "possible partial dislocations". Further corroborative evidence is required for a more positive identification (much of which work the author hopes to perform himself).

The most powerful approach for further work is probably the combination of axial dark field images with direct lattice resolution. (At the time of this thesis, no dark field facilities were available on the microscope employed.) For example, relatively low resolution

(e.g. 10 Å) characterisation of the microcrystallite thicknesses (and the Burger's vectors of any partial dislocations) should permit an interpretation of the high resolution detail available in the lattice fringes. It should be noted that interpretations of the dark field images could be quite difficult. The artifacts present at the crystal exit surface (5.2.2) could cause problems, in particular the wedge splitting of the beams. (For example, this splitting of the diffracted beam will produce inaccurate results when the Selected Zone Dark Field method of Heinemann and Poppa 1975 is used to decipher the diffraction patterns.) Furthermore, weak beam images of any dislocations might easily be lost in the carbon speckle. It may be for this reason that dislocations have never been reported in small MTPs.

An alternative approach would be to obtain better image calculations than the approximate discussion provided in 5.2. Ideally these would be full image simulations, but this is not plausible at present. Current programmes employ a grid, so that a particle large enough to be relevant, with a grid size small enough for the fine variations observed, will cause severe storage problems.

In conclusion, small ($\sim$20 nm diameter) MTPs, particularly Ics, may contain large numbers of strain-relieving partial dislocations. These defects can be readily observed by direct lattice imaging at 500 kV. However, it is felt that corroborative evidence is required to eliminate the possibility that these defects are anomalies of the imaging process.

CHAPTER 6

HIGH RESOLUTION STUDIES OF SINGLE CRYSTALS, LAMELLAR TWINNED PARTICLES & POLYPARTICLES

6.1 Introduction

This chapter deals with results which demonstrate the utility of lattice imaging as a means of directly identifying and characterising small particles. The major advantage of this technique is that all reasonably strong (111) and (200) dark field images are effectively recorded simultaneously on a single micrograph with full directional information and very high spatial resolution. This is of substantial convenience for decoding complicated particles. It is shown that many particles can be classified under the broad heading of "polyparticles", which are similar to polycrystals but with definite particles (e.g. Ics) replacing single crystals as the basic units.

6.2 Experimental Details

The same samples and operating conditions were employed as described in 5.3.

6.3 Results

6.3.1 Single Crystals

The single crystal particles observed were shaped in the same way as described in previous work for similar epitaxially grown particles (e.g. Ino 1966): nearly square shapes with a <100> epitaxy (Figure 6.1), and triangles for the <111> epitaxy (Figure 6.2). A few rectangular <100> particles were also observed, almost

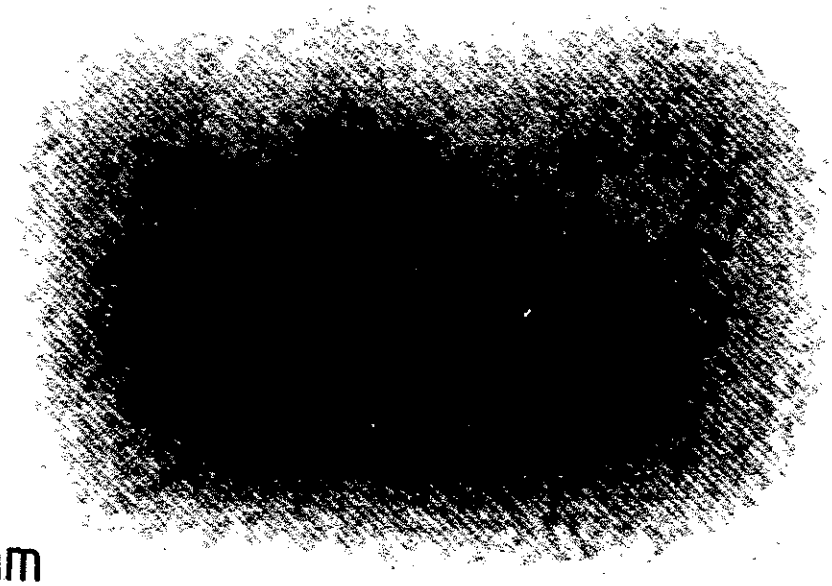

Figure 6.1 Micrograph of a typical, slightly rectangular, <100> epitaxed Ag single crystal. Crossed (020) and (002) lattice fringes are evident.

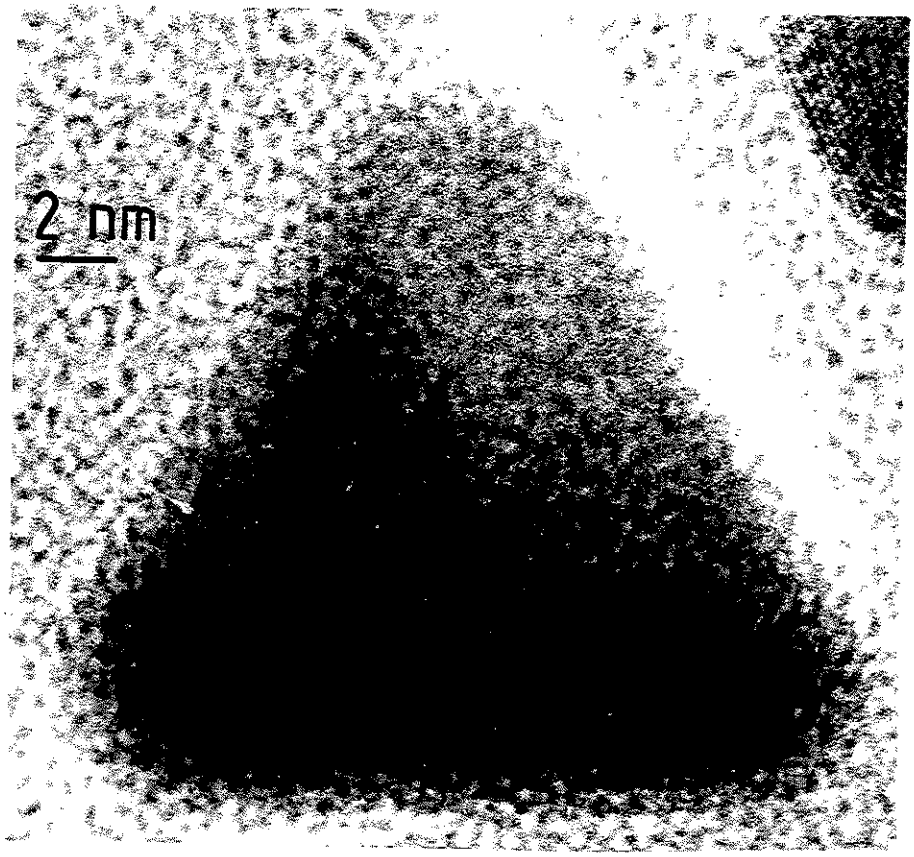

Figure 6.2 Triangular Ag particle with a <111> epitaxy.

is shown in Figures 6.3 and 6.4. In Figure 6.3, the (200) lattice fringes display a definite orientation change along a line between the two arrows marked, indicating either a low angle grain boundary or a sharp change in thickness. Both of these are associated with late stages in coalescence. Figure 6.4 shows two particles frozen, probably by the cooling of the substrate, in the necking stage of coalescence (Pashley et al 1964).

6.3.2 Lamellar Twinned Particles

These particles (lamellar twinned particles or LTPs) are characterised by a number of parallel twin boundaries, though the simplest example, shown in Figure 6.5, has only one twin boundary. It is possible to classify them as a simple type of polycrystal, but their frequent observation (see Hayashi et al 1977) suggests that they should be considered as a distinct particle type.

6.3.3 Polyparticles

A very common observation was of particles which appeared to contain MTPs or LTPs "embedded" among other crystals or recognisably coalesced with them. The MTPs were readily identified by the characteristic pattern of their lattice fringes (see 5.4).

(a) Polyicosahedral MTPs

These particles have the general form of Ics sharing decahedra. The simplest example is the bi-icosahedral MTP, shown in Figure 6.6, upon which the two epitaxial directions for the silver

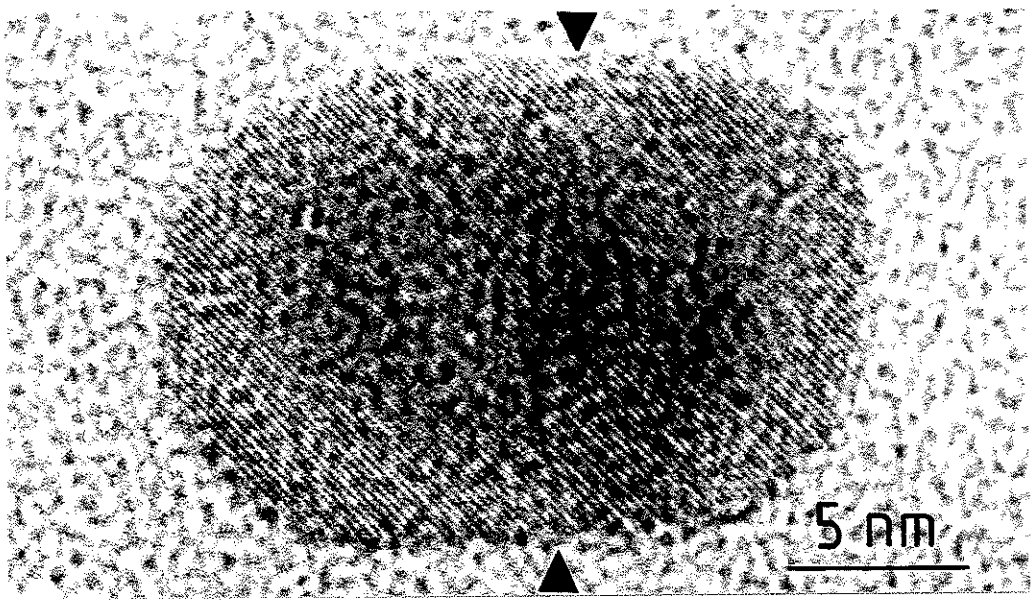

Figure 6.3 Micrograph of a rectangular <100> Ag particle showing evidence for particle coalescence. There is a definite change in the lattice fringe orientation on a line between the two arrows, indicating either the presence of a low angle grain boundary or a sharp change in the thickness vector.

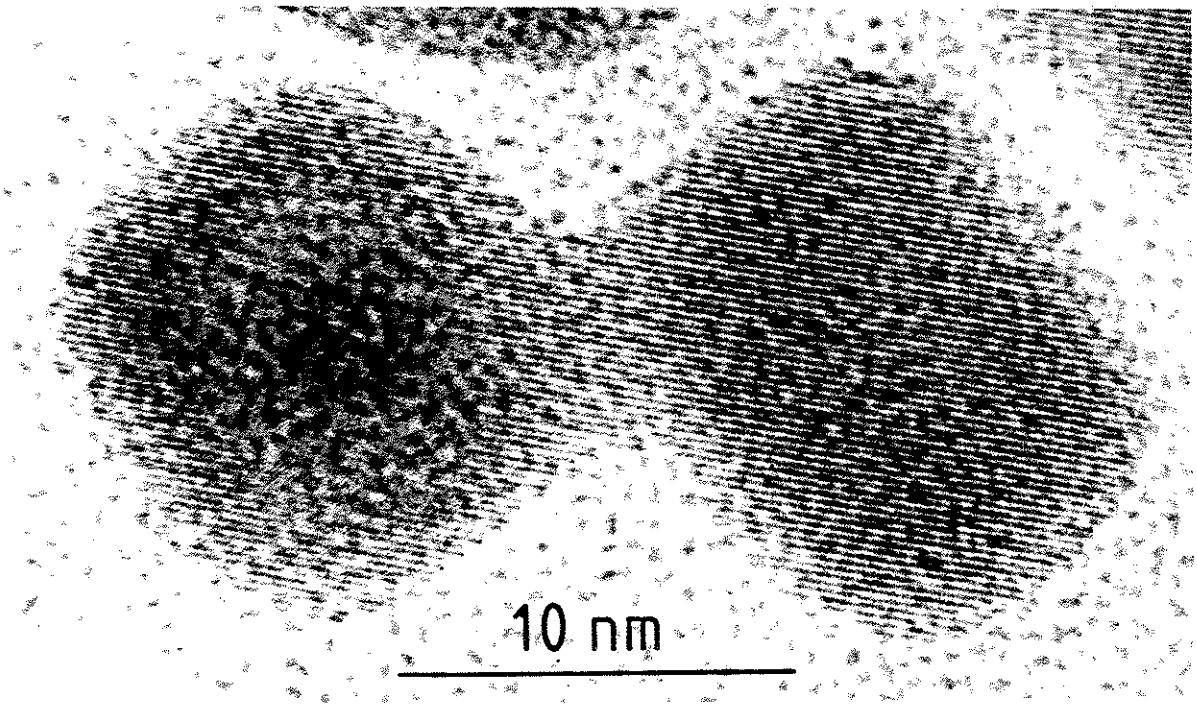

Figure 6.4 Two <100> oriented Ag particles 'frozen' in the necking stage of coalescence.

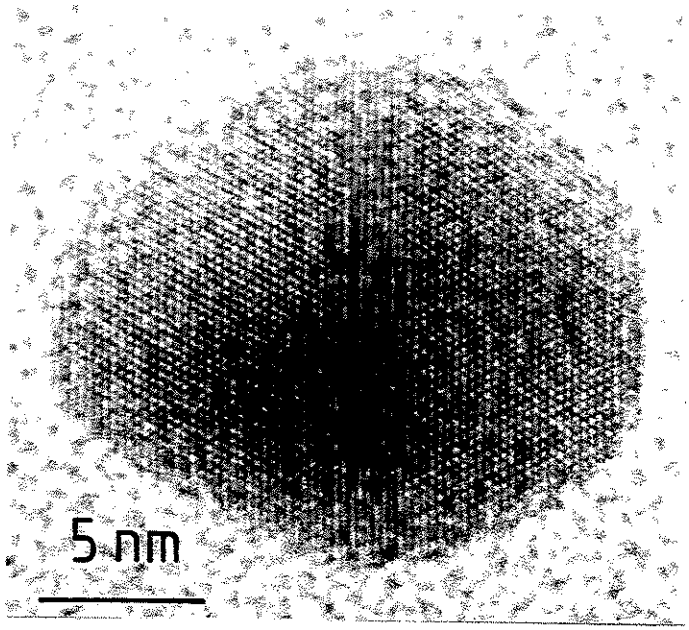

Figure 6.5 A silver LTP imaged down the shared <110> axis. The position of the twin boundary is very ill-defined.

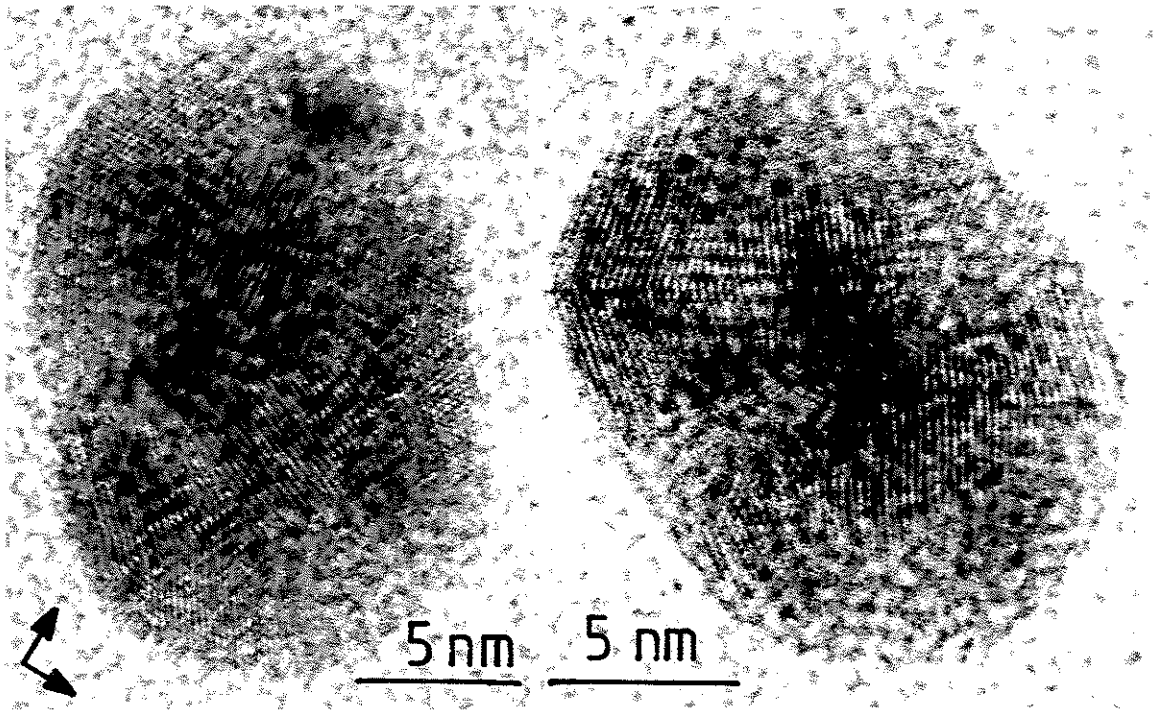

Left hand side:
Figure 6.6 Bi-icosahedral MTP of silver, probably a result of inter-particular coalescence. The two epitaxial directions of the Ics on the substrate are indicated.

Right hand side:
Figure 6.7 A composite particle (Ag) which provides evidence for coalescence as the source of polyicosahedral MTPs. Two <112> epitaxed Ics are shown, frozen in the process of coalescing into a single Ic.

Ics are also marked. It is clear that neither of the particles is adopting the epitaxial alignment, suggesting that the polyparticle was produced by coalescence of two Ics, rather than nucleation of a second Ic upon the first. (A nucleation process would be expected to occur with one of the MTPs epitaxially aligned.) Particles resembling coalesced MTPs were suggested by Ino (1966) and Komoda (1968), although neither were able to provide clear structural identifications.

Further evidence of a coalescence mechanism for the formation of these particles is shown in Figure 6.7 and 6.8. The composite particle in Figure 6.7 seems to be two Ics, with the same orientation, in the process of coalescing into a single Ic. Figure 6.8 shows an Ic necking to another which is itself part of a composite particle. The continuity of the lattice fringes between the Ics should be noted.

(b) Icosahedral-Decahedral MTPs

In much the same way as described above for polyicosahedral MTPs, these particles are the result of combining an Ic and a Dh by sharing two tetrahedral segments. An example is shown in Figure 6.9. Not only does this structure occur separately, but it also appears as part of a more complicated particle. Figure 6.10, for example, shows a Dh bridging two Ics , in perfect register with the right-hand Ic.

(c) Decahedral-Lamellar MTPs

This particular structure (Figure 6.11) again in a similar way to those described above, corresponds to a low energy matching

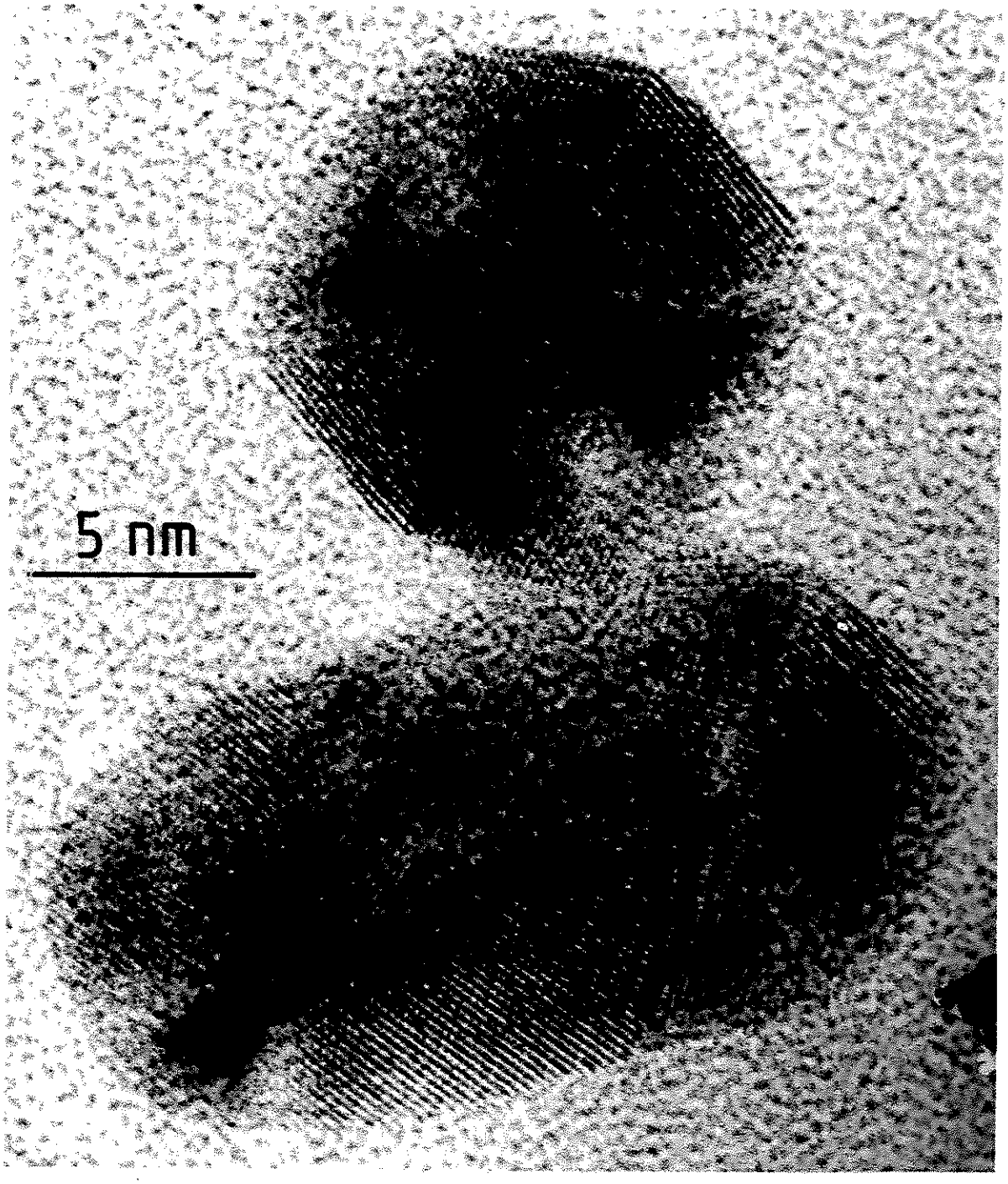

Figure 6.8 Coalescence between an Ic and an elongated bi-icosahedral MTP. The continuity of the lattice fringes across the 'neck' should be noted.

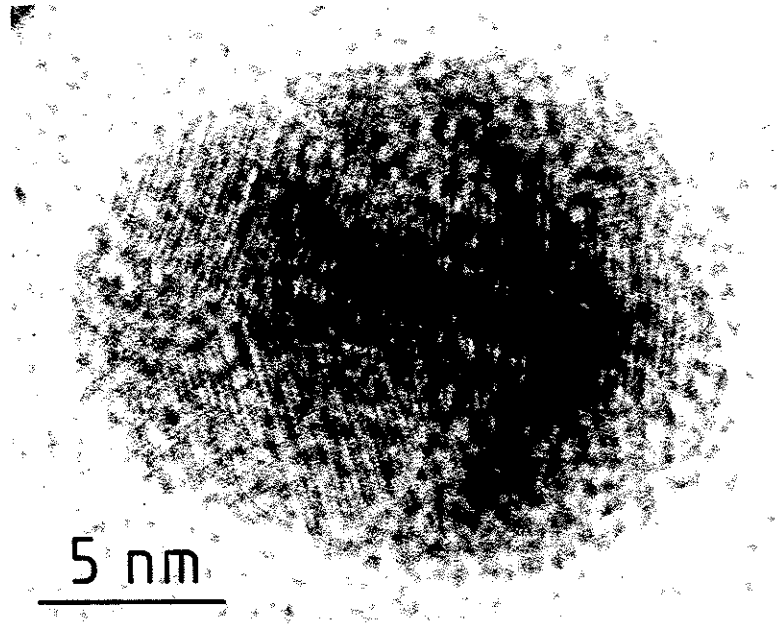

Figure 6.9 Icosahedral-Decahedral MTP. An Ic, on the right, and a Dh, on the left, are sharing two tetrahedral segments. Silver is again the metal.

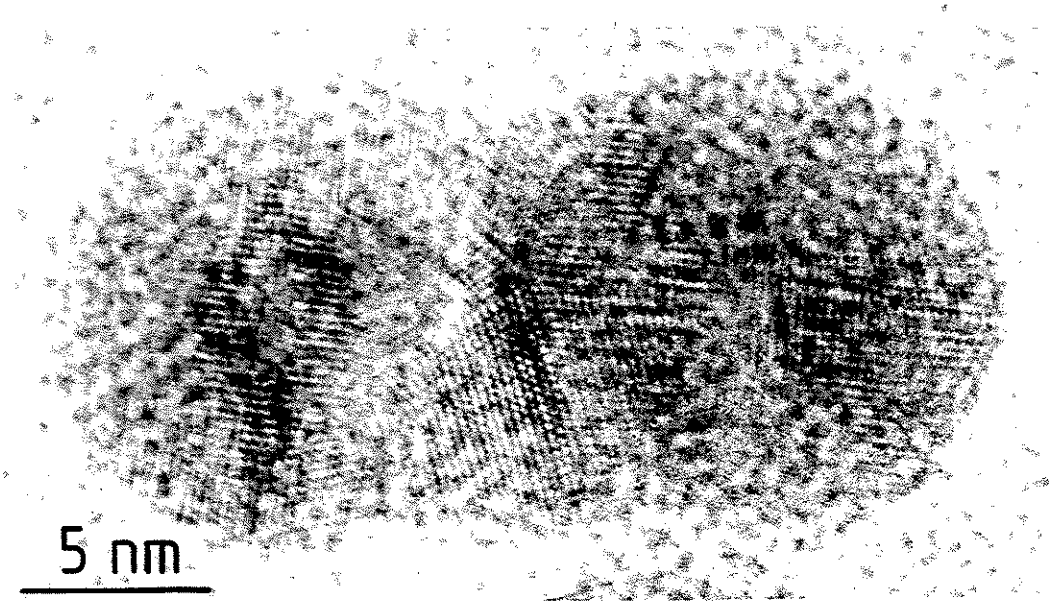

Figure 6.10 Example of a Dn bridging two Ics taken from the Ag sample.

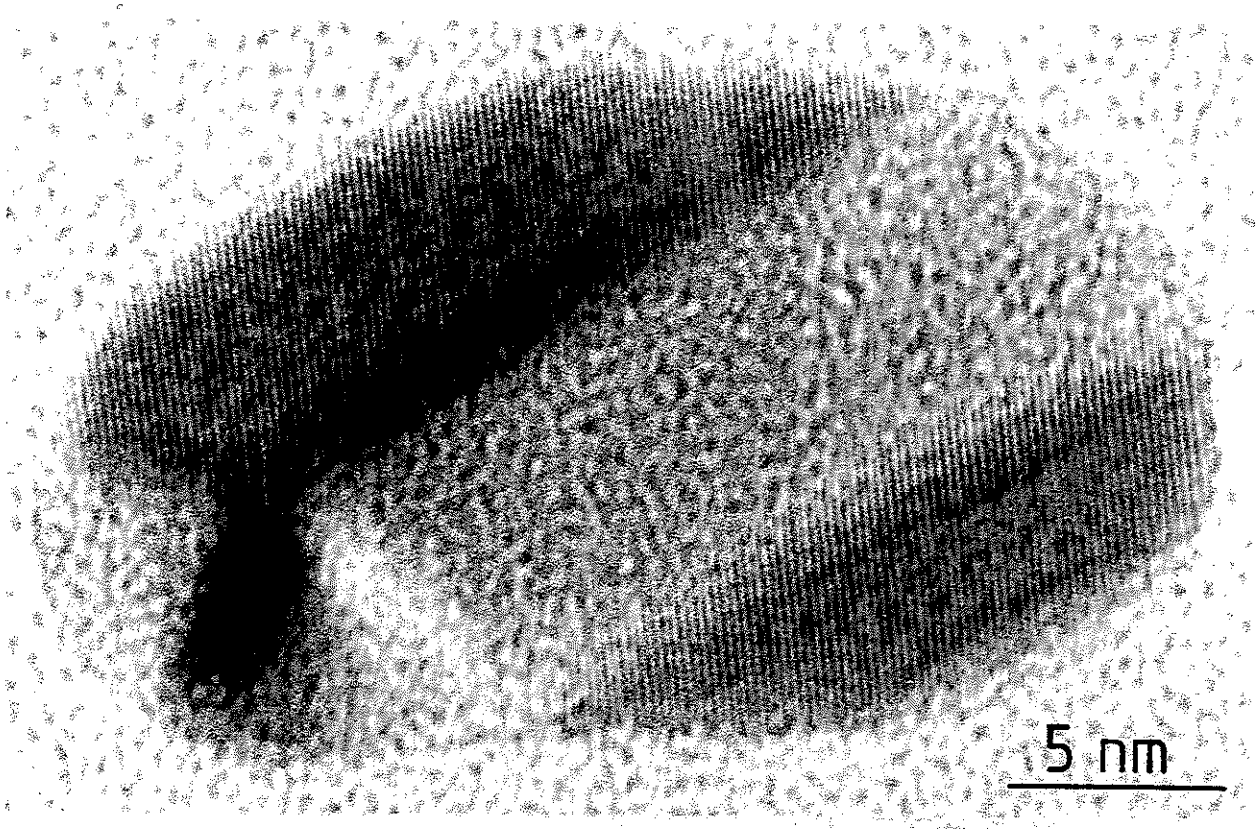

Figure 6.11 A Decahedral-Lamellar MTP of Ag. A strong (220) 'ghost' image from one of the Dh segments is clearly visible.

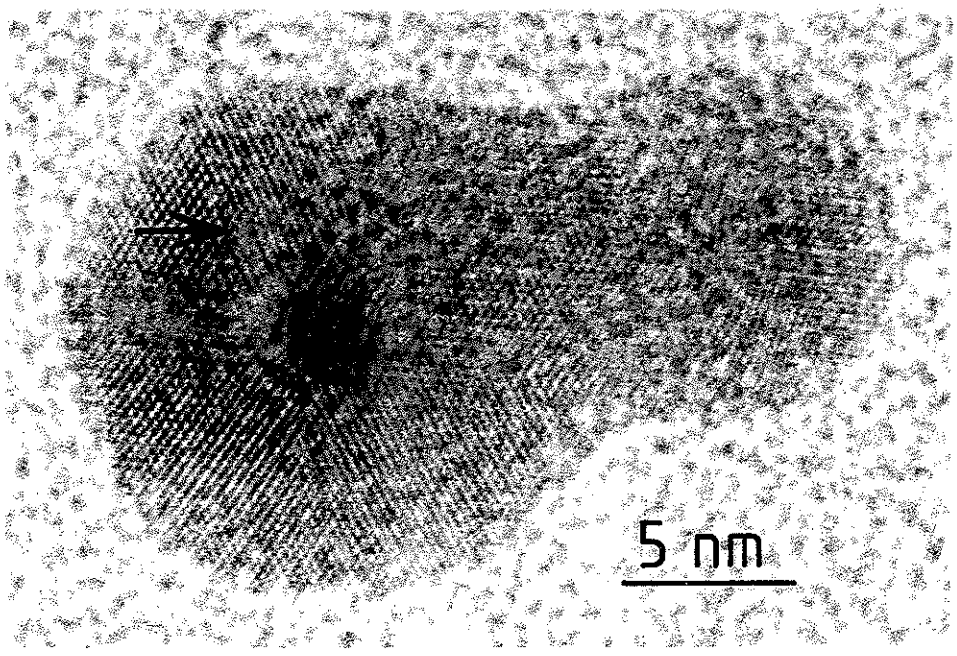

Figure 6.12a An unidentified Au polyparticle. The left hand particle is a ⟨111⟩ oriented Ic, which has colalesced with the particle on the right (a possible Ic). A possible partial dislocation (see 5.4.2) is indicated in the figure.

6.11 would be a Dh with two rather extended segments and an additional twinned segment. However, the classification as decahedral-lamellar MTPs is more consistent with the manner in which these particles are probably formed, i.e. by coalescence.

(d) More Complicated Polyparticles

Particles where an identifiable segment was embedded in a large undecodable region were also frequently observed. A number of typical examples are shown in Figure 6.12 and are explained in the figure captions. The present method of identification is not always capable of completely decoding these particles, though advances in the image resolution (e.g. resolving the (220) lattice fringes) may permit this.

6.2.4 Polycrystals

A number of particles were observed which could not be classified. Examples are shown in Figure 6.13. It is possible to give these the rather nebulous title of polycrystals, but this may be inaccurate. It is suspected that they are really polyparticles which are not in an orientation suitable for decoding their structures via lattice imaging.

6.4 Discussion

The predominant feature of the observations reported here is the manner in which various particles, such as MTPs and LTPs, appear to retain their integrity as units when involved in a larger

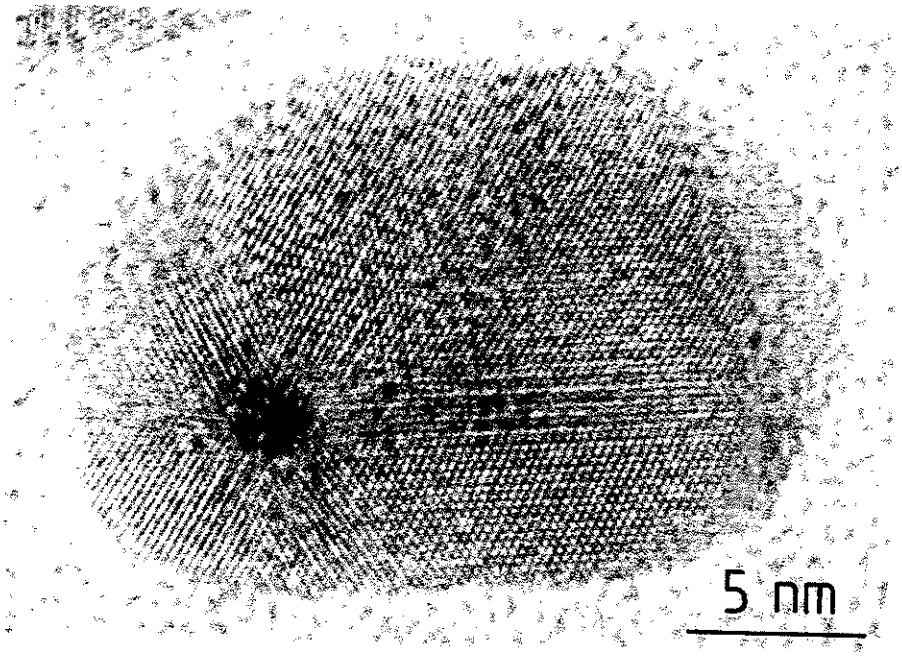

Figure 6.12b An unidentified Au polyparticle. A <111> oriented Ic is embedded in the lower left of the particle. possibly extending towards the right and top.

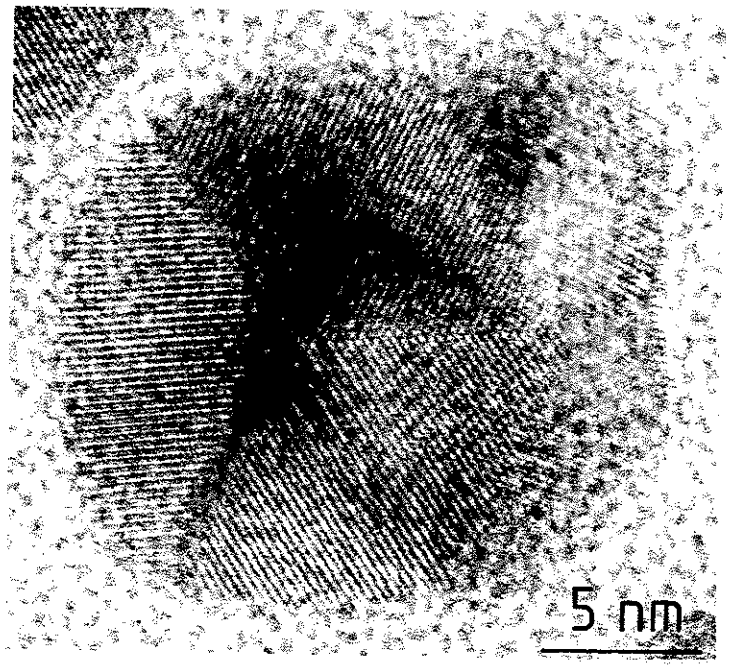

Figure 6.12c Unidentified Au polyparticle. The configuration of the lattice fringes on the left and center suggest the presence of half (bisected normal to the viewing direction) a <111> Ic. Some (222) half spacing fringes and (220) fringes are visible on the lower left.

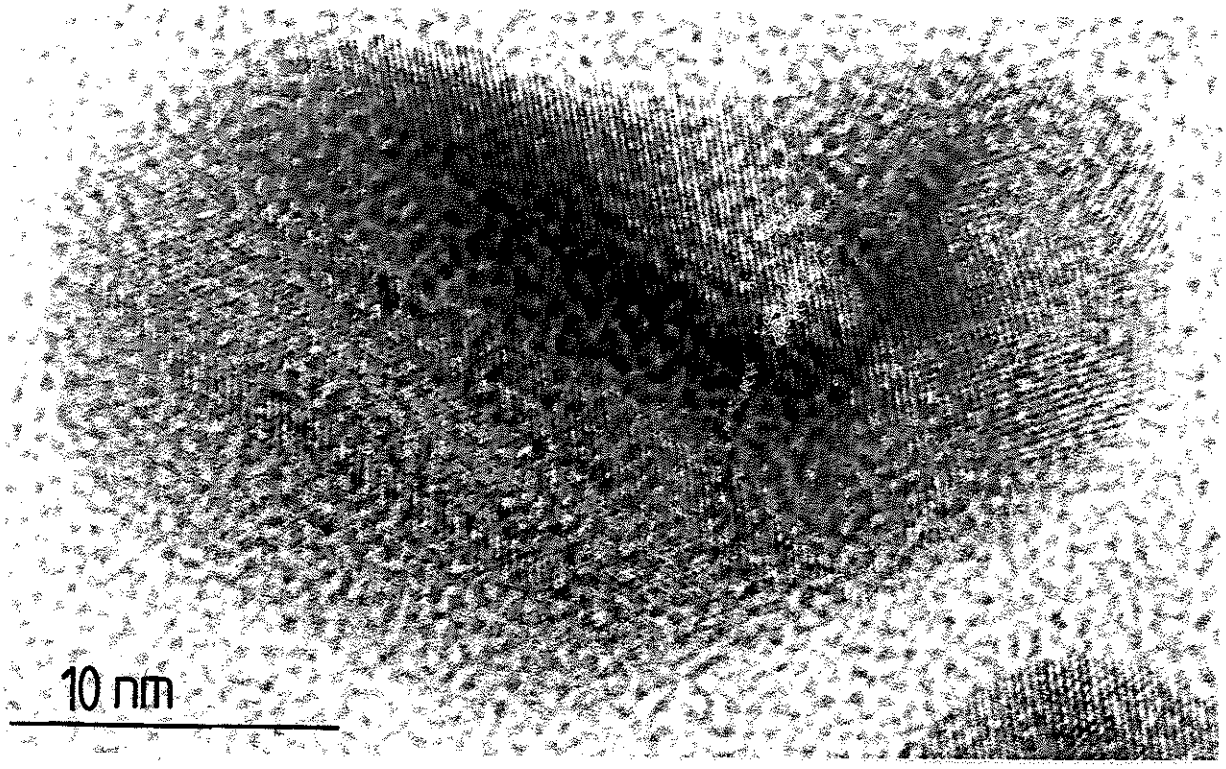

Figure 6.13a Possible polycrystal of Au. There is some evidence of lamellar twinning towards the left.

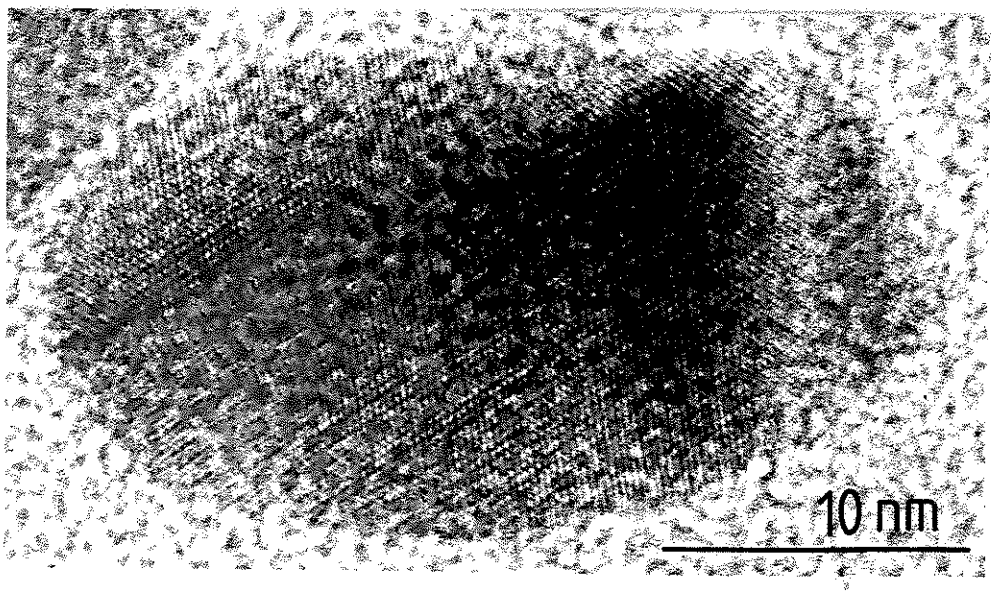

Figure 6.13b Another particle of Au which is tentatively identified as a polycrystal. There is again some evidence for lamellar twinning.

particle. In many ways, an analogy between polycrystals and polyparticles is useful: both are constructed from unit particles (single crystals or twinned particles respectively) with "grain boundaries" at the interfaces. The approach does not change qualitatively with more complicated units, but the rules for producing low energy grain boundaries do. In common with polycrystals, polyparticles appear to favour low energy grain boundaries. For example, the shared decahedra present in polyicosahedral MTPs are low energy boundaries between the Ics.

The stability of the polyparticles is unclear. The configurations may correspond to local energy minima stable to small perturbations, or they may be unstable intermediaries "frozen" with insufficient energy available for rearrangement to a more favourable structure. The former is suspected to be the case for at least some of the particles (for the reasons discussed in 5.7), although the matter will only be properly resolved by in-situ analysis of particulate growth and further theoretical analysis.

Finally, it is interesting to note the similarity between the structures observed here and some models for amorphous films. Various authors (e.g. Hoare and Pal 1970, Gaskell 1975 and Mistry 1979) have suggested polytetrahedral structures (which are polyicosahedral MTPs in a 3-D network) in amorphous materials. The observation of polyicosahedral MTPs appears to provide some circumstantial evidence for these models.

CHAPTER 7

MULTIPLY-TWINNED PARTICLES IN SILVER CATALYSTS

7.1 Introduction

In the introduction to this thesis, one of the motivations for the line of research conducted was stated to be the significance of small particles in heterogeneous catalysts. Having now presented in Chapters 3-6 a fairly extensive theoretical and experimental analysis of small particle structures, particularly MTPs, it is appropriate in this final chapter to investigate the relevance of this work to catalysis.

The possibility that MTPs are present in heterogeneous catalysts was first suggested by Allpress and Sanders (1970) and investigated be Avery and Sanders (1970). They found, however, that at most 2% of catalyst particles 10-35 nm in size (for Au, Ni, Pd and Pt on γ-alumina) were multiply twinned. Consequently the significance of these unusual structures in catalysis has generally been considered to be small.

In this chapter, the presence of considerable numbers of MTPs in a silver catalyst supported on α-alumina is reported and the possibility that these particles possess unusual catalytic behaviour is discussed.

7.2 Experimental Procedure

The samples examined were supplied by ICI Ltd., who prepared them as follows (UK Patent 1369639). An 0.8 M^2g^{-1} support of α-alumina (Carborundum Ltd., No. SAHT96) was immersed in a solution of silver oxalate in 45% water-45% ethylene diamine-10% ethanolamine. The support was then pyrolysed in nitrogen at 200° C for 1 hour to decompose the oxalate to silver metal. The catalyst examined

contained approximately 16% silver by weight. Samples were prepared for microscopy by allowing a drop of ground catalyst suspended in acetone to dry on amorphous carbon films premounted on microscope grids. These were examined with a Siemens 102 microscope at 100 kV and the Cambridge HREM at 500 kV (care being taken to avoid contamination or beam heating of the sample which was observed to sinter the silver).

7.3 Results

The samples examined consisted primarily of isolated metal particles of size between 100 and 200 nm, although smaller particles (< 50 nm) were occasionally found on amorphous regions of substrate and a few large polycrystals were observed. A typical, low-magnification micrograph is shown in Figure 7.1.

The discrete particles displayed well-developed 111 facets, with very little edge or corner rounding. More than 80% were observed to be icosahedra or decahedra; the remainder included twinned platelets, faulted needles and single crystals. Micrographs of these various morphologies are shown in Figures 7.2 and 7.3. All the Ics and most (but not all of the Dhs displayed internal contrast suggestive of dislocations, as noted previously for large MTPs by Saito et al (1978).

The larger polycrystals frequently displayed contrast similar to that observed in polyparticles (see 5.3.3). For example, the particle shown in Figure 7.4 contains a Dh combined with some other, unidentified microcrystallites. Their presence was attributed to particle coalescence (as suggested in Chapter 6), supporting evidence for which is shown in Figure 7.5.

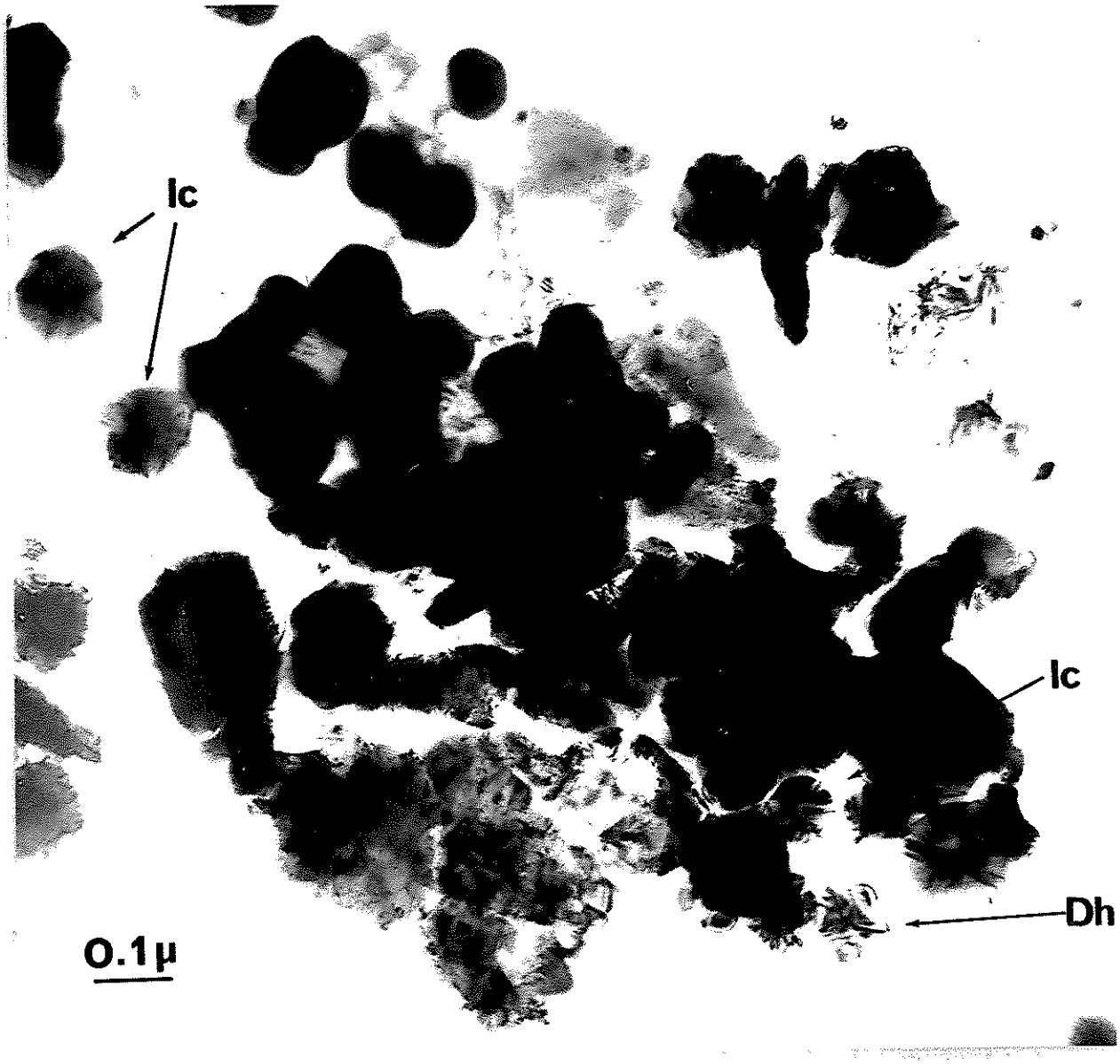

Figure 7.1 Low magnification micrograph of a catalyst specimen. MTPs are indicated on the figure.

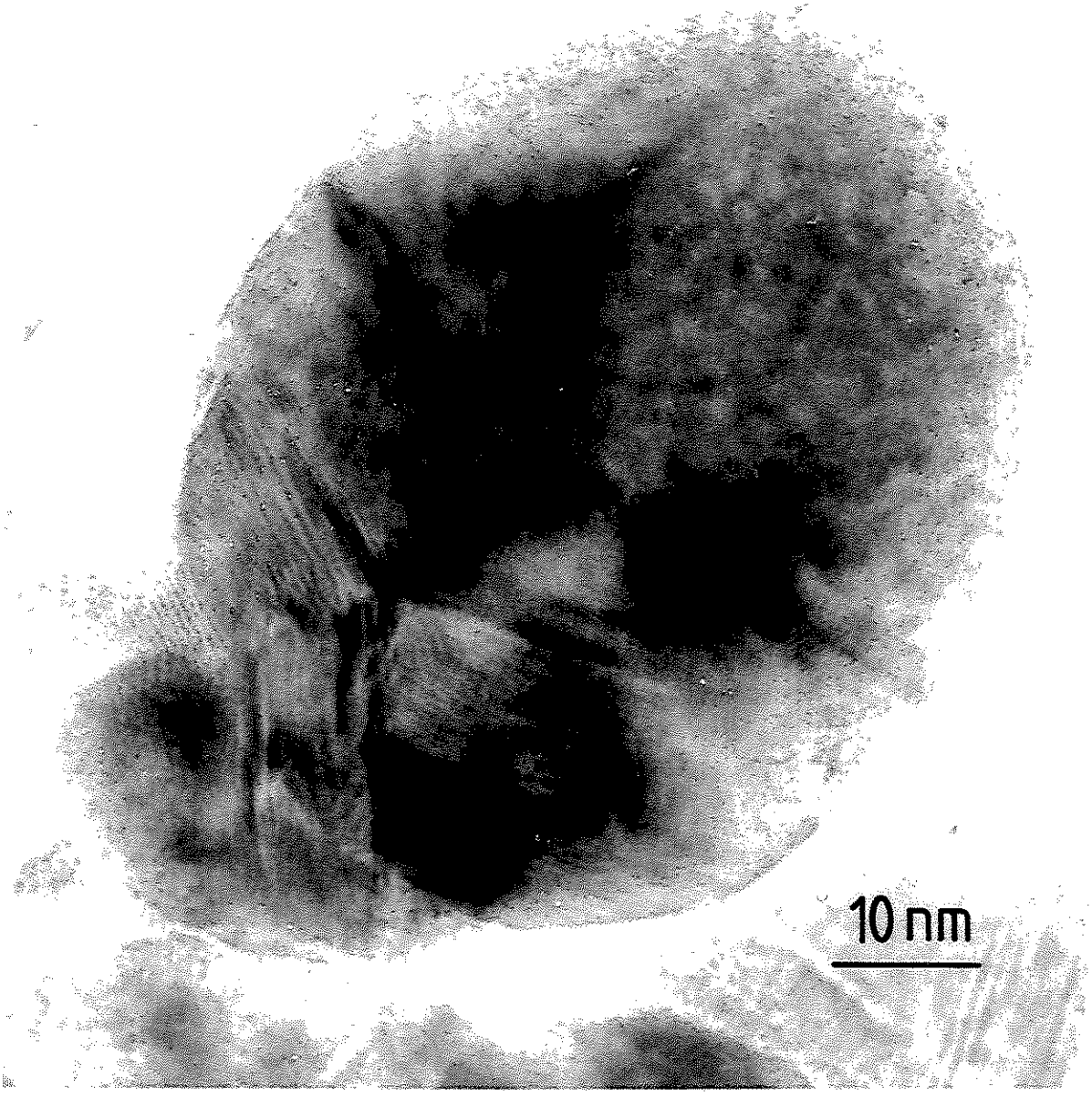

Figure 7.4 High resolution micrograph of a catalyst polyparticle (taken on the Cambridge H.R.E.M. at 500 kV). A Dh near to the 5-fold symmetry orientation is present on the lower left, as is shown by the lattice fringe configuration.

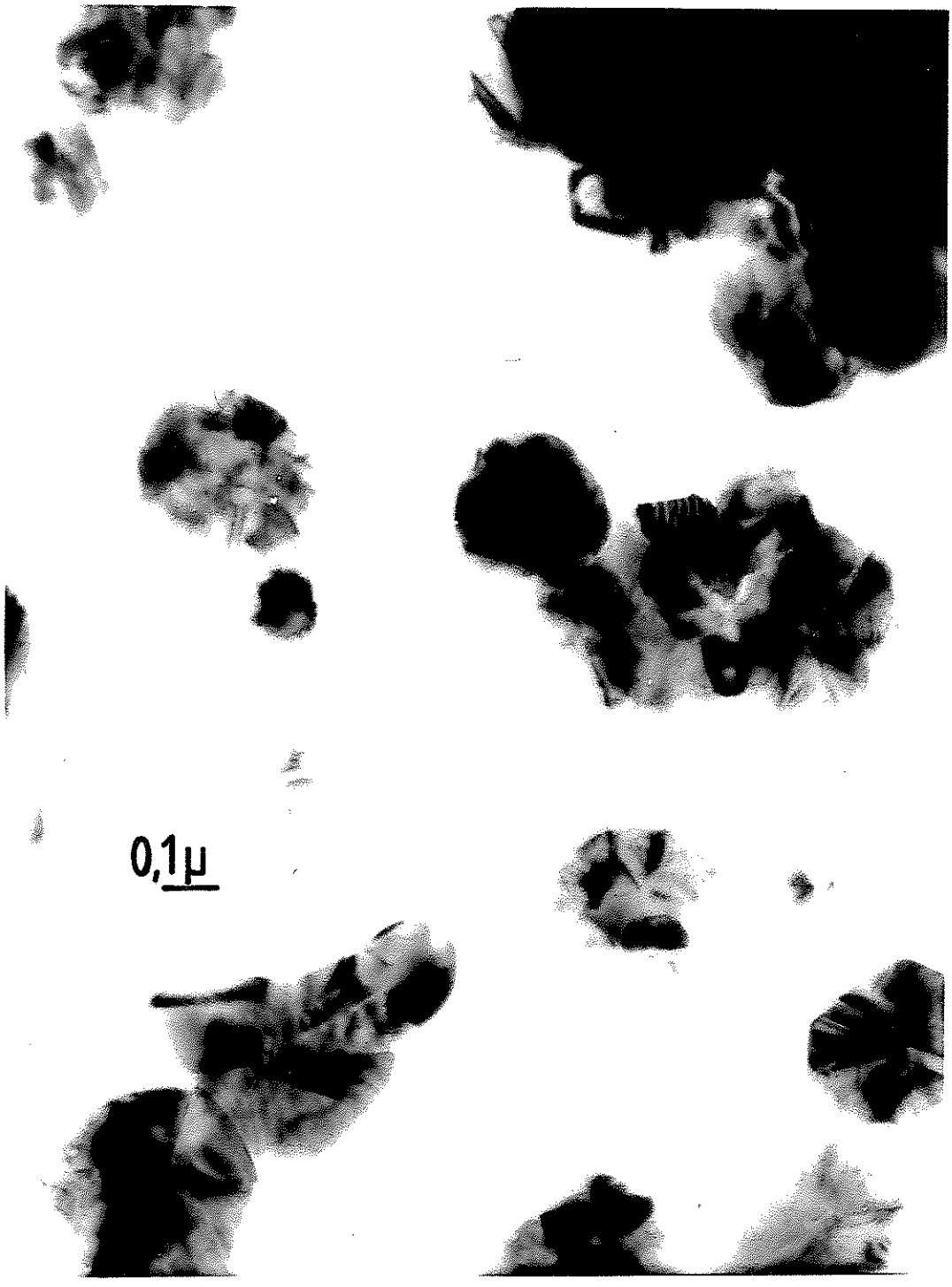

Figure 7.5 Evidence for inter-particular coalescence. This micrograph was obtained through a relatively thin region of the α-alumina support.

7.4 MTPs as Unusual Catalysts

The results presented herein demonstrate that MTPs can occur in heterogeneous catalysts. This raises an important question: are these unusual particles responsible for variations in catalytic behaviour with, for example, particle size, trace impurities or the substrate employed? As described below, there are substantial reasons for believing that MTPs behave catalytically in a very different fashion to single crystal particles. Three major differences between the surfaces of MTPs and single crystals are highlighted: the high concentration of unusual sites on the twin boundaries; the different permution of surface faces; and the presence of surface strains or dislocations.

Atoms on a twin boundary can be expected to display geometric and electronic catalytic effects which have no analogue on a single crystal surface. For example, these atoms have a D_{3h} point group symmetry (i.e. hcp co-ordination rather than fcc), so their d-orbitals have different spatial orientations. The re-entrant surfaces present in the thermally equilibrated particles might possess unusual catalytic properties, similar to their suggested significance as favourable nucleation fites for growth (Frank 1949). The concentration of twin sites could be appreciable: for example, assuming the strong faceting model (3.5.2) for a 5 nm radius Dh, approximately 7% of the surface atoms are on the twin boundaries, a third of these in the notches.

The different distribution of crystal faces (see 3.4.3) could be significant for reactions which are sensitive to the surface crystallography. For example, the absence of any (100) surface in Ics could "poison", as suggested in 4.6, a catalyst dependent upon

this face if large numbers of these particles are present.

The expansions of the surface layer by ~1% and ~ 2% for Dhs and Ics respectively (see 4.2) may also be significant. For example, Flank and Beachell (1967) showed that lattice constant variations in a silver catalyst (produced by alloying with gold) correlated with the rate of ethylene oxidation. The high dislocation densities present, particularly if the defects imaging in 5.4 are true partial dislocations, could also be particularly important.

Anomalous surface sites and strained surfaces are, of course, also found in other particles. Re-entrant surfaces have been observed for fcc particles with an odd number of closely-spaced, parallel twin boundaries (lamellar twinned particles - see 6.3.3) by Hayashi et al (1977). Similar sites and strained surfaces will also be present in any polyparticles. However, the site density in MTPs can be expected to be higher than in any other types.

7.5 Discussion

The occurence of MTPs in a heterogeneous catalyst is consistent with their frequent presence in epitaxial films. MTPs may well occur in many other catalysts: for example, micrographs of a nickel catalyst (supplied by A. Szczpera) showed contrast typical of MTPs. The apparent contradiction between the results presented here and those of Avery and Sanders (1970) is probably due to the different methods of production: the particles described here were prepared by a mild pyrolysis, whilst Avery and Sanders examined theirs after a hydrogen anneal. It should be clear from the analysis in Chapter 4 that the occurence and survival of MTPs in catalysts are very sensitive to the conditions during both

preparation and running.

The large sizes of the MTPs are probably a result of the growth process. The surface structures were consistent with a layer growth process (see 3.6) which, with a sufficiently low nucleation density to prevent appreciable inter-particular coalescence, can in principle proceed indefinitely. Although almost certainly metastable at these sizes, without sufficient activation energy for a structural transformation to occur, the particles will be frozen with the multiply twinned structures.

It should be noted that the other types of discrete particles observed, particularly the needles, are also consistent with this model for growth. Chemically, this mechanism, with low nucleation densities and layer growth, suggests that the oxalate decomposition was catalysed by the silver, i.e. the reaction was autocatalytic.

Clearly, it will now be of considerable interest to produce catalyst samples containing, for example, a large proportion of single crystals and compare their behaviour with a catalyst of MTPs. It might then be possible to directly assess the importance of particle morphology in catalysis.

BIBLIOGRAPHY

Allpress J G and Sanders J V, Surf Sci 7, 1 (1967).

Allpress J G and Sanders J V, Aust J Phys 23, 23 (1970).

Avery N R and Sanders J V, J Catal 18, 129 (1970).

Bagley B G, Nature 208, 674 (1965).

Blakeley D W and Somorjai G A, Surf Sci 65, 419 (1977).

Chadwick G A and Kirchner H O K, Phil Mag 22, 449 (1970).

Clayton R D and Norval S in Specialist Periodical Reports (Chemical) (1980) (Chemical Society, London) in press.

Cockayne D J H, Parsons J R and Hoelke C W, Phil Mag 24, 139 (1971).

Cotton F A and Wilkinson G, Advanced Inorganic Chemistry 3rd Edition (1972) (Wiley, London).

Cosslett V E, Camps R A, Saxton W O, Smith D J, Nixon W C, Ahmed H, Catto C J D, Cleaver J R A, Smith K C A, Timbs A E, Turner P W and Rose P M, Nature 281, 48 (1979).

Coulomb P, J Microsc Spectros Electron 3, 295 (1978).

Cowley J M, Diffraction Physics (1975) (North Holland, Oxford).

Cowley J M and Rees A L G, Nature 158, 550 (1946).

Cowley J M and Rees A L G, Proc Phys Soc 59, 283 (1947).

Caspar DLD and Klug A in Cold Spring Harbour Symposia of Qualitative Biology, 27, 1 (1961) (Cold Spring Harbour, New York).

de Wit R, J Phys C5, 529 (1972).

Dinghas A, Z Krist 105, 305 (1943).

Disgurd C, Maurin M G and Roberts J, Met Corres Ind 51, 255 (1976).

Disgurd C, Maurin M G and Roberts J, Met Corres Ind 51, 320 (1976).

Eriksson J C, Surf Sci 14, 221 (1969).

Eshelby J D, Phil Trans A 244, 87 (1951).

Eshelby J D in Solid State Physics 3, 79 (1956) ed Seitz and Turnball (Academic Press, New York and London).

Flank W H and Beachell H C, J Catal 8, 316 (1967).

Flytzani-Stephanopoulous M, Wong S and Schmidt L D, J Catal 49, 51 (1977).

Frank F C, Discuss Faraday Soc 5, 48, 186 (1949).

Freeman L A, Howie A and Treacy M M J, J Microsc 111, 165 (1977).

Fukano Y and Wayman C M, J Appl Phys 40, 1656 (1969).

Fundamental Aspects of Dislocation Theory, 1, 579-680 (1970). (National Bureau of Standards, Washington, D.C.).

Fuller B in Ideas and Intergrities (1963) (Prentice Hall, New Jersey). Unpublished work of his has been used by Mackay (1962) and Caspar and Clug (1961).

Gaskell P H, Phil Mag 32, 211 (1975).

Gaskell P H and Mistry A B, Phil Mag A39, 3, 245 (1979).

Gillet E, Renou A and Gillet M, Thin Solid Films 29, 2, 217 (1975).

Gillet M, J Crystal Growth 36, 2, 239 (1976).

Gillet M, Surf Sci 67, 139 (1977).

Gordon M B, Cyrot-Lackmann and Desjonqueres, Surf Sci 80, 159 (1979).

Harris W F in Fundamental Aspects of Dislocation Theory 1, 579 (1970). (National Bureau of Standards, Washington, D.C.).

Harrison W A, Pseudopotentials in the theory of metals (1966) (Benjamin, New York).

Hashimoto H, Mannami M and Naiki T, Phil Trans Roy Soc 253, 459 and 490 (1961).

Hayashi T, Ohno T, Shigeki Y and Uyeda R, Jpn J Appl Phys 16, 705 (1977).

Heinemann K and Poppa H, Appl. Phys. Lett 16, 515 (1970).

Heinemann et al (1979)

Heinemann K, Yacaman M J, Yang C Y and Poppa H, J Cryst Growth 47, 177 (1979).

Yacaman M J, Heinemann K, Yank C Y and Poppa H, ibid 187.

Yang C Y, ibid 274.

Yang C Y, Yacaman M J and Heinemann K, ibid 283.

Hirsh P B, Howie A, Nicholson R B, Pashley D W and Whelan M J, Electron Microscopy of Thin Crystals (1965) (Butterworths, London).

Hoare M R and Pal P, J Cryst Growth 17, 77 (1972).

Honjo G, J. Phys Soc Jap 2, 133 (1947).

Ino S, J Phys Soc Jap 21, 346 (1966).

Komoda T , Jap J Appl Phys 7, 27 (1968).

Lang N D and Kohn W, Phys Rev B1, 4555 (1970).

Lang N D and Kohn W, Phys Rev 3, 1215 (1971).

Laue M v, Z Krist 105, 124 (1943).

Lemnpfuhl G and Reissland A, Z f Naturforsch 23a, 544 (1968).

Linford R G, "Surface Thermodynamics of Solids" in Solid State Surface Science II (1973)(Dekker, London, and TCM Library, Cavendish Labs).

Love A E H, A Treatise on the Mathematical Thery of Elasticity (1944) (Dover paperback, London).

Mackay A L, Acta Cryst 15, 916 (1962).

Mays C W, Vermaack J S and Kuhlmann-Wilsdorf D , Surf Sci 12, 125 (1968).

Mays C W, Vermaach J S and Kuhlmann-Wilsdorf D , Surf Sci 12, 134 (1968).

see also:

Vermaak J S and Kuhlmann-Wilsdorf D , J Phys Chem 72, 4150 (1968).

Wasserman H J and Vermaak J S, Surf Sci 22, 164 (1970).

Wasserman H J and Vermaak J S, Surf Sci 32, 168 (1972).

Moliere K and Wagenfeld H, Z Krist 110, 3 (1958).

Murrell J N, Kettle S F A and Tedder J M, Valence Theory (1965) (Wiley, London).

Nabarro F R N, Theory of Crystal Dislocations (1967)(Clarendon Press, Oxford).

Pashley D W, Stowell M J, Jacobs M H and Law T J, Phil Mag 10, 103,127 (1964).

see also:

Jacobs M H, Pashley D W and Stowell M J, Phil Mag 13 , 121, 129 (1966).

Pashley D W and Stowell M J, J Vac Science and Tech 3, 3, 156 (1966).

Rhead G E and McLean M, Acta Met 12, 401 (1964).

Saito Y, Yatsuya S, Mihama K and Uyeda R, Jpn J Appl Phys 17, 1149 (1978).

Shuttleworth R, Proc Roy Soc A63, 444 (1950).

Smart D C, Boswell F W and Corbett J M, J Appl Phys 43, 11 (1972).

Solliard C, Buffat P and Faes F, J Cryst Growth 32, 123 (1976).

Takahashi M, Suzuki T, Kushima H and Ogasawara S, Jpn J Appl Phys 17, 9, 1499 (1978).

Treacy M M J, Howie A and Wilson C J, Phil Mag A38, 569 (1978).

Volterra V, Ann Ec Norm Sup 24, 400 (1907).

Wu J C and Harriott P , J Catal 39, 395 (1975).

Wulff G, Z Krist 34, 449 (1901).

Yagi K, Takayamagi K, Kobayashi K and Honjo G, J Cryst Growth 28, 117 (1975).